

SATELLITE REMOTE SENSING OF ACTIVE WILDFIRES IN ALASKA'S BOREAL FOREST

By

Christine F. Waigl, Dipl.-Phys.

A Dissertation in Partial Fulfillment of the Requirements for the Degree of

Doctor of Philosophy

in

Geophysics (Remote Sensing)

University of Alaska Fairbanks

December 2017

©2017 Christine Waigl

APPROVED:

Dr. Martin Stuefer, Committee Co-Chair

Dr. Anupma Prakash, Committee Co-Chair

Dr. David Verbyla, Committee Member

Dr. Charles Ichoku, Committee Member

Dr. Paul McCarthy, Chair

Department of Geosciences

Dr. Paul Layer, Dean

College of Natural Science and Mathematics

Dr. Michael Castellini, Interim Dean

Graduate School

ABSTRACT

This research addresses improvements to the detection and characterization of active wildfires in Alaska with satellite-based sensors.

The VIIRS I-band Fire Detection Algorithm for High Latitudes (VIFDAHL) was developed and evaluated against existing active fire products from the Visible Infrared Imaging Radiometer Suite (VIIRS) and the Moderate Resolution Imaging Spectroradiometer (MODIS). This new algorithm is based on VIIRS 375 m spatial resolution imagery and was tuned using fires in Alaska's boreal forest. It provides improved fire detection of low-intensity fires, especially during daytime and at sensor zenith angles smaller than approximately 50° off nadir. Low-intensity active fires, which represent residual combustion present after the passage of a high-intensity fire front, are not very well detected by existing active fire products.

A second topic was fire remote sensing with ~30 m resolution imaging spectrometer (or hyperspectral instrument), the Hyperion sensor on NASA's EO-1 spacecraft, which was in use from 2000 to 2016. Hyperion had a much higher spectral resolution than VIIRS or MODIS, but no repeat imagery of the same active fire was available in Alaska. The investigation relied on absorption and emission features in the radiance spectra acquired at every pixel location. Three fire detection methods were evaluated using archived Hyperion data from three fires in interior Alaska from 2004 and 2009: A version of the Hyperspectral Fire Detection Algorithm (HFDI) produced excellent active fire maps; an approach that relies on a shortwave infrared carbon dioxide absorption feature and associated Continuum Interpolated Band Ratio (CO_2 CIBR) proved to be useful, but was affected by sensor noise and clouds; finally, a potassium emission feature from biomass burning was not detectable in the Hyperion data.

Fire temperatures were determined using the Hyperion shortwave infrared spectra between 1400 nm and 2400 nm. The temperatures of active fire, the corresponding partial pixel areas, and the pixel areas occupied by unburned and already-burned vegetation, respectively, were modeled within each fire pixel. A model with two reflected background components and two tempera-

ture endmembers, applied to the same three study scenes, yielded an excellent fit to Hyperion spectral radiance data. Fire temperatures ranged from approximately 500-600 K to approximately 800-900 K. The retrieved lower fire temperatures are within the range of smoldering combustion; high-temperature values are limited by Hyperion's saturation behavior. High-temperature fire occupying 0.2% of a pixel (2 m^2) was detectable. Sub-pixel fire area and temperature were also retrieved using VIIRS 750 m (M-band) data, with comparable results. Uncertainties were evaluated using a Monte Carlo simulation.

This work offers insight into the sensitivity of fire detection products to time of day (largely due to overpass timing), spatial distribution over the study area (largely due to orbital properties) and sensor zenith angle. The results are relevant for sensor and algorithm design regarding the use of new multi- and hyperspectral sensors for fire science in the northern high latitudes. Data products resulting from this research were designed to be suitable for supporting fire management with an emphasis on real-time applications and also address less time-sensitive questions such as retrievals of fire temperature and time series of fire evolution.

TABLE OF CONTENTS

	Page
Abstract.....	iii
Table of Contents.....	v
List of Figures	ix
List of Tables	xi
Acknowledgements	xiii
Chapter 1 General Introduction	1
1.1 Fires in the boreal forest	1
1.2 Satellite remote sensing of active fires	3
1.3 Objectives and structure of this dissertation	5
References	6
Chapter 2 Detecting high and low-intensity fires in Alaska using VIIRS I-band data: An improved operational approach for high latitudes	11
Abstract.....	11
2.1 Introduction	12
2.2 Global active fire products: a brief review.....	13
2.3 Wildfire study areas	15
2.3.1 Willow: Sockeye fire, June 2015.....	16
2.3.2 Yukon-Koyukuk: multiple wildfires, July 2015	17
2.3.3 Eagle: early-season wildfires, May 2015	17
2.3.4 Northern Koyukuk: multiple large fires, July 2016	18
2.4 Data	18

2.4.1	Global MODIS and VIIRS I-band products	18
2.4.2	VIIRS Sensor Data Record (SDR) data.....	19
2.4.3	Fire location and perimeter data	20
2.4.4	Landsat 8 imagery	22
2.4.5	Evaluation of operational MODIS and VIIRS I-band products	23
2.4.6	VIIRS I-band Fire Detection Algorithm for High Latitudes (VIFDAHL).....	23
2.4.7	Validation using Landsat 8	28
2.5	Results	28
2.5.1	Exploratory data analysis of operational MODIS and VIIRS I-band fire de- tection datasets.....	28
2.5.2	VIIRS I-band Fire Detection Algorithm for High Latitudes (VIFDAHL).....	32
2.6	Discussion and conclusions	33
2.7	Acknowledgements.....	36
	References	36

Chapter 3	Fire detection and temperature retrieval using EO-1 Hyperion data over selected Alaskan boreal forest fires	41
Abstract.....	41	
3.1	Introduction	42
3.2	Study Areas	44
3.3	Data	45
3.3.1	The Hyperion sensor on EO-1.....	45
3.3.2	Hyperion scenes	46
3.4	Methods	47
3.4.1	Fire-related feature extraction	48
3.4.2	Fire detection	49
3.4.3	MODTRAN for atmospheric correction.....	52
3.4.4	Temperature retrieval	53
3.5	Results	55
3.5.1	Fire detection and comparative analysis.....	55

3.5.2	Temperature retrieval	61
3.6	Discussion	64
3.7	Conclusions, recommendations, and future work.....	67
3.8	Acknowledgements.....	68
	References	69
Chapter 4	Sensitivity considerations in fire detection and sub-pixel fire temperature retrieval with Suomi-NPP VIIRS	77
	Abstract.....	77
4.1	Introduction	77
4.2	Study area and data used.....	80
4.3	Methods	81
4.3.1	Fire detection	81
4.3.2	Sensor angle statistics	82
4.3.3	Temperature retrieval	83
4.3.4	Atmospheric correction	85
4.3.5	Uncertainty estimation	85
4.4	Results and discussion.....	86
4.4.1	Zenith angle dependency of fire detection.....	86
4.4.2	Fire temperature and partial pixel area retrieval	90
4.5	Conclusions.....	93
	References	94
Chapter 5	General Conclusion	99
	References	102
Appendix A	Coal-Fire Hazard Mapping in High-Latitude Coal Basins: A Case Study from Interior Alaska	103
A.1	High latitude coal fires	104
A.1.1	Introduction	104
A.1.2	Alaskan Context	105

A.2 Case Study from Interior Alaska	107
A.2.1 Introduction	107
A.2.2 Study Area	108
A.2.3 Data.....	110
A.2.4 Data Processing.....	113
A.2.5 Results	119
A.2.6 Discussion.....	120
A.2.7 Conclusions	122
A.2.8 Acknowledgements	123
A.2.9 Important Terms.....	123
References	124

LIST OF FIGURES

	Page
1.1 Alaska wildfire perimeters, 1998–2017.....	2
2.1 Location of the four 2015 and 2016 wildfire study areas within Alaska	16
2.2 VIFDAHL (VIIRS I-band Fire Detection Algorithm for High Latitudes) processing workflow.....	24
2.3 Willow study area, Sockeye fire 2015-06-15, 15:09 AKDT	26
2.4 VIIRS I-band pixel anomalies illustrated for a subset of the 2015 Yukon-Koyukuk study area on 2015-07-06.....	27
2.5 Global VIIRS I-band (375 m) vs. MODIS (both Terra and Aqua) fire detection counts....	30
2.6 Hourly detection counts across the Alaska 2016 fire season for global fire products	30
2.7 Spatio-temporal distribution of fire detections from global active fire products	31
2.8 Overview of three study areas with VIFDAHL fire detections outlined	34
2.9 Overview and zoom into 2015 Yukon-Koyukuk study area.....	35
2.10 Willow study area, fire progression in 6-hour intervals.....	35
3.1 Map of study areas	45
3.2 Wavelength range of the VNIR and SWIR instruments of the Hyperion sensor	46
3.3 Hyperion processing flow	48
3.4 Crazy fire (top) and Boundary fire (bottom)	56
3.5 Examples of fire pixel radiance spectra	57
3.6 Box plots of the distributions of average HFDI, carbon dioxide CIBR and K-emission band difference index across fire and background pixels for each fire event	58
3.7 Values of average HFDI and CO ₂ CIBR for the Crazy and Boundary fire study areas....	59
3.8 Example spectra for T-retrieval	62
3.9 Burning areas of the Crazy and Boundary study sites	63

4.1	Within the rectangular area, all fire detections from the global VIIRS I-band product between July 9, 2017 and July 24, 2017, are shown in red	80
4.2	Sensor look angle (pink) and sensor zenith angle (red)	82
4.3	Planck blackbody spectral radiance curves.....	83
4.4	Distribution of zenith angles at the center of the 62 VIIRS scenes with nonzero VIF-DAHL detections.....	89
4.5	VIIRS I-band fire detection counts	89
4.6	VIIRS MIR spectral radiance.....	91
4.7	Spectral response function and atmospheric transmittance for MIR bands	93
A.1	Remote Rugged Winter Landscape	103
A.2	This representation shows the Earth in relation to the incoming solar radiation during summer in the northern hemisphere.....	105
A.3	Burn pattern typical for wildfire in an Alaskan boreal forest	106
A.4	Map of Alaska showing the major coal basins and coal deposits.....	107
A.5	Map of Alaska showing the major coal basins and coal deposit by rank (where known)	108
A.6	A field photograph of the 2012 Windfall Mountain fire	109
A.7	Study area (red rectangle) and its location within interior Alaska.....	110
A.8	A subset of the selected 2011 Landsat image covering the study area.....	115
A.9	Result of classifying the selected 2011 Landsat image using the LTK algorithm	116
A.10	Selected 2011 Landsat image after masking out clouds, smoke, active fires, fresh burn scars, and missing data pixels.....	117
A.11	Distribution of radiant temperature calculated from the thermal infrared band of the selected 2011 Landsat image	118
A.12	Thermal anomalies retrieved from the 2011 Landsat scene	120
A.13	Persistent thermal anomalies (red and magenta) delineated after stacking 40 processed Landsat scenes	121

LIST OF TABLES

	Page
2.1 Overview of VIIRS swath data.....	20
2.2 GIS attributes in the AICC and global fire product datasets	21
2.3 Landsat and VIIRS scenes used for validation.....	21
2.4 VIIRS I-band pixel anomalies illustrated for a subset of the 2015 Yukon-Koyukuk study area on 2015-07-06.....	27
2.5 Overall detection performance of MODIS and VIIRS I-band fire products	29
2.6 Comparison of VIFDAHL with the global VIIRS I-band product and with Landsat 8 fire detections	29
3.1 EO-1 Hyperion scenes and central latitude/longitude (WGS 84) of the subsets used	47
3.2 Configuration used with MODTRAN 5.3.....	53
3.3 HFDI band combinations evaluated for 500 labeled sample pixels.....	60
4.1 Parameters for VIIRS M-bands used in Dozier retrieval.....	85
4.2 List of 62 VIIRS SDR granules used in this study with non-zero fire detection counts for at least one method (VIIRS I-band or VIFDAHL). Totals are 3252 detections from the global VIIRS I-band product and 3247 from VIFDAHL.....	87
4.3 Sample results of M-band sub-pixel temperature retrieval, sorted by fractional pixel area occupied by fire	91
A.1 List of 40 Landsat scenes used to retrieve persistent thermal anomalies	112

ACKNOWLEDGEMENTS

This PhD thesis would not have been possible without the help of many. First and foremost, my gratitude goes to my co-advisors: Dr. Martin Stuefer for the opportunity to discover the science of the circum-polar North, and Dr. Anupma Prakash for the push and constant encouragement that I needed to take the leap and acquire my own scientific credentials. My growth as a scientist, academic and professional is largely due to them.

My committee, and the many members of the geosciences and STEM community at UAF and beyond, my co-authors, the staff of the UAF Geophysical Institute and College of Natural Science and Mathematics, my grad student peers have offered me their knowledge, wisdom, critique, or sympathetic ear, and traveled along with me for a section of my path. The list is too long and the risk too great to inadvertently omit a person, so I will not even try to name them all.

To wife and life partner, Melinda Shore, thank you so much for everything.

Finally, this work would not have been possible without the funding I have received from numerous sources. My PhD work was supported by NASA Headquarters under the NASA Earth and Space Science Fellowship (NESSF) Program, Grant NNX13AN90H; by a UAF Center for Global Change Student Research Grant with funds from the Cooperative Institute for Alaska Research (CIFAR) as well as funds from the National Oceanic and Atmospheric Administration (NOAA) under cooperative agreement NA13OAR4320056 with the University of Alaska; by the Alaska EPSCoR NSF award #OIA-1208927 and the state of Alaska; and by the (former) Arctic Region Supercomputing Center (ARSC). The University of Alaska Fairbanks Office of the Vice-Chancellor of Research, the College of Natural Science and Mathematics and the Geophysical Institute Graduate Students' Association provided travel and publication cost support. The Federation of Earth Science Information Partners (ESIP) awarded me the Rankin Scholarship, which allowed me to travel to the 2015 summer meeting. To all of them, I am indebted and offer my assurance that I will endeavor to live up to their trust.

Chapter 1

GENERAL INTRODUCTION

1.1 Fires in the boreal forest

Wildfire is a major natural hazard and an important factor in landscape change and disturbance in many regions of the earth, wherever vegetation is available to serve as fuel. In the boreal forests of the circum-polar North wildfires are an essential ingredient for ecological renewal and change. These regions play a vital role in the earth system: Arctic and sub-Arctic ecosystems constitute approximately 22 % of the earth's land mass (Chapin et al. 2000) and represent one third of the global forested area (Dixon et al. 1994). Their soils are characterized by an accumulation of fine organic litter referred to as duff (e.g. Kasischke et al. 2005), which is decomposing only slowly due to the low average temperatures and the presence of continuous or discontinuous permafrost soils.

Scientific interest in the study of fire in the boreal zone is in part driven by the sensitivity of these regions to climate warming (Chapin et al. 2004; Collins et al. 2013; Kasischke and Turetsky 2006), and in part by the needs of fire management agencies, which have to operate over a vast area generally inaccessible by road. Other than selected locations targeted by timber harvest or fuel treatment for wildfire risk reduction, these are sparsely inhabited spaces with human activity concentrated in few locations. Large boreal wildfires affect atmospheric composition and air quality (Andreae 1991; Grell et al. 2011) and are a threat to critical infrastructure. Satellite-based approaches are therefore of great relevance for both fire science and decision support.

Important differences exist in the fire regimes between sub-regions of the global boreal zone. The term fire regime is used in the literature in a variety of ways to describe frequency and seasonality of fire, as well as the distribution of fire attributes such as: burned area per fire event, flaming versus smoldering combustion, crown fires versus surface fires, fire temperatures, power output, flame lengths, fire front propagation speeds etc. (e.g. Johnstone et al. 2010; Kasischke and

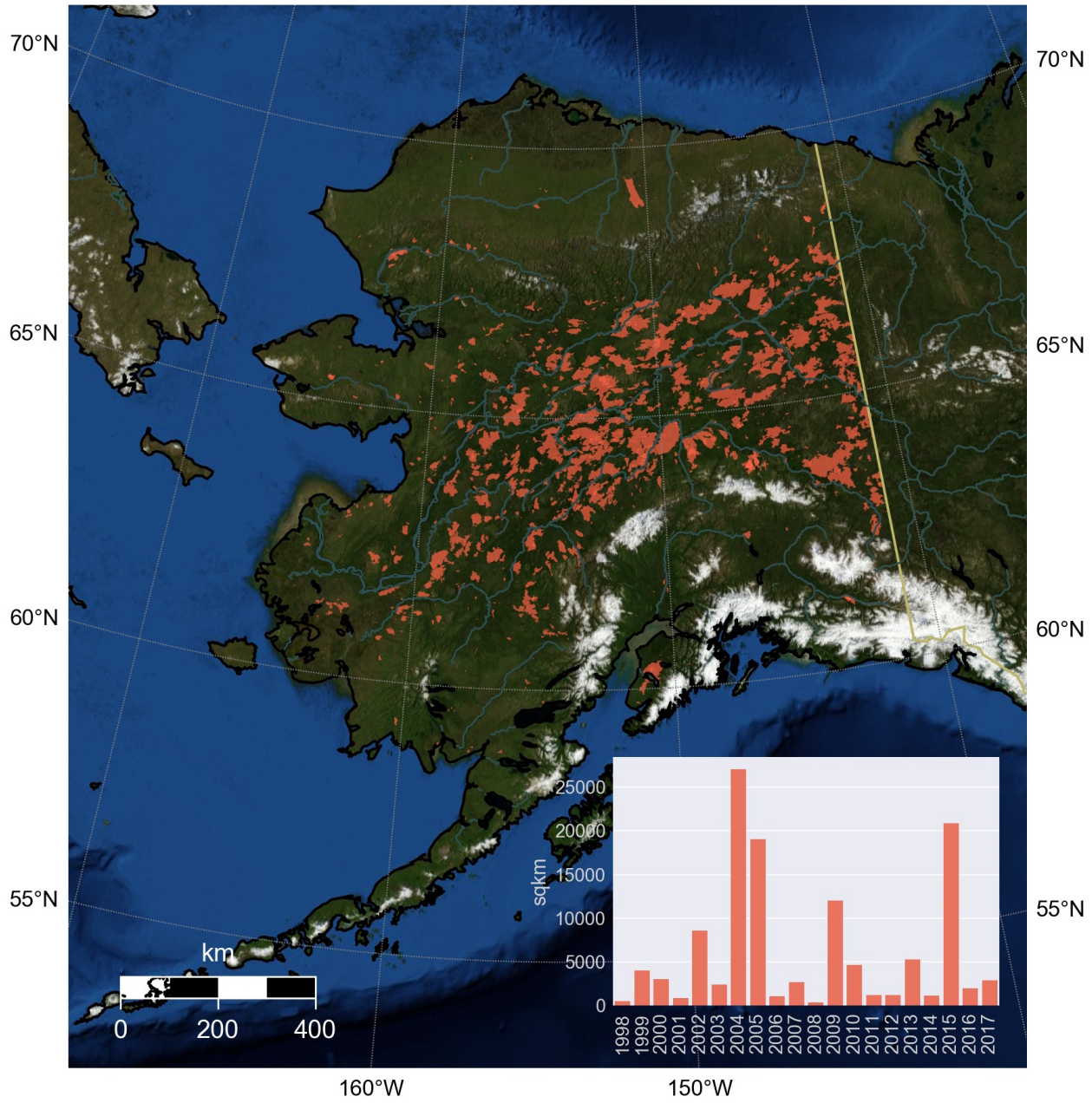


Figure 1.1: Alaska wildfire perimeters, 1998–2017 (source: Alaska Large Fires Database/Alaska Fire Service). The inset shows the yearly cumulative area enclosed by the fire perimeters.

Turetsky 2006; Rein et al. 2008). Highly flammable understory and mosses favor ignition and fire spread (van Cleve et al. 1991). In the boreal forests of Alaska, in particular the areas dominated by black spruce (*Picea mariana*) and the parts of Canada covered in spruce and lodgepole pine (*Pinus contorta*), large stand-replacing crown fires are particularly common (Chapin et al. 2004). In contrast, the mature Eurasian boreal forest has a higher prevalence of more fire-resistant conif-

erous species such as Scots pine (*Pinus sylvestris*) and Siberian larch (*Larix siberica*), so surface fires are more common there (Soja et al. 2007). Such differences matter for the detection and characterization of fires using a satellite-borne sensor.

This dissertation focuses on fires in the boreal forest of Alaska, where they are a common, recurring phenomenon: In any given decade, a large part of the forested area of interior Alaska is affected by wildfire; however, the total burned area varies greatly from year to year (Figure 1.1). The largest fires, and therefore the area burned, are driven by ignition by lightning strikes (Dissing and Verbyla 2003; Kasischke et al. 2010; Veraverbeke et al. 2017), given suitable hot and dry conditions that sustain fire spread. In Alaska fires in regions dominated by black spruce, a large part (50-80%) of the carbon emissions stem from the surface and sub-surface layers (Kasischke and Hoy 2012; Randerson et al. 2006).

1.2 Satellite remote sensing of active fires

Satellite remote sensing of active fires makes use of the infrared radiation emitted by biomass combustion. Sensors detect the fire's emitted electromagnetic radiation in the shortwave (SWIR, 1100–2500 nm), mid- (MIR, 3–5 μm) and thermal infrared (TIR, 8–15 μm) regions of the electromagnetic spectrum to identify image pixels whose footprint on the earth surface contains active combustion. Operational fire detection with sensors on polar-orbiting satellites was implemented since the 1980s (e.g. Ichoku et al. 2012) and has been in widespread use by fire managers at least since the well-validated global fire products from NASA's Moderate Resolution Imaging Spectroradiometer (MODIS) became easily available to a wide user community (Giglio et al. 2003, 2016; Justice et al. 2010; Kaufman et al. 1998).

Geostationary satellites, such as for example the Geostationary Operational Environmental Satellites (GOES) of the United States National Oceanic and Atmospheric Administration (NOAA), also play an important role in active fire remote sensing. Several algorithms, both for active fire monitoring (Menzel and Prins 1996; Prins et al. 2001) and early fire detection (Koltunov et al. 2016), are in use. In high latitudes, however, geometric effects lead to pixel distortion and lower the spatial resolution of a geostationary earth-observing system. On the other hand, polar-orbiting

satellites have advantages in the high latitudes as their orbits converge towards the poles, and therefore the imaging frequency for a location on the earth surface is increased. Therefore, this work only considers sensors on polar-orbiting platforms.

MODIS is a multispectral sensor, which means that it acquires imagery in a number of individually selected, carefully placed spectral bands. Design criteria are based on the targeted scientific applications, and sensitivity and bandwidth vary from band to band. A different class of sensors are imaging spectrometers, also called hyperspectral sensors. They offer a much increased spectral resolution, typically acquiring reflectance or radiance spectra across the visible and near-infrared (VNIR, up to 1100 nm) and shortwave infrared (1100 nm to 2500 nm) regions of the electromagnetic spectrum at every imaging pixel. They essentially provide a very large data volume, but over a more restricted spectral region, than multispectral sensors that specialize in fire detection. Fire detection and characterization with this type of space-borne sensor in the boreal forest has not, up to now, been explored in depth by the research community. Furthermore, ongoing and planned satellite missions with hyperspectral sensors will open up opportunities to apply such approaches to fire remote sensing. This study explores the potential of satellite-borne hyperspectral remote sensing using the Hyperion sensor on NASA's EO-1 satellite, which has a spatial resolution of 30 m (Middleton et al. 2013; Ungar et al. 2003).

A characteristic feature of sensors on polar-orbiting satellites is the trade-off between temporal and spatial resolution: Given the constraints on their orbital properties, an increase of the number of overpasses that image a given location is achieved by widening the image swath and thereby lowering the spatial resolution. The imagery used in this work therefore falls in one of two classes: Those with a spatial resolution of the order of 1 km (values range from 375 m at nadir (Cao et al. 2014), to approximately 2×5 km (Lee et al. 2006)) and those whose ground-sampling distance (GSD) is approximately 30 m. Coarser-resolution imagery of a location is available multiple times every day in the high latitudes, compared to every 2-3 weeks for the higher-resolution class. From the coarser-resolution class, we used MODIS as well as the Visible Infrared Imaging Radiometer Suite (VIIRS), which was launched on October 28, 2011, and is operated under a joint program by both NOAA and NASA; as for ~30 m imagery, we rely on Hyperion as well as data from the TM, ETM+ and OLI/TIRS sensors carried on Landsat 5, 7 and 8, respectively.

Beyond fire detection, this work addresses fire characterization. One of the most fundamental characteristics of a fire is the temperature at which it burns. Active fire products, however, often focus on a different variable, fire-radiative power (FRP), which is the rate of emission of radiative energy (Wooster et al. 2005). There are valid reasons for this choice: First, the radiance measured at the sensor reflects the rate of energy released on the ground (minus atmospheric losses), whereas the concept of fire temperature refers to only the (often very small) portion of the pixel that contains active fire. Second, scientific questions relevant to climate and atmospheric science, such as carbon consumption or trace gas emissions, are directly linked to the consumption of biomass and therefore energy released by the fire (*ibid.*). On the other hand, we can argue in favor of making fire temperature the object of study: FRP is determined via temperature retrievals anyway, sometimes using empirical relations between the two quantities in the data provided by a given sensor (Kaufman et al. 1998); and whether we study FRP or fire temperature, an active fire scene is always an instantaneous snapshot of processes that develop and change over time, so FRP retrievals in the best case only provide instantaneous rates of carbon consumption. Moreover, fire temperature opens its own avenues for future research: temperature is one way to delineate flaming from smoldering combustion, which is a crucial distinction that drives the nature and quantity of fire emissions (Andreae 1991; French et al. 2002). It is temperature that governs fire-related processes such as drying, pyrolysis, or ignition (Rein et al. 2008).

1.3 Objectives and structure of this dissertation

The goal of this dissertation is to advance the detection and characterization of fires in Alaska's boreal forest using new or improved remote sensing techniques. We use data from VIIRS on the Suomi-NPP satellite and Hyperion for fire detection and active fire temperature retrieval. For purposes of validation we rely, where appropriate, on Landsat data and published Landsat-based fire detection and landcover classification algorithms.

In Chapter 2 the performance of existing global active fire detection products from MODIS and VIIRS is evaluated using data from the Alaska fire seasons of 2015 and 2016, and a new fire detection algorithm is introduced. The VIIRS Fire Detection Algorithm for High Latitudes

(VIFDAHL) is described. It is based on the imaging bands of the VIIRS sensor (I-bands, 375 m resolution at nadir). Landsat 8 data is used for validation.

Chapter 3 presents the first study of North American boreal forest fires using satellite-borne imaging spectroscopy with NASA's Hyperion sensor. Three fire detection methods are evaluated and compared, and sub-pixel active fire temperatures and fractional areas of fire and background components are determined using a linear spectral mixture model.

Chapter 4 explores a similar approach to temperature retrieval, the well-documented Dozier method (Dozier 1981), but used with VIIRS imagery acquired over Alaska to retrieve active fire temperatures in mid- and thermal infrared multispectral data. The sensitivity of fire detection to sensor angle and uncertainty considerations are addressed.

In Chapter 5, the results are summarized.

Finally, the Appendix offers a related investigation, the topic of which is fire hazard mapping in coal seam fires. Fire hazard areas were associated with persistent thermal anomalies in Landsat imagery acquired over the coal-bearing regions of interior Alaska, where coal seam fires are a recurring phenomenon and sometimes ignite forest fires.

Chapters 2, 3, 4, and the appendix are multi-authored articles. In chapters 2, 3, and 4, I contributed to the research design, collected the data, carried out the data analysis, generated the visualizations, and produced the initial manuscript. In the appendix, I contributed to the research design, collected the data, carried out most of the data analysis, generated the visualizations, and contributed to the writing.

References

- Andreae, M. O. (1991). Biomass burning: Its history, use, and distribution and its impact on environmental quality and global climate. In: *Global Biomass Burning: Atmospheric, Climatic and Biospheric Implications*. Ed. by L. J. S. Cambridge, Massachusetts: MIT Press, pp. 3–21.

Cao, C., F. J. D. Luccia, X. Xiong, R. Wolfe, and F. Weng (2014). Early On-Orbit Performance of the Visible Infrared Imaging Radiometer Suite Onboard the Suomi National Polar-Orbiting Partnership (S-NPP) Satellite. *IEEE Transactions on Geoscience and Remote Sensing*, vol. 52, no. 2, pp. 1142–1156. DOI: 10.1109/TGRS.2013.2247768.

Chapin, F. S., A. D. McGuire, J. Randerson, R. Pielke, D. Baldocchi, S. E. Hobbie, N. Roulet, W. Eugster, E. Kasischke, E. B. Rastetter, S. A. Zimov, and S. W. Running (2000). Arctic and boreal ecosystems of western North America as components of the climate system. *Global Change Biology*, vol. 6, pp. 211–223. DOI: 10.1046/j.1365-2486.2000.06022.x.

Chapin, F. S., T. V. Callaghan, Y. Bergeron, M. Fukuda, J. F. Johnstone, G. Juday, and S. A. Zimov (2004). Global Change and the Boreal Forest: Thresholds, Shifting States or Gradual Change? *AMBIO: A Journal of the Human Environment*, vol. 33, no. 6, pp. 361–365. DOI: 10.1579/0044-7447-33.6.361.

Collins, M., R. Knutti, J. Arblaster, J.-L. Dufresne, T. Fichefet, P. Friedlingstein, X. Gao, W. J. Gutowski, T. Johns, G. Krinner, M. Shongwe, C. Tebaldi, A. J. Weaver, and M. Wehner (2013). Chapter 12 - Long-term climate change: Projections, commitments and irreversibility. In: *Climate Change 2013: The Physical Science Basis. IPCC Working Group I Contribution to AR5*. Ed. by IPCC. Cambridge: Cambridge University Press.

Dissing, D. and D. L. Verbyla (2003). Spatial patterns of lightning strikes in interior Alaska and their relations to elevation and vegetation. *Canadian Journal of Forest Research*, vol. 33, no. 5, pp. 770–782. DOI: 10.1139/x02-214.

Dixon, R., S. Brown, R. Houghton, A. Solomon, M. Trexler, and J. Wisniewski (1994). Carbon Pools and Flux of Global Forest Ecosystems. *Science*, vol. 263, no. 5144, pp. 185–190. DOI: 10.1126/science.263.5144.185.

Dozier, J. (1981). A method for satellite identification of surface temperature fields of subpixel resolution. *Remote Sensing of Environment*, vol. 11, pp. 221–229. DOI: 10.1016/0034-4257(81)90021-3.

French, N. H. F., E. S. Kasischke, and D. G. Williams (2002). Variability in the emission of carbon-based trace gases from wildfire in the Alaskan boreal forest. *Journal of Geophysical Research: Atmospheres*, vol. 107, p. 8151. DOI: 10.1029/2001JD000480.

Giglio, L., J. Descloitres, C. O. Justice, and Y. J. Kaufman (2003). An Enhanced Contextual Fire Detection Algorithm for MODIS. *Remote Sensing of Environment*, vol. 87, no. 2, pp. 273–282. DOI: 10.1016/S0034-4257(03)00184-6.

Giglio, L., W. Schroeder, and C. O. Justice (2016). The collection 6 MODIS active fire detection algorithm and fire products. *Remote Sensing of Environment*, vol. 178, pp. 31–41. DOI: 10.1016/j.rse.2016.02.054.

Grell, G., S. R. Freitas, M. Stuefer, and J. Fast (2011). Inclusion of biomass burning in WRF-Chem: impact of wildfires on weather forecasts. *Atmos. Chem. Phys.* Vol. 11, no. 11, pp. 5289–5303. DOI: 10.5194/acp-11-5289-2011.

Ichoku, C., R. Kahn, and M. Chin (2012). Satellite contributions to the quantitative characterization of biomass burning for climate modeling. *Atmospheric Research*, vol. 111, pp. 1–28. DOI: 10.1016/j.atmosres.2012.03.007.

Johnstone, J. F., T. N. Hollingsworth, F. S. Chapin, and M. C. Mack (2010). Changes in fire regime break the legacy lock on successional trajectories in Alaskan boreal forest. *Global Change Biology*, vol. 16, no. 4, pp. 1281–1295. DOI: 10.1111/j.1365-2486.2009.02051.x.

Justice, C. O., L. Giglio, D. Roy, L. Boschetti, I. Csiszar, D. Davies, S. Korontzi, W. Schroeder, K. O’Neal, and J. Morisette (2010). MODIS-Derived Global Fire Products. In: *Land Remote Sensing and Global Environmental Change*. Remote Sensing and Digital Image Processing. Springer, New York, NY, pp. 661–679. DOI: 10.1007/978-1-4419-6749-7_29.

Kasischke, E. S. and E. E. Hoy (2012). Controls on carbon consumption during Alaskan wildland fires. *Global Change Biology*, vol. 18, no. 2, pp. 685–699. DOI: 10.1111/j.1365-2486.2011.02573.x.

Kasischke, E. S., E. J. Hyer, P. C. Novelli, L. P. Bruhwiler, N. H. F. French, A. I. Sukhinin, J. H. Hewson, and B. J. Stocks (2005). Influences of boreal fire emissions on Northern Hemisphere atmospheric carbon and carbon monoxide. *Global Biogeochemical Cycles*, vol. 19, no. 1, GB1012. DOI: 10.1029/2004GB002300.

Kasischke, E. S. and M. R. Turetsky (2006). Recent changes in the fire regime across the North American boreal region—Spatial and temporal patterns of burning across Canada and Alaska. *Geophysical Research Letters*, vol. 33, no. 9, p. L09703. DOI: 10.1029/2006GL025677.

Kasischke, E. S., D. L. Verbyla, T. S. Rupp, A. D. McGuire, K. A. Murphy, R. Jandt, J. L. Barnes, E. E. Hoy, P. A. Duffy, M. Calef, and M. R. Turetsky (2010). Alaska’s changing fire regime – implications for the vulnerability of its boreal forests. *Canadian Journal of Forest Research*, vol. 40, no. 7, pp. 1313–1324. DOI: 10.1139/X10-098.

Kaufman, Y. J., C. O. Justice, L. P. Flynn, J. D. Kendall, E. M. Prins, L. Giglio, D. E. Ward, W. P. Menzel, and A. W. Setzer (1998). Potential global fire monitoring from EOS-MODIS. *Journal of Geophysical Research*, vol. 103, PP. 32, 215–32, 238. DOI: 10.1029/98JD01644.

Koltunov, A., S. L. Ustin, B. Quayle, B. Schwind, V. G. Ambrosia, and W. Li (2016). The development and first validation of the GOES Early Fire Detection (GOES-EFD) algorithm. *Remote Sensing of Environment*, vol. 184, pp. 436–453. DOI: 10.1016/j.rse.2016.07.021.

Lee, T. F., S. D. Miller, C. Schueler, and S. Miller (2006). NASA MODIS Previews NPOESS VIIRS Capabilities. *Weather & Forecasting*, vol. 21, no. 4, pp. 649–655. DOI: 10.1175/WAF935.1.

Menzel, W. P. and E. M. Prins (1996). Monitoring biomass burning with the new generation of geostationary satellites. In: *Biomass Burning and Global Change*. Ed. by J. S. Levine. Vol. 1. MIT Press, pp. 56–64.

Middleton, E., S. Ungar, D. Mandl, L. Ong, S. Frye, P. Campbell, D. Landis, J. Young, and N. Pollock (2013). The Earth Observing One (EO-1) Satellite Mission: Over a Decade in Space. *IEEE Journal of Selected Topics in Applied Earth Observations and Remote Sensing*, vol. 6, no. 2. 00006, pp. 243–256. DOI: 10.1109/JSTARS.2013.2249496.

Prins, E. M., J. Schmetz, L. Flynn, D. Hillger, and J. Feltz (2001). An overview of diurnal active fire monitoring using a suite of international geostationary satellites. *Global and Regional Vegetation Monitoring from Space: Planning a Coordinated International Effort*, pp. 145–170.

Randerson, J. T., H. Liu, M. G. Flanner, S. D. Chambers, Y. Jin, P. G. Hess, G. Pfister, M. C. Mack, K. K. Treseder, L. R. Welp, F. S. Chapin, J. W. Harden, M. L. Goulden, E. Lyons, J. C. Neff, E. a. G. Schuur, and C. S. Zender (2006). The Impact of Boreal Forest Fire on Climate Warming. *Science*, vol. 314, no. 5802, pp. 1130–1132. DOI: 10.1126/science.1132075.

Rein, G., N. Cleaver, C. Ashton, P. Pironi, and J. L. Torero (2008). The severity of smouldering peat fires and damage to the forest soil. *CATENA. Fire Effects on Soil Properties*, vol. 74, no. 3, pp. 304–309. DOI: 10.1016/j.catena.2008.05.008.

Soja, A. J., N. M. Tchekakova, N. H. F. French, M. D. Flannigan, H. H. Shugart, B. J. Stocks, A. I. Sukhinin, E. I. Parfenova, F. S. Chapin III, and P. W. Stackhouse Jr. (2007). Climate-induced boreal forest change: Predictions versus current observations. *Global and Planetary Change*, vol. 56, no. 3–4, pp. 274–296. DOI: 10.1016/j.gloplacha.2006.07.028.

Ungar, S., J. Pearlman, J. Mendenhall, and D. Reuter (2003). Overview of the Earth Observing One (EO-1) mission. *IEEE Transactions on Geoscience and Remote Sensing*, vol. 41, no. 6. 00243, pp. 1149–1159. DOI: 10.1109/TGRS.2003.815999.

van Cleve, K., F. S. Chapin, C. T. Dyrness, and L. A. Viereck (1991). Element Cycling in Taiga Forests: State-Factor Control. *BioScience*, vol. 41, no. 2, pp. 78–88. DOI: 10.2307/1311560.

Veraverbeke, S., B. M. Rogers, M. L. Goulden, R. R. Jandt, C. E. Miller, E. B. Wiggins, and J. T. Randerson (2017). Lightning as a major driver of recent large fire years in North American boreal forests. *Nature Climate Change*, vol. 7, no. 7, pp. 529–534. DOI: 10.1038/nclimate3329.

Wooster, M. J., G. Roberts, G. L. W. Perry, and Y. J. Kaufman (2005). Retrieval of biomass combustion rates and totals from fire radiative power observations: FRP derivation and calibration relationships between biomass consumption and fire radiative energy release. *Journal of Geophysical Research: Atmospheres*, vol. 110, p. D24311. DOI: 10.1029/2005JD006318.

Chapter 2

DETECTING HIGH AND LOW-INTENSITY FIRES IN ALASKA USING VIIRS I-BAND DATA: AN IMPROVED OPERATIONAL APPROACH FOR HIGH LATITUDES¹

Abstract

Fire products from Moderate Resolution Imaging Spectroradiometer (MODIS) and Visible Infrared Imaging Radiometer Suite (VIIRS) imagery provide timely information for wildfire detection, monitoring, and characterization at the global scale. However, in Alaskan boreal forest fires, their lower effectiveness in detecting residual fire once the high-intensity fire front has passed limits their practical use for regional or local fire management decisions. Using data acquired during Alaska's 2016 fire season, we analyzed the performance of the MODIS-based MOD14/MYD14, and the more recent VIIRS I-band active fire products. A comparison with the fire perimeter and properties data published by the Alaska Interagency Coordination Center (AICC) shows that both MODIS and VIIRS fire products successfully detect all fires larger than approximately 200–300 ha. For fires smaller than this threshold, the VIIRS I-band product offers higher detection likelihood. To map burn areas containing both low- and high-intensity active fire, we developed the VIIRS I-band Fire Detection Algorithm for High Latitudes (VIFDAHL). We apply this algorithm to regions of known Alaskan boreal forest fires and validate it using events mapped by fire management agencies and detected on closely-timed Landsat imagery. We find that for Alaska, an example of a high-latitude region, VIFDAHL more accurately captures the fire spread, can differentiate well between low- and high-intensity fires, and can detect 30–90% more fire pixels compared to the MODIS and VIIRS global fire products.

¹ Article published as: Waigl, C. F., Stuefer, M., Prakash, A., & Ichoku, C. (2017). Remote Sensing of Environment, 199, 389–400. <https://doi.org/10.1016/j.rse.2017.07.003>

2.1 Introduction

Operational fire detection products from satellite-borne visible and infrared sensors have been used to track wildfire activity and inform fire managers of fire risk and hazard since they first became available in the 1980s (Ichoku et al. 2012). In the northern high-latitude regions such as Alaska, where fire affects remote, sparsely populated areas, site access or fire suppression decisions are associated with significant complexity and cost. In such areas, satellite remote sensing frequently offers the only avenue to obtain near real-time data for decision support.

In Alaska's vast boreal forest, wildfires have been reported to be increasing in frequency, severity, and extent, in part due to a rapidly changing climate regime (Collins et al. 2013; Kasischke and Turetsky 2006; Soja et al. 2007). Between 1960 and 2000, the area annually affected by fire increased from an average of 400,000 ha per year to approx. 767,000 ha per year (Kasischke et al. 2010). In the Alaskan boreal forest, stands of black spruce (*Picea mariana*), the dominant coniferous species, undergo a complete stand-replacing fire roughly every 50–500 years (ibid.). Due to the slow progress of decomposition in the sub-arctic climate a deep layer of fine organic material covers the forest floor. The combustion of this duff layer accounts for more than half of the fire-related carbon consumption and emissions in boreal forest areas (Kasischke and Hoy 2012; Kasischke et al. 2005; Randerson et al. 2006); the degree to which it is consumed impacts carbon storage (Genet et al. 2013) and the succession of species during post-fire recovery (Johnstone et al. 2010). Rapid changes in the frequency and characteristics of Alaskan wildfires therefore affect the atmospheric composition at local (Andreae and Merlet 2001; Grell et al. 2011) and hemispheric scales (Pfister et al. 2006, 2005, 2008). The investigation of some of these processes requires observational data to be available in near real time.

In 2015 Alaska witnessed an extreme fire season, with the total area burned exceeding 2.5 million ha (Roman 2015), which is six times the long-term annual average. Since the start of the Alaska Large Fires Database in 1940 (Kasischke et al. 2002) the area burned in 2015 was only exceeded during the 2004 fire season. 2015 was followed by a below-average fire season in 2016 (200,000 ha burned). These two recent fire seasons provide an excellent opportunity to investigate a variety of fires that are representative for the fire regime in the Alaskan boreal forest.

The goals of this study are to use 2015 and 2016 data as a test case:

- To investigate the performance of the principal fire products currently available for operational use in the detection and mapping of Alaskan wildfires, using fire properties and perimeter data provided by fire management agencies as reference data.
- To design and evaluate a customized fire detection algorithm suitable for Alaska and to compare its performance to the global product as well as validate it with higher-resolution data. We first provide a brief review of existing global fire detection products, introduce four study sites, and evaluate selected global fire products with ground truth data available from fire management agencies. We then present the VIIRS I-band Fire Detection Algorithm for High Latitudes (VIFDAHL), validate it using higher-resolution remote sensing data, and compare its performance with the previously evaluated global fire products.

2.2 Global active fire products: a brief review

Most global operational fire products make use of two infrared (IR) bands: one in the mid-IR (centered at a wavelength of $\sim 4 \mu\text{m}$), which corresponds to the peak of radiant emittance caused by a flaming wildfire at $\sim 1000 \text{ K}$; and a second band in the thermal IR (at $\sim 11\text{--}12 \mu\text{m}$), which is sensitive to background radiation emitted by the Earth's surface. Whenever a pixel's footprint covers the location of a wildfire, the mid-IR radiance is elevated with respect to the thermal IR radiance. Fire detection algorithms use thresholds on both the value of the mid-IR emissive signal and the difference between the mid- and thermal IR brightness temperatures. Algorithm-dependent checks serve to minimize errors of commission ("false alarms") and errors of omission ("missing fire pixels").

The Wildfire Automated Biomass Burning Algorithm (WF-ABBA), developed for fire retrieval from Geostationary Operational Environmental Satellite (GOES) and other geostationary satellites operated by European, Japanese and Korean agencies, was used to generate an operational fire detection product with a spatial resolution of 4 km at the equator as early as 1994 (Menzel and Prins 1996; Prins and Menzel 1994; Prins and Schmidt 2001). However, it was only in 2002 that a WF-ABBA based daily fire product was available operationally for the user community through

NOAA's National Environmental Satellite, Data, and Information Service (NESDIS). Sub-pixel analysis is used to retrieve the temperature and the fractional areas of fires in individual pixels (Dozier 1981; Matson and Dozier 1981).

A family of fire detection algorithms was also developed for the Advanced Very High Resolution Radiometer (AVHRR) on NOAA's polar-orbiting satellites (Giglio et al. 1999; Li et al. 2000a,b). The Fire Identification, Mapping and Monitoring Algorithm (FIMMA), which is available at NESDIS, is specifically aimed at the detection of forest fires, as it relies on land cover data among its inputs to complement the AVHRR bands 2 (0.9 μm), 3b (3.7 μm), 4 (10.8 μm) and 5 (12 μm) that are used.

Following the launch of the National Aeronautics and Space Administration's (NASA's) Earth Observing System (EOS) suite of satellites beginning in 1999, the Moderate Resolution Imaging Spectroradiometer (MODIS) sensors offered new opportunities for advancing fire detection and characterization. MODIS data are used to generate the currently best-validated active fire detection products, MOD14 and MYD14 (from the Terra and Aqua spacecraft, respectively), at a spatial resolution of 1 km at nadir (Justice et al. 2002; Kaufman et al. 1998). Originally described by Kaufman et al. (1998), the MODIS operational algorithm version has since evolved from collections 2, 3, 4, and 5 (Giglio et al. 2003) up to the current collection 6 (Giglio et al. 2016). MODIS acquires data in 36 spectral bands, ranging from visible and near infrared (VNIR) to shortwave infrared (SWIR), mid-infrared (MIR) and thermal infrared (TIR). 29 of the 36 spectral bands are acquired at a ground-sampling distance (GSD) of 1 km at nadir. Off-nadir, pixel footprints grow to approximately 2×5 km at the swath edge. Active fire detection makes use of two channels centered at 3.96 μm (band 21 and the more sensitive band 22, which saturates at a lower brightness temperature) and the TIR channel 31, which is centered at 11 μm .

The Visible Infrared Imaging Radiometer Suite (VIIRS) on the National Oceanic and Atmospheric Administration's (NOAA's) Suomi National Polar-orbiting Partnership (Suomi NPP) platform (Cao et al. 2014) was launched in late 2011 under the Joint Polar Satellite System (JPSS), which is a joint program managed by both NOAA and NASA. A fire detection algorithm based on the moderate-resolution ("M") bands (GSD 750 m at nadir) uses the dual-gain band M13 (3.973–

$4.128\text{ }\mu\text{m}$, with saturation temperatures of 343 K and 634 K) and the single-gain band M15 ($10.263\text{--}11.263\text{ }\mu\text{m}$) (Csiszar et al. 2014). A second algorithm, devised by Schroeder et al. (2014) uses the bands optimized for imaging (“I” bands, GSD 375 m at nadir), specifically I4 (centered at $3.74\text{ }\mu\text{m}$) and I5 (centered at $10.45\text{ }\mu\text{m}$). Polivka et al. (2016) have proposed the Firelight Detection Algorithm (FILDA), which combines VIIRS M-band infrared data with the visible light signal from the near-constant contrast Day-Night Band (DNB) (Liang et al. 2014) for improved night-time fire detection.

Csiszar et al. (2006) validated the MODIS active fire products using simultaneous higher-resolution data from the Advanced Spaceborne Thermal Emission and Reflection Radiometer (ASTER) on the Terra platform for wildfires in the Eurasian boreal forest in Siberia. They found that, due to the thick smoke observed in Siberian boreal forest fires, the footprint of a $1\times 2\text{ km}$ MODIS pixel needs to contain one third more 30 m ASTER fire detections than required for fires in the Brazilian Amazon (60 vs. 45) to achieve a probability of 50% for the pixel to be flagged as “fire”. Schroeder et al. (2008) validated WF-ABBA and the MODIS products using ASTER and Landsat ETM+ over Amazonia. A different approach to validation consists in the comparison of the output from newer products to existing ones. Thus, Schroeder et al. (2014) compared the new VIIRS 375 m I-band global product to MOD14/MYD14 and to the VIIRS M-band product, by sampling 12 zones across the globe for one month (August 2013). Two of these zones are in the boreal region, one over Canada, one over Russia. For these zones, errors of commission do not exceed 0.04% (*ibid.*). Direct comparison with MODIS as well as higher-resolution sensors was carried out for fire events in California, Brazil, and Australia, but no locations in the boreal forest were selected for detailed investigation.

2.3 Wildfire study areas

In this study we use four selected study sites (Fig. 2.1) to generate and validate a new Alaska-specific VIIRS I-band based fire product. They represent distinct situations in which fire was active during the 2015 or 2016 Alaska fire seasons. For these sites, cloud-free Landsat 8 Operational Land Imager (OLI) data that was closely timed with one of the VIIRS overpasses in our dataset was available.

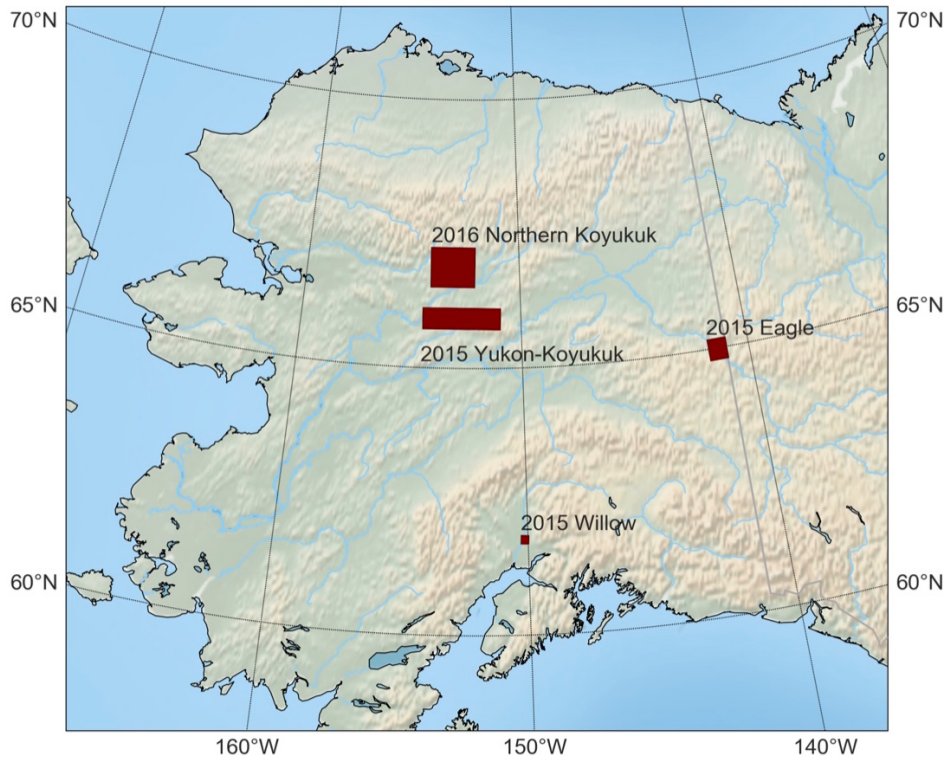


Figure 2.1: Location of the four 2015 and 2016 wildfire study areas within Alaska: Willow (Sockeye fire), Eagle (Seventymile and Trout fire), and two areas within the northern Yukon-Koyukuk basin which saw multiple large-scale and high intensity wildland fire events during both July 2015 and 2016.

2.3.1 Willow: Sockeye fire, June 2015

A human-caused wildfire started on the northern outskirts of the town of Willow, southcentral Alaska, on June 14, 2015. High winds and dry weather conditions caused the fire to rapidly grow and spread southwards. Numerous buildings were destroyed. The area north of Willow consists mainly of mature black spruce forest, interspersed by birch and balsam poplar and bordered by alluvial plains covered in grass and brush. The Susitna River borders the area in the west.

Unlike most Alaskan boreal forest fires, the road-accessible Sockeye fire was vigorously suppressed. Thus, significant flaming fire activity was limited to less than one week. We selected this fire site as it offers a diversity of surface characteristics and fuels that were likely to cause false positive detections in the new Alaska-specific algorithm. This is due to the extensive bare,

dry, highly reflective sand banks along the Susitna river as well as an old fire scar in the vicinity. Cloud cover also varied widely throughout the active phase of this fire event.

The geographic extent of this study area is latitude 61.7–61.9°N, longitude 150.0–150.1°W.

2.3.2 Yukon-Koyukuk: multiple wildfires, July 2015

During the last third of the month of June 2015, with hot, dry, windy weather continuing in western interior Alaska, multiple wildfires were ignited by lightning across the rural areas of northern Yukon-Koyukuk region. These fires offer an excellent test case for fire detection and mapping, in particular for large-scale, high-intensity burns in a remote area with little infrastructure and predominately black spruce forest. We include the following large fire events: Sushgitit Hills (discovered June 21, final area 126,633.5 ha), Rock (June 19, 57,728.6 ha), Torment Creek (June 20, 33,359.1 ha), Tobatokh (June 22, 21,867.6 ha), and Holonada (June 22, 19,496.2 ha). Detections from neighboring fire perimeters that were active at the same time (Bandana Creek and Isahultila) are sometimes present at the edge of the study area. The fires remained active from the time of ignition to mid-August, when wet weather ended large-scale wildfire activity.

We selected this site because the fire events generated a large amount of data (N1000 detections in a single acquisition), with high fire intensity, and abundant smoke and clouds. As the area is remote and sparsely populated the fires were classified in the “limited” management option by the fire protection agencies and essentially left unsuppressed. The only exception is the Rock fire, in the “full” management option, due to its proximity to the village of Hughes on the banks of the Koyukuk River. The VIIRS data for this area contain numerous test cases for data anomalies due to sensor saturation and intense signals.

The geographic extent of this study area is latitude 65.75–66.1°N, longitude 150.9–154.5°W.

2.3.3 Eagle: early-season wildfires, May 2015

We further selected a small area north of the town of Eagle, AK, which was affected by early-season lightning-ignited fires in late May 2015. The area is mountainous, largely covered by

either black spruce forest or alpine tundra interspersed with rocky outcrops. The Seventymile fire (1175 ha) was located approximately 10 km northwest of Eagle, and the Trout fire (106.7 ha) was a smaller nearby event.

The geographic extent of this study area is latitude 64.75–65.17°N, longitude 140.95–141.75°W.

2.3.4 Northern Koyukuk: multiple large fires, July 2016

From the 2016 fire season we selected a study area containing several of the largest fires of 2016, during a short period of particularly intense fire activity: Hog (discovered July 5, 23,700.5 ha), Hogaza River (June 26, 21,179.1 ha), Iniakuk Lake (June 25, 14,872.0 ha) and Bedrock Creek (July 3, 2650 ha).

The geographic extent of this study area is latitude 66.5–67.25°N, longitude 152.1–154.2°W.

2.4 Data

This study required data from the northern high latitudes. While on the one hand overlapping tracks of polar orbiting satellites provide more coverage (and thus more frequent data) in higher latitudes, poorer computer network infrastructure still poses challenges for reliable and quick data transmission from mid-latitudes to higher-latitude areas for near real-time applications. However, local data downlink stations in the high latitudes provide an opportunity to overcome this challenge. Even though this work is based on data from NOAA and NASA data repositories, it was undertaken with a view towards future operational use based on processing locally downlinked data to detect and map fires, and tailor the fire products to regional and local needs.

2.4.1 Global MODIS and VIIRS I-band products

We downloaded MODIS and VIIRS I-band fire detection data from the Land, Atmosphere Near real-time (NRT) Capability for EOS (LANCE) system, specifically the Fire Information for Resource Management System (FIRMS) [<https://earthdata.nasa.gov/firms>]: The near real-time VIIRS 375 m I-band Active Fire product VNP14IMGT (DOI: 10.5067/FIRMS/VIIRS/VNP14IMGT. NRT.001) and the MODIS Collection 6 NRT Hotspot/Active Fire Detections MCD14DL (DOI:

10.5067/FIRMS/MODIS/MCD14DL.NRT.006). At the time of writing, availability of the VIIRS 375 m I-band product via NASA’s portals begins in January 2016. Therefore, we used the 2016 fire season for the evaluation of global fire products. After limiting the data to the geographic extent of Alaska, the dataset contained:

- MODIS (based on MODIS Terra and Aqua): 3,769 detected hotspots
- VIIRS I-band (375 m, based on VIIRS on Suomi NPP): 11,091 detected hotspots.

Each data record represents the latitude and longitude of a fire detection associated with the following attributes: timestamp and brightness temperature measurements, the along-scan and along-track linear extent of the fire pixel’s footprint on the ground, a confidence index, and fire radiative power.

Regarding the three 2015 study areas, we were also able to obtain NASA-processed VIIRS 375 m I-band active fire data for selected days in 2015, courtesy Wilfrid Schroeder (University of Maryland and NOAA/NESDIS Center for Satellite Applications and Research).

2.4.2 VIIRS Sensor Data Record (SDR) data

We based the design of an Alaska-specific VIIRS I-band fire detection algorithm on VIIRS at-sensor brightness temperature swath data. For this study, we used VIIRS Sensor Data Record (SDR) data from NOAA’s Comprehensive Large Array-data Stewardship System (CLASS) data portal. Throughout the entire active fire phase of our two smaller study areas (Willow and Eagle), all available VIIRS SDR datasets, with the exception of those dominated by cloud cover or lacking any active fire, were analyzed. For the large-scale study areas (Yukon-Koyukuk and Northern Koyukuk), the analysis is based on the one or two VIIRS scenes that coincide with the available Landsat 8 data. For later operational use, locally downlinked and processed data from the Geographic Information Network of Alaska (GINA) at the University of Alaska Fairbanks (UAF), a data provider that operates an X-band direct read-out station, will be available. VIIRS SDR data is provided as HDF5 data files aggregating multiple bands and 86-second granules, plus

terrain-corrected geodata layers for each granule and each sensor band group (I-bands, M-bands and Day-Night-Band).

The swath acquired by VIIRS is 3040 km wide, 30% wider than a MODIS swath (2330 km). The Suomi NPP orbit closely follows that of Aqua (in the “A-train”), but at an orbit that is >100 km higher. Like Aqua, Suomi NPP makes early afternoon overpasses on an ascending node each day. The repeat interval is 16 days, the same as Aqua and Terra, so orbital tracks vary from day to day. At a minimum, two good daytime and two good nighttime overpasses can be expected daily for any location in interior Alaska.

2.4.3 Fire location and perimeter data

To evaluate the fire detections against a measure for “true” fires, we used the 2016 (and, limited to the study areas, 2015) additions to the Alaska Large Fires Database (ALFD) (Kasischke et al. 2002) from the AICC’s Geographic Information System (GIS) portal (<http://afsmaps.blm.gov/imf/imf.jsp?site=firehistory>). The 2016 dataset consists of a Shapefile containing 155 fire perimeters, in a geographic coordinate system using the NAD83 datum. AICC also distributes an additional “Fire Locations” file, which provides point data for the initial location of all events managed by AICC during the fire season; this is a superset of the fires in the ALFD. For 2016, after removing events marked as false alarms, there are 592 such fire locations. The GIS files are updated approximately daily during the fire season; they were retrieved in their final form in 2017, after the 2016 season ended.

Table 2.1: Overview of VIIRS swath data scenes that were used for each study area.

Study Area	Number of VIIRS SDR granules used	Start date	End date
Eagle	5	2015-05-27	2015-05-29
Willow	19	2015-06-14	2015-06-19
Yukon-Koyukuk	1	2015-07-06	2016-07-06
Northern Koyukuk	2	2016-07-15	2016-07-15

The attribute information (Table 2.2) published by the AICC includes dates (first detection, last management action, date the fire was confirmed “out”), environmental factors (fire cause, primary fuel, total burned area in acres) and management related information, such as false-alarm flags.

Table 2.2: GIS attributes in the AICC and global fire product datasets that were used in this study. Attribute names are truncated from the names used within the AICC’s database.

File	Field name	Description
AICC perimeters	CalcAcres	Final total area of the burn perimeter, in acres
	FireName	Name of fire (text label)
	DiscDate	Date on which fire was discovered (AKDT)
	ControlDate	Date on which fire was under control
	OutDate	Date on which fire was extinguished
	FalseAlarm	Flag marking false alarm fires
	GenCause	Fire cause (human or lightning)
	Comment	Plain text comment relating to the provenance of perimeter geometry data
MODIS, VIIRS-I	ACQ_DATE	Date of detection (UTC)
	ACQ_TIME	Time of detection (UTC)

Table 2.3: Landsat and VIIRS scenes used for validation of the AK-specific VIIRS I-band fire detection scheme.

Landsat scene ID	Landsat datetime (UTC)	VIIRS orbit	VIIRS granule ID	VIIRS granule start time (UTC)	Study area
LC80650142015147LGN00	2015-05-27 20:47:22	18565	NPP001135168656	2015-05-27 20:45	Eagle
LC80700172015166LGN00	2015-06-15 21:19:17	18820	NPP001150756980	2015-06-15 21:28	Willow
LC80730142015187LGN00	2015-07-06 21:36:48	19118	NPP001168905804	2015-07-06 21:36	Yukon-Koyukuk
LC80740132016197LGN00	2016-07-15 21:43:04	24438 24439	NPP001492885869 NPP001492947321	2016-07-15 20:58 2016-07-15 22:41	Northern Koyukuk

During pre-processing we confirmed that none of the 155 fires from the ALFD are marked as false alarms. Inspection of the fire events without corresponding fire perimeter shows that such fires are typically very small (b1 ha) human-caused fires, often in residential or industrial areas, and that data available for them may be incomplete. Given our interest in wildland fires we only analyzed fires for which a perimeter is available, that is, the 155 ALFD fire events.

During the active management phase of a fire event, operational fire detections from VIIRS and MODIS are among the data sources used to update fire perimeter geometries. However, at the end of a fire event the final perimeter data is corrected using the best available source, such as aerial GPS surveys or digitization of Landsat fire scar imagery (Jennifer Jenkins, Alaska Fire Service GIS manager, personal communication). In the 2016 data, 66 final perimeters (43%) were generated from Landsat 8 imagery, 16 (10%) from aerial survey data, 34 (22%) were provided by operational teams affiliated with the Alaska Department of Forestry or the National Park Service, 26 (17%) from various operational sources, and 13 (8%) were lacking provenance information. Out of the 10 largest fires, 8 perimeters relied on Landsat 8 data.

2016 fire areas range from 0.2 ha to 23,700.5 ha, with a mean of 1293.7 ha and a median of 83.5 ha. Six fire events exceeded 10,000 ha. The 2016 fire season was below-average, with many relatively small fires. As a point of comparison, for the extreme 2015 fire season we count 334 fire perimeters with a mean area of 6236.2 ha, a median of 1128.5 ha and a maximum of 126,633.5 ha. 133 out of 155 2016 fire events (86%) were labeled as caused by lightning, compared to only 22 (14%) human-caused fires. Typically, only few large wildland fires are caused by human action in interior Alaska. To be able to compare and measure distances, we re-projected the geospatial coordinate information in the fire events and the fire detection datasets to the Alaska Albers Equal Area projection.

2.4.4 Landsat 8 imagery

To validate the Alaska-specific VIIRS fire detection algorithm, we used three Landsat 8 OLI images that were acquired within minutes of an available VIIRS granule of the same location 2.3. For the 2016 Northern Koyukuk study area, for which the time lapse between Landsat and the two closest VIIRS overpass times is approximately 45 min and 58 min, respectively, Landsat fire detections were not suitable to validate VIIRS-based detections and are therefore used for visualization purposes only.

2.4.5 Evaluation of operational MODIS and VIIRS I-band products

For each of the 155 ALFD fires we counted the hotspot detections that are located within a buffer of 1 pixel (at nadir) around the fire perimeter: 375 m for VIIRS and 1 km for MODIS data. Furthermore, we required detection time stamps to fall between the “discovery date” and either the “out date” or, if unavailable, the “control date” attributes of the fire event. The buffer was used to ensure that fire pixels whose centers lie just outside the recorded perimeter are correctly counted. The footprint of a MODIS fire pixel is 1×1 km at nadir, but can become stretched to a maximum of 2×5 km at the swath end. VIIRS I-band pixels are nearly square with a side of 375 m, and grow by a factor approximately 2 towards the swath edge. The resulting dataset was then statistically analyzed to compare the performance of VIIRS I-band and MODIS hotspot counts and to evaluate their spatio-temporal distribution.

2.4.6 VIIRS I-band Fire Detection Algorithm for High Latitudes (VIFDAHL)

Our processing scheme ingests VIIRS data that are locally downlinked and processed to the SDR processing level (Figure 2.2); it is based on the following design goals:

- all fire pixels correctly detected by the global VIIRS I-band product must also be detected by VIFDAHL
- saturated pixels due to fire-related radiance are detected as fire
- the product is superior to the global VIIRS I-band product in detecting residual fire behind the fire front
- fire detections are classified into high- and low-intensity fire pixels
- false-detection filters are optimized for sources typically found in Alaska, specifically sand banks and old fire scars
- duplicate detections due to the bowtie effect are removed

We generate the resulting detection product as a polygon vector dataset in order to preserve the extent of the pixel footprint.

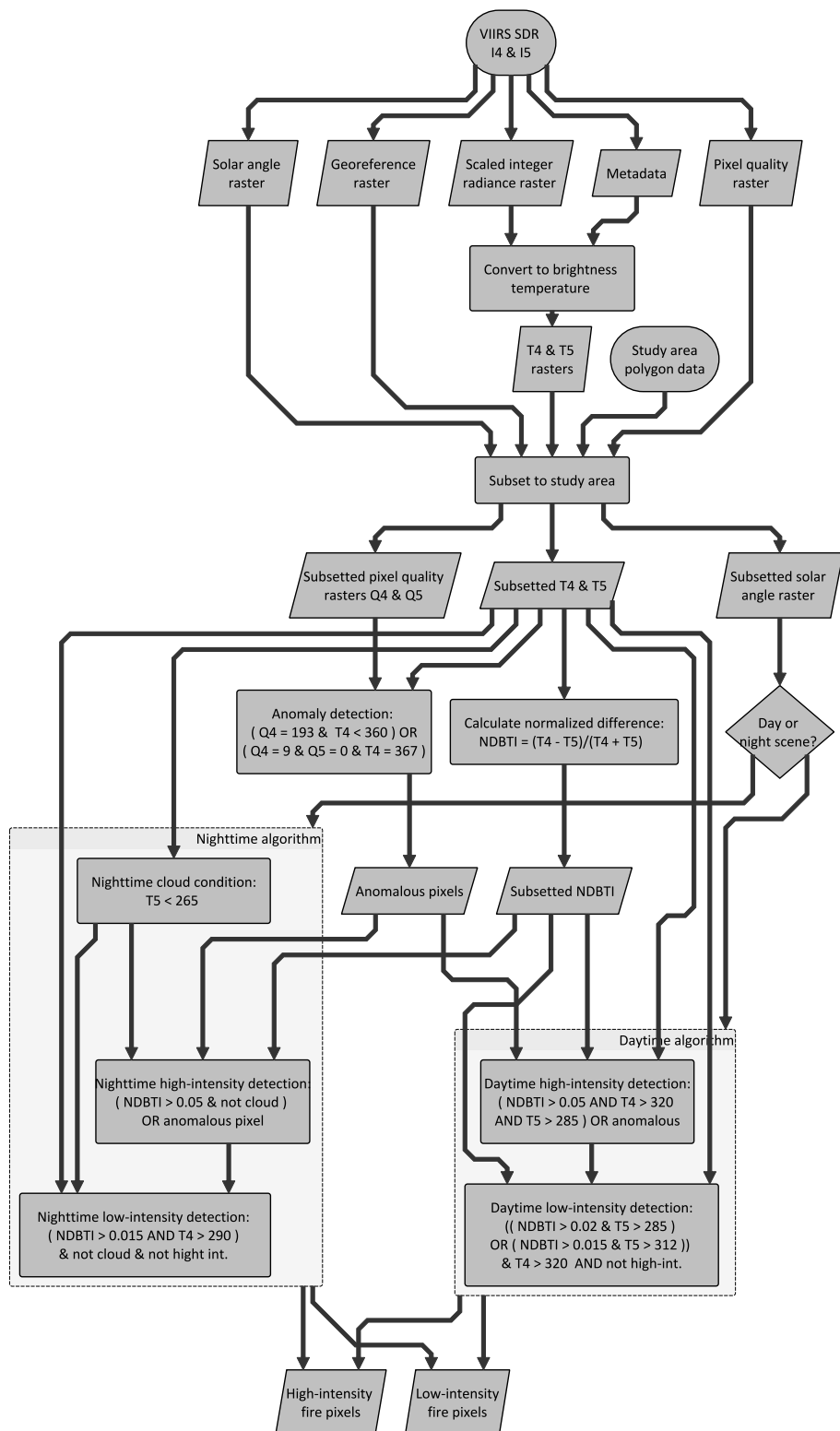


Figure 2.2: VIFDAHL (VIIRS I-band Fire Detection Algorithm for High Latitudes) processing workflow.

The scaled integer data in bands I4 (centered at 3.74 μm) and I5 (11.45 μm) were converted to at-sensor brightness temperature T4 and T5 (Schroeder et al. 2014). As in other fire detection algorithms, VIFDAHL relies on a large difference in the I4 and I5 brightness temperatures (T4, T5); pixels that have no elevated T4 or appear cold in T5 (cloud, water) are excluded. In order to remove highly reflective riverbanks, we need the thermal signal to be elevated as well. To ensure that thresholds apply across meteorological conditions, we calculate a Normalized Difference Brightness Temperature Index (NDBTI):

$$\text{NDBTI} = \frac{T_4 - T_5}{T_4 + T_5} \quad (2.1)$$

NDBTI values for a typical active fire are shown in Figure 2.3: Fire pixels show elevated NDBTI values, with the active fire front clearly distinguished from residual fire within the fire perimeter. Potential sources of false detections are the sandy banks of the river visible to the left of the fire and a ten year old fire scar in the top left corner. We used a minimum in the NDBTI frequency distribution close to 0.05 to delineate low- and high-intensity fire areas. Due to the risk of false detections in locations that are in reality highly-reflective river banks, we added a check for elevated T5 ($>312\text{ K}$) for daytime images. The thresholds for absolute values of T5 and T4 have been fixed via a grid search and sampling across the test scenes (Table 2.1): we maximize the detections within the known fire perimeter up to the point where false detections start to appear in the known non-fire areas. For each test scene, the entire VIIRS swath, subsetted to the extent of Alaska, was checked for false detections not associated with a known fire.

A second consideration relates to artifact conditions associated with fires. To assess them, we considered the pixel quality rasters for both band 4 and band 5 (Stevens 2014). These are 1-byte raster bands of the same extent as their respective radiance swaths. The single byte encodes four separate 2-bit quality flags for each pixel as shown in Table 2.4. For nominal data, the value 0 (=00|00|00|00) would be expected.

In the Yukon-Koyukuk study area we found the following anomalous pixel quality values:

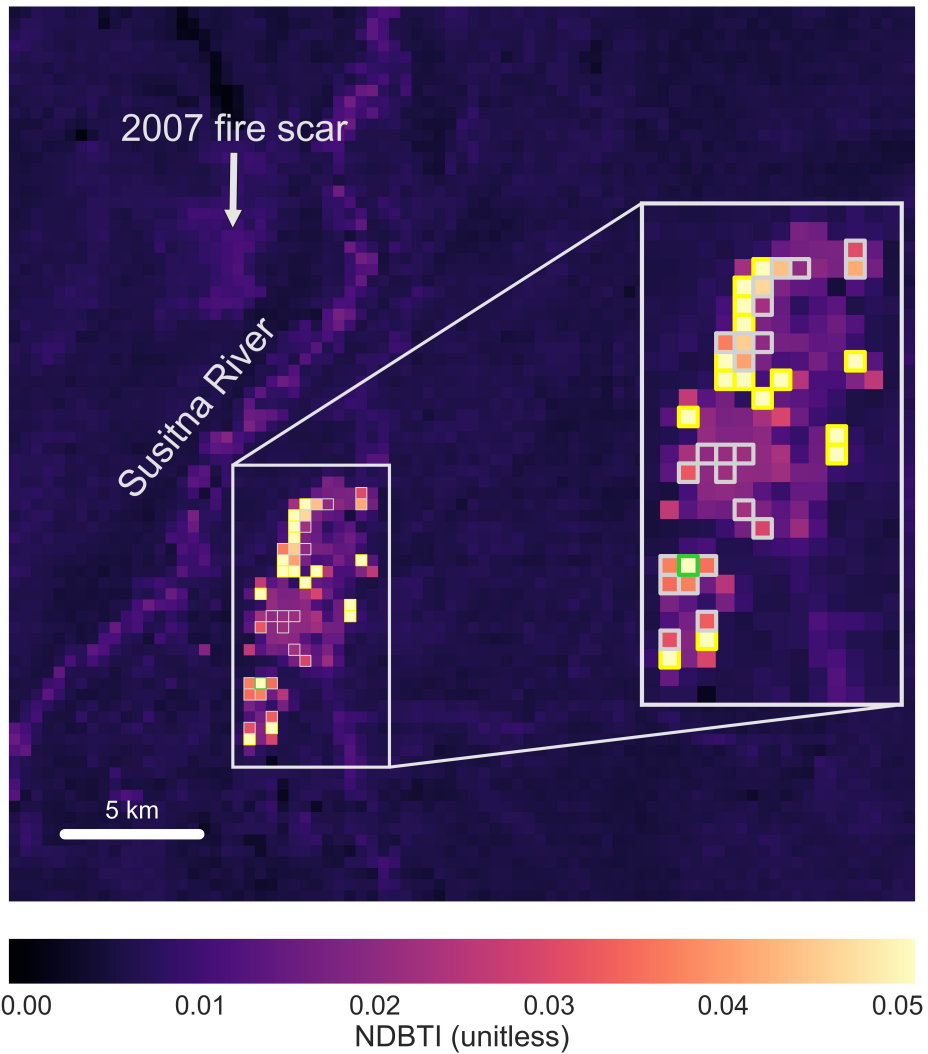


Figure 2.3: Willow study area, Sockeye fire 2015-06-15, 15:09 AKDT: Normalized Difference Brightness Temperature Index (NDBTI) from VIIRS I-band data, overlaid with VIFDAHL detections: high-intensity (yellow outline), low-intensity (gray outline), saturated (green outline). VIFDAHL was tuned to avoid false positive detections along the sun-heated riverbanks of the Susitna as well as for the fire scar of the 2007 Su River fire, despite the elevated NDBTI values in these areas. The center of this scene is at latitude 61.84°N, longitude 150.1°W.

- 2 = 00|00|00|10 (“no calibration”) in both bands I4 and I5. These are essentially no-data pixels, located towards swath edge, and represent bowtie removal.
- 9 = 00|00|10|01 in band I4: “poor calibration, all saturated”
- 65 = 01|00|00|01 in band I5: “poor calibration radiance out of range” (used for I5)
- 193 = 11|00|00|01 in band I4: “poor calibration, radiance and reflectance out of range”

Table 2.4: VIIRS I-band pixel anomalies illustrated for a subset of the 2015 Yukon-Koyukuk study area on 2015-07-06. Left: mid-IR brightness temperature (band I4). Right: thermal IR brightness temperature (band I5). Pixels that saturate in I4 appear white (left) and are outlined in blue; the corresponding I5 brightness temperature is within the normal range (nominal quality). Anomalous pixels that appear black (left) and are outlined in green correspond to a “fold-over” of the digital number; all but two of these (white arrows) have nominal quality brightness temperatures in I5.

2 bits: calibrated pixel value outside look-up table limits	2 bits: data required for calibration missing	2 bits: level of pixel saturation	2 bits: calibration quality
00 all within range	00 no missing data	00 none saturated	00 good calibration
01 radiance out of range	01 Raw Data Record missing	01 some saturated	01 poor calibration
10 reflectance or brightness temperature out of range	10 calibration data missing	10 all saturated	10 no calibration
11 both out of range	11 thermistor data missing	11 not used	11 not used

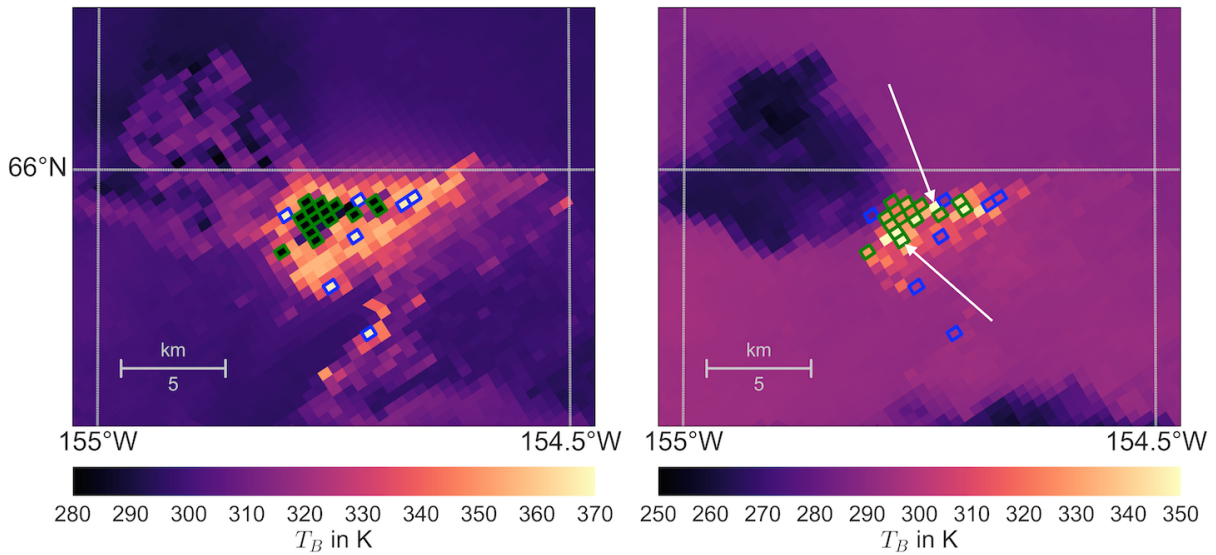


Figure 2.4: VIIRS I-band pixel anomalies illustrated for a subset of the 2015 Yukon-Koyukuk study area on 2015-07-06. Left: mid-IR brightness temperature (band I4). Right: thermal IR brightness temperature (band I5). Pixels that saturate in I4 appear white (left) and are outlined in blue; the corresponding I5 brightness temperature is within the normal range (nominal quality). Anomalous pixels that appear black (left) and are outlined in green correspond to a “fold-over” of the digital number; all but two of these (white arrows) have nominal quality brightness temperatures in I5.

As is the case for the wildfires in the contiguous United States examined by Schroeder et al. (2014), the T4 brightness temperature associated with Q4=9 was at its maximum value (367 K),

whereas $Q_4=193$ indicates folded values caught at the lower end of the permissible data range ($T_4 = 208$ K). In a small number of pixels we found $Q_5=65$ associated with $Q_4=193$ and a saturated T_5 (see white arrows in Figure 2.4). Whenever $Q_4=9$ or $Q_4=193$, the pixel is counted as a high intensity fire pixel by VIFDAHL, but the brightness temperature value for these pixels is not providing any meaningful information. Furthermore, Figure 2.4 also shows some pixels that appear dark in the T_4 plot, and for which T_5 shows elevated temperatures; but Q_4 and Q_5 are both zero (nominal quality, no green outline) even though T_4 is likely to be anomalous. VIFDAHL does not include a test that flags these as fire pixels.

2.4.7 Validation using Landsat 8

To validate VIFDAHL we used near-simultaneous Landsat 8 OLI imagery. We implemented the fire detection algorithm described in Schroeder et al. (2015), which uses spectral reflectance in the OLI SWIR bands (B5 and B7) to preselect “unambiguous” and “marginal” fire pixels and then re-examines the “marginal” pixels using contextual tests on the B7 reflectance and the B7/B5 reflectance ratio using a 61 by 61 pixel window.

2.5 Results

2.5.1 Exploratory data analysis of operational MODIS and VIIRS I-band fire detection datasets

Neither of the two global fire products is able to detect all 2016 ALFD wildfires: MODIS failed to detect 45% and the VIIRS 375 m I-band product failed to detect 35% fires. These relatively elevated percentages are due to the small size and short burn duration of most 2016 fires, and cloud conditions. As summarized in Table 2.5, the VIIRS I-band product detects more fires than the MODIS product, offers an improvement in the detection of smaller fires, and detects numerous thermal anomalies that are not wildfire, but instead associated with the Prudhoe Bay oil fields on the North Slope of Alaska, or volcanic eruptions in the Aleutian arc. A small percentage of detections (2% for VIIRS, 3.3% for MODIS) remain unassigned to either an ALFD wildfire or another known source. Approximately 40% for VIIRS (85 out of 224) and half for MODIS (63 out of 126) are located within 5 km of a fire perimeter and are therefore likely to be associated with it.

The remainder consists in a mix of industrial hotspot and sporadic detections of unknown origin, more commonly found for the more sensitive VIIRS.

Table 2.5: Overall detection performance of MODIS and VIIRS I-band fire products for detection of 2016 Alaska wildfires

Fire product	Number of undetected fires	% undetected fires	Size largest undetected fire (ha)	Max. fire pixels for one fire	% fire pixels assigned to oil exploration and volcanic eruptions	% unassigned detections
MODIS	70	45	331	440	0.3	3.3
VIIRS I-band	55	35	196	1,323	3.9	2.0

Table 2.6: Comparison of VIFDAHL with the global VIIRS I-band product and with Landsat 8 fire detections

Study area	VIIRS I-band (global product) detections	VIFDAHL high intens. fire detections	L8 detections per VIFDAHL high intensity pixel: mean (std)	VIFDAHL low intens. fire detections	L8 detections per VIFDAHL low intensity pixel: mean (std)
Willow 2015	15	11	18.7 (12.5)	11	12.7 (19.1)
Eagle 2015	7	8	28.3 (19.9)	1	2 (n/a)
Yukon-Koyukuk 2015	633	745	14.6 (30.5)	325	7.9 (21.1)
Northern Koyukuk 2016, scene 1	440	458	n/a	388	n/a
Northern Koyukuk 2016, scene 2	1006	1143	n/a	791	n/a

The number of VIIRS I-band fire pixels per fire is generally greater than the number of MODIS pixels because of the much higher resolution of VIIRS I-band (375 m) relative to MODIS (1 km). The relationship is strongly linear ($r^2 = 0.93$, see Figure 2.5), and there are on average 2.9 times the number of VIIRS detections for a fire event as MODIS detections (95% Confidence Interval (CI) for the slope: [2.83, 3.02]). There is a roughly linear relationship between a fire's size and the number of fire detections contained within it (Figure 2.5). From linear regression we find an average of 1.63 MODIS detections (95% CI: [1.51, 1.74], $r^2 = 0.84$) for each square kilometer of final area burnt, and 4.66 VIIRS I-band detections ([4.26, 5.06], $r^2 = 0.78$).

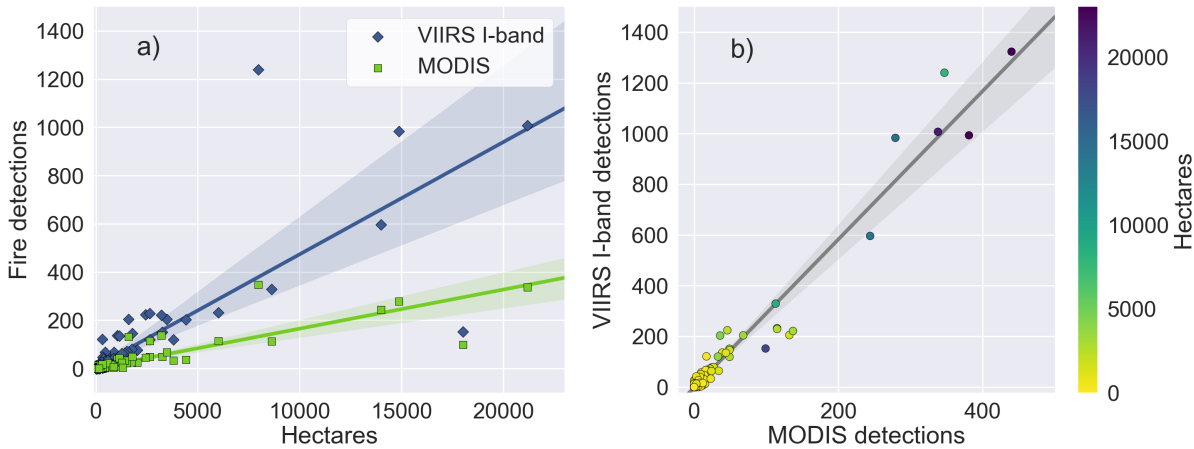


Figure 2.5: Global VIIRS I-band (375 m) vs. MODIS (both Terra and Aqua) fire detection counts. A point represents a fire event of the Alaska Large Fire Database for 2016 (155 fire events). a) Number of fire detections vs. fire area. Linear regression yields an average of 1.6 MODIS detections ($r^2 = 0.84$) and 4.7 VIIRS I-band detections ($r^2 = 0.78$) per km 2 of fire area. b) There is a strongly linear relationship between the number of VIIRS I-band and MODIS detections for each fire ($r^2 = 0.96$, slope = 2.9). The 95% confidence intervals are indicated as shaded.

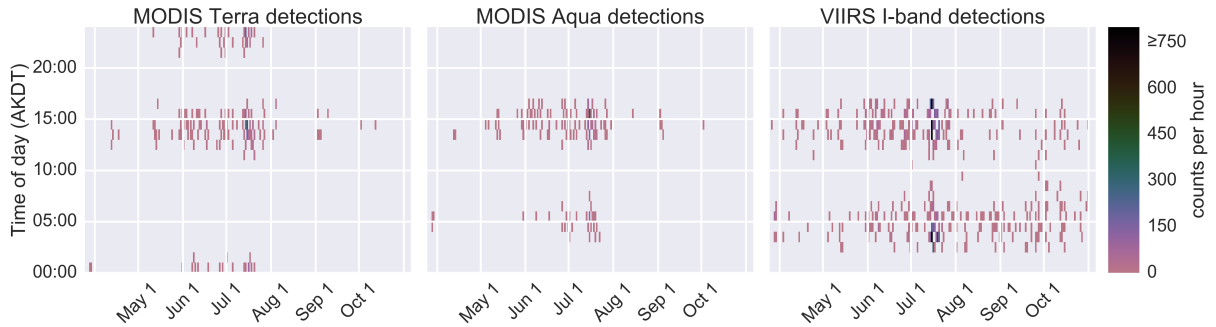


Figure 2.6: Hourly detection counts across the Alaska 2016 fire season for global fire products: MODIS Terra, MODIS Aqua and VIIRS I-band (375 m) detections. Hourly counts only show a spike in July and otherwise stay low (<100). MODIS detections generally fall off in August, while the higher sensitivity of VIIRS still supplies active fire data. The banding of detection timing is due to the temporal grouping of satellite overpasses. For MODIS Terra, mid-day/early afternoon overpasses occur on a descending node, and late evening overpasses on an ascending node; for MODIS Aqua and VIIRS on Suomi NPP, the early afternoon overpasses occur on an ascending node and the early morning overpasses on a descending node. (All times of day are in Alaska Daylight Time.)

After early August, when rain inhibited the fire activity (Figure 2.6), MODIS detections are much reduced. VIIRS I-band still provides some fire detections, especially at night. Some of the VIIRS detections can be attributed to industrial fires or wildfires too small to be in the ALVD perimeter dataset. Finally, the geographic distribution of fire detections is dominated by and

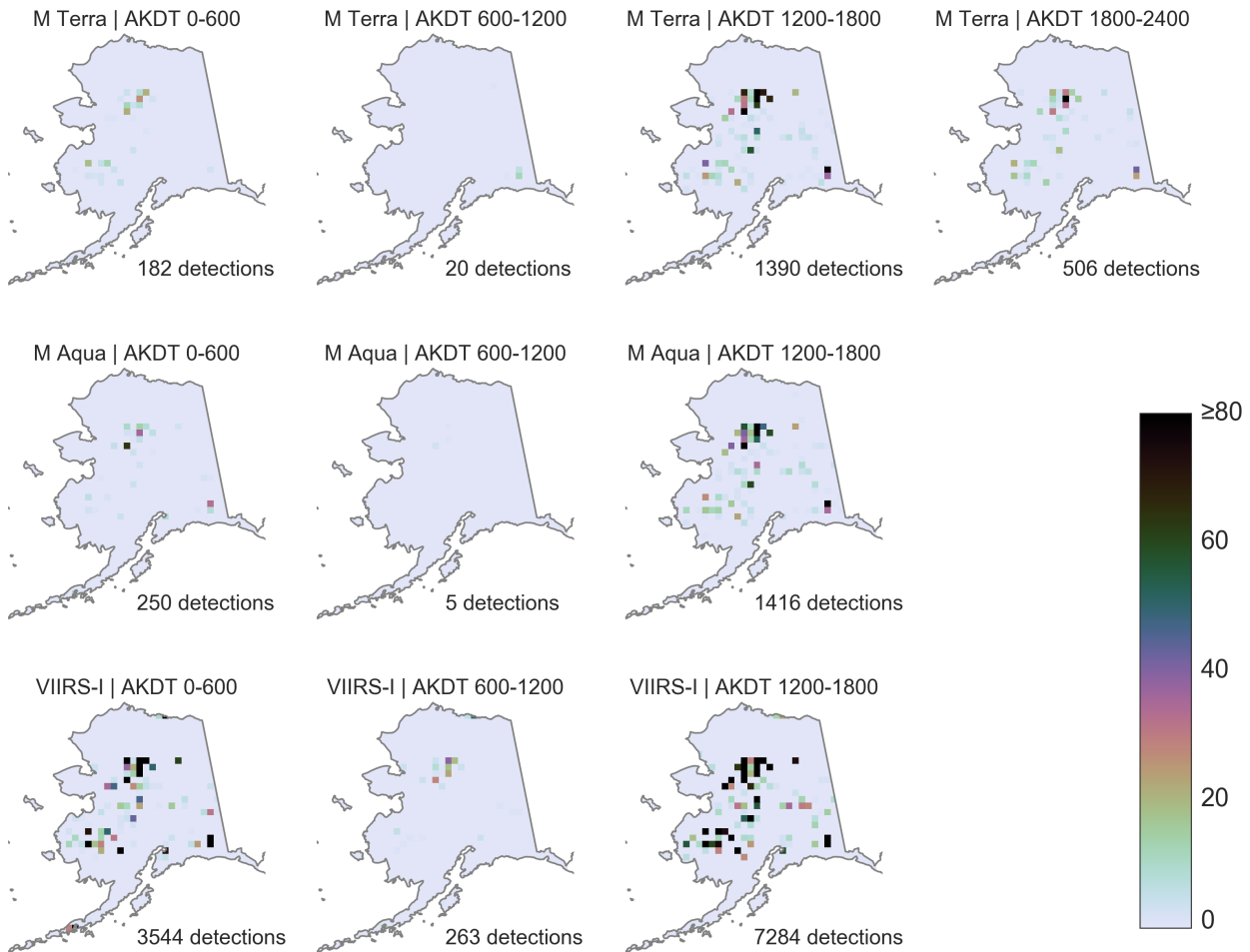


Figure 2.7: Spatio-temporal distribution of fire detections from global active fire products, in Alaska Daylight Time, during the 2016 fire season, aggregated to a 25 by 25 km grid. Top row: MODIS Terra. Middle row: MODIS Aqua. Bottom row: VIIRS on SUOMI NPP. There are no fire detections for MODIS Aqua or NPP/VIIRS during the 18:00 to 24:00 time slot.

clustered around the timing of overpasses. For overpasses for which only the swath-edge overlaps with Alaska, fires in some geographical areas are likely to be missed by the sensor. These variations are entirely independent of the processing algorithm and rely only on the orbital and swath characteristics (Figure 2.7). The narrower range and timing of potential overpass times of VIIRS compared to MODIS can in some cases lead to a short-lived fire receiving more MODIS than VIIRS I-band detections.

2.5.2 VIIRS I-band Fire Detection Algorithm for High Latitudes (VIFDAHL)

We validated VIFDAHL using near-simultaneous Landsat scenes listed in Table 2.3. For the Willow study area, on June 15, 2015 and the Eagle study area on May 27, 2015, the corresponding Landsat scenes were acquired within 9 and 2 minutes, respectively, of the VIIRS granule. For the Yukon-Koyukuk study area, this lapse is approximately 1 minute. Spatially, VIFDAHL detections show an excellent match with Landsat detections. There is no obvious co-registration error between the Landsat and the VIIRS footprints (Figure 2.8a and b show close-up imagery).

In freshly burned areas, which contain smoldering and residual flaming fires, we tend to find detections of low-intensity fire. There is no false signal from riverbanks or old fire scars in any test scene, but there are areas where sporadic Landsat fire detections are present without a corresponding VIFDAHL detection. For the Willow study area (N=22 VIIRS detections), the mean Landsat fire pixel count for a VIFDAHL high-intensity pixel is 18.7 (standard deviation: 12.5), and for a low-intensity pixel 12.7 (std: 19.1). For the Eagle case, we identify 9 fire pixels (8 high-intensity, 1 low-intensity). High-intensity VIFDAHL pixels contain higher numbers of Landsat fire pixel than low-intensity fire detections (Table 2.6). Landsat pixel counts were not carried out for the Northern Koyukuk case, as the time lapse between Landsat 8 and VIIRS overpass was too great and the fires too fast-moving for the result to be meaningful.

VIFDAHL detections were compared with the global VIIRS I-band (375 m) product for all four study areas (Table 2.6). Overall, high-intensity VIFDAHL detections closely approximate VIIRS I-band fire pixels (Figure 2.8 a-b, Figure 2.9 b-d). In addition, VIFDAHL delivers a second set of detections of less intense fire, predominantly in areas that contain Landsat 8 fire detections but no VIIRS I-band (or high-intensity VIFDAHL detections). Not all low-intensity VIFDAHL detections contain Landsat 8 detections. While it is not at present possible to exclude that VIFDAHL may falsely detect areas where a fresh fire scar is still hot, but extinguished, possible alternative reasons for the absence of Landsat detections are: the shorter wavelength of Landsat's SWIR bands, which is more affected by smoke and clouds, and requires higher temperatures to activate, and the time lapse between VIIRS and Landsat overpasses. Moreover, some high-intensity VIFDAHL and VIIRS I-band fire pixels also correspond to zero Landsat 8 fire pixel counts.

A source of potentially false VIFDAHL detections can be seen in areas with high-intensity fire and great amounts of smoke or clouds. Such an example is visible in the two westernmost fires in Figure 2.9a, as a halo of detections around the area that are certain to contain fire.

In the two smaller and less intensely burning (or more heavily suppressed) test scenes, Eagle and Willow, VIFDAHL overall yields between 30 and 50% more detections than the global VIIRS I-band dataset. For the two large-scale extended burn events of the 2015 Yukon Koyukuk and the 2016 Northern Koyukuk study area, we count approximately 90% more VIFDAHL than VIIRS I-band detections, some of them capturing residual fire as mapped by Landsat, some due to the halo-effect around smoke plumes.

2.6 Discussion and conclusions

VIFDAHL is easy to implement and computationally light-weight, as it uses simple thresholds on bands and band combinations, tuned for Alaskan boreal forest fires. The Alaska-specific approach with VIFDAHL was able to detect more low-intensity fire pixels than the global operational VIIRS I-band products. This is of interest for mapping areas that are most likely to pose a residual hazard and need to be monitored for any renewed need of fire suppression activity. While VIFDAHL appears to successfully avoid false detections from river banks or old fire scars, future work should look more closely into errors of commission, informed by experience gathered in operational use. Local VIFDAHL processing enables enhanced geolocation, which can be used for superior fire progression mapping (Figure 2.10). Another application would be stacking of repeated VIFDAHL detections in the same location to be used to estimate fire residence time, with potential links to fire severity. Further study is desirable with the objective to test the algorithm on the Canadian and Eurasian boreal forests.

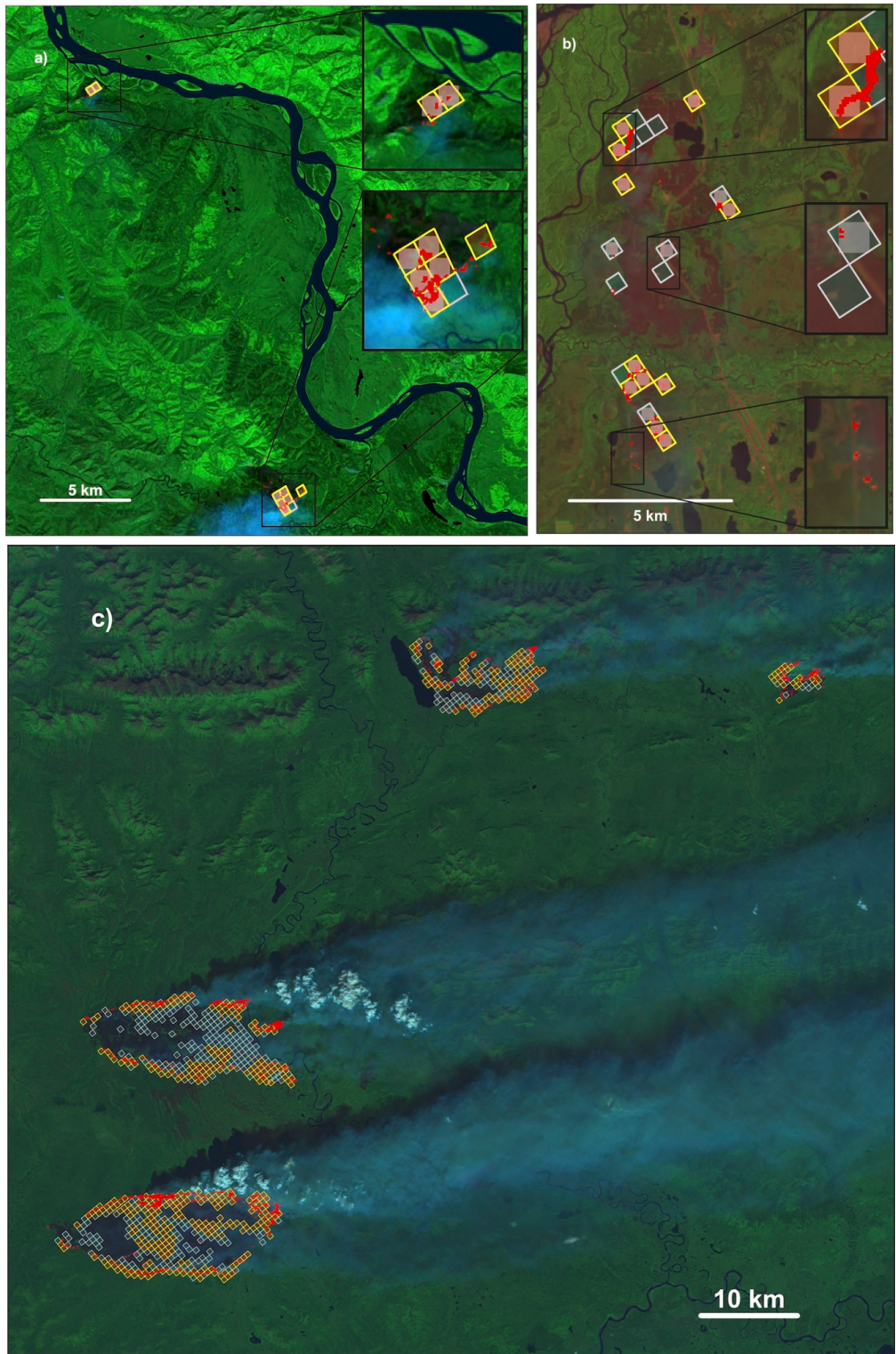


Figure 2.8: Overview of three study areas with VIFDAHL fire detections outlined in yellow (high-intensity active fire) and gray (low-intensity fire), on a background of near-simultaneous Landsat 7-5-3 false color RGB composite with Landsat fire detections overlaid in red. a) Eagle, 2016-05-27, central latitude 64.0°N, longitude 141.4°W. b) Willow, 2015-06-15, central latitude 61.8°N, longitude 151.1°W. c) Northern Koyukuk 2016-07-15, central latitude 66.9°N, longitude 153.1°W. In a) and b), VIFDAHL fire pixels that are also detected by the global VIIRS 375 m I-band product are shaded.

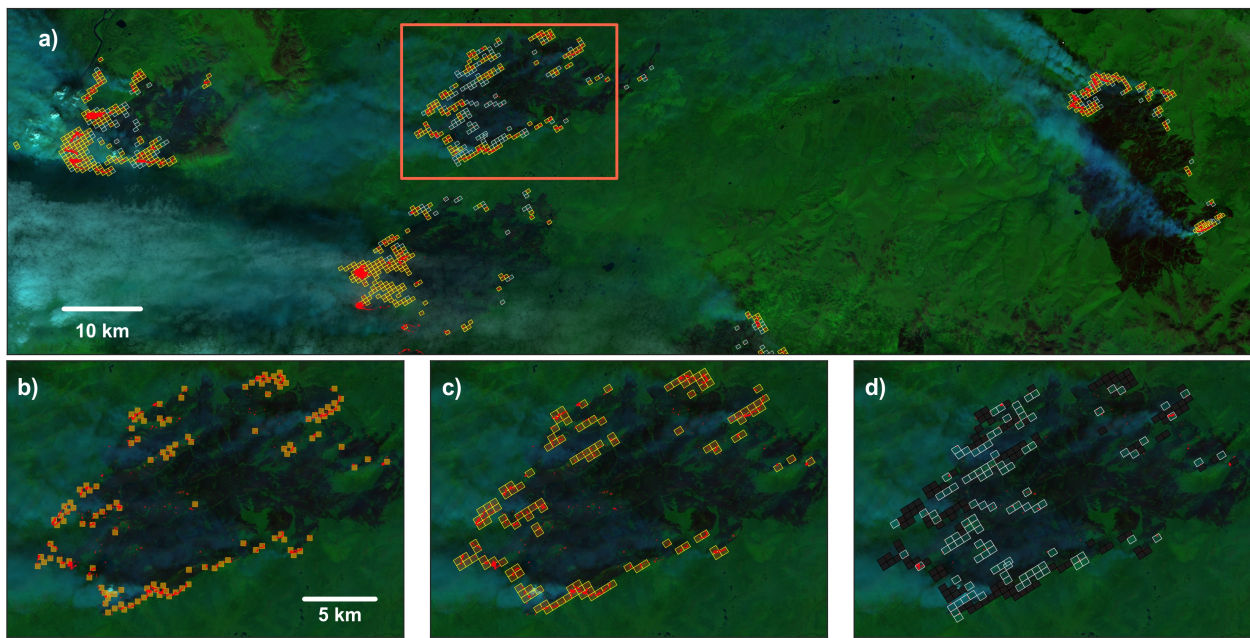


Figure 2.9: Overview and zoom into 2015 Yukon-Koyukuk study area, 2015-07-06, central latitude 65.9°N, longitude 152.7°W. Fire detection from a single VIIRS scene at 12:58 local time (AKDT) on top of a Landsat 8 bands 7-5-3 false color RGB composite, with Landsat fire detections marked in red. a) Entire study area, VIFDAHL detections, zoomed-in area outlined in red. b) Fire detections from the global VIIRS I-band product. c) VIFDAHL high-intensity detections. d) VIFDAHL low-intensity detections, with the locations of high intensity detections masked out in black for greater visual contrast

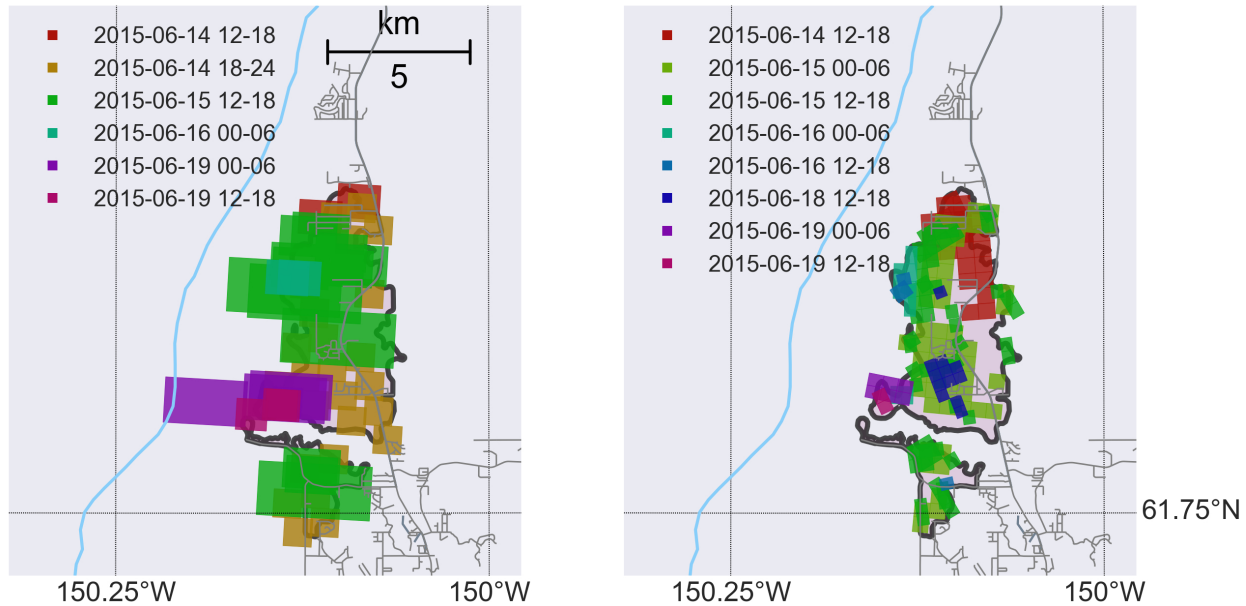


Figure 2.10: Willow study area, fire progression in 6-hour intervals. Roads, the Susitna River, and the official AICC fire perimeter are outlined. Left: MODIS active fires (pixel dimensions, but not orientation, are realistic from data). Right: VIFDAHL. A complete dataset of the global VIIRS I-band detections was not available for this 2015 fire.

2.7 Acknowledgements

This research was supported by NASA Headquarters under the NASA Earth and Space Science Fellowship Program – Grant NNX13AN90H. This research was supported in part by a UAF Center for Global Change Student Research Grant with funds from the Cooperative Institute for Alaska Research, and funding support from UAF’s College of Natural Science and Mathematics. C. Waigl is grateful to Alison York, Randi Jandt and Robert Ziel from the Alaska Fire Science Consortium as well as Evan Ellicott for many fruitful discussions, and to Wilfrid Schroeder for providing us with VIIRS I-band 375 m active fire data for the 2015 study areas. We thank the anonymous reviewers for their thoughtful critique, which improved the manuscript substantially.

We acknowledge the use of data and imagery from LANCE FIRMS operated by the NASA/GSFC/Earth Science Data and Information System (ESDIS) with funding provided by NASA/HQ. Landsat 8 data was available from the US Geological Survey.

References

- Andreae, M. O. and P. Merlet (2001). Emission of trace gases and aerosols from biomass burning. *Global Biogeochemical Cycles*, vol. 15, no. 4. 02027, pp. 955–966. DOI: 10.1029/2000GB001382.
- Cao, C., F. J. D. Luccia, X. Xiong, R. Wolfe, and F. Weng (2014). Early On-Orbit Performance of the Visible Infrared Imaging Radiometer Suite Onboard the Suomi National Polar-Orbiting Partnership (S-NPP) Satellite. *IEEE Transactions on Geoscience and Remote Sensing*, vol. 52, no. 2, pp. 1142–1156. DOI: 10.1109/TGRS.2013.2247768.
- Collins, M., R. Knutti, J. Arblaster, J.-L. Dufresne, T. Fichefet, P. Friedlingstein, X. Gao, W. J. Gutowski, T. Johns, G. Krinner, M. Shongwe, C. Tebaldi, A. J. Weaver, and M. Wehner (2013). Chapter 12 - Long-term climate change: Projections, commitments and irreversibility. In: *Climate Change 2013: The Physical Science Basis. IPCC Working Group I Contribution to AR5*. Ed. by IPCC. Cambridge: Cambridge University Press.
- Csiszar, I. A., J. T. Morisette, and L. Giglio (2006). Validation of active fire detection from moderate-resolution satellite sensors: the MODIS example in northern Eurasia. *IEEE Transactions on Geoscience and Remote Sensing*, vol. 44, no. 7, pp. 1757–1764. DOI: 10.1109/TGRS.2006.875941.

Csiszar, I., W. Schroeder, L. Giglio, E. Ellicott, K. P. Vadrevu, C. O. Justice, and B. Wind (2014). Active fires from the Suomi NPP Visible Infrared Imaging Radiometer Suite: Product status and first evaluation results. *Journal of Geophysical Research: Atmospheres*, vol. 119, no. 2, 2013JD020453. DOI: 10.1002/2013JD020453.

Dozier, J. (1981). A method for satellite identification of surface temperature fields of subpixel resolution. *Remote Sensing of Environment*, vol. 11, pp. 221–229. DOI: 10.1016/0034-4257(81)90021-3.

Genet, H., A. D. McGuire, K. Barrett, A. Breen, E. S. Euskirchen, J. F. Johnstone, E. S. Kasischke, A. M. Melvin, A. Bennett, M. C. Mack, T. S. Rupp, A. E. G. Schuur, M. R. Turetsky, and F. Yuan (2013). Modeling the effects of fire severity and climate warming on active layer thickness and soil carbon storage of black spruce forests across the landscape in interior Alaska. *Environmental Research Letters*, vol. 8, no. 4, p. 045016. DOI: 10.1088/1748-9326/8/4/045016.

Giglio, L., J. D. Kendall, and C. O. Justice (1999). Evaluation of global fire detection algorithms using simulated AVHRR infrared data. *International Journal of Remote Sensing*, vol. 20, no. 10, pp. 1947–1985. DOI: 10.1080/014311699212290.

Giglio, L., J. Descloitres, C. O. Justice, and Y. J. Kaufman (2003). An Enhanced Contextual Fire Detection Algorithm for MODIS. *Remote Sensing of Environment*, vol. 87, no. 2, pp. 273–282. DOI: 10.1016/S0034-4257(03)00184-6.

Giglio, L., W. Schroeder, and C. O. Justice (2016). The collection 6 MODIS active fire detection algorithm and fire products. *Remote Sensing of Environment*, vol. 178, pp. 31–41. DOI: 10.1016/j.rse.2016.02.054.

Grell, G., S. R. Freitas, M. Stuefer, and J. Fast (2011). Inclusion of biomass burning in WRF-Chem: impact of wildfires on weather forecasts. *Atmos. Chem. Phys.* Vol. 11, no. 11, pp. 5289–5303. DOI: 10.5194/acp-11-5289-2011.

Ichoku, C., R. Kahn, and M. Chin (2012). Satellite contributions to the quantitative characterization of biomass burning for climate modeling. *Atmospheric Research*, vol. 111, pp. 1–28. DOI: 10.1016/j.atmosres.2012.03.007.

Johnstone, J. F., T. N. Hollingsworth, F. S. Chapin, and M. C. Mack (2010). Changes in fire regime break the legacy lock on successional trajectories in Alaskan boreal forest. *Global Change Biology*, vol. 16, no. 4, pp. 1281–1295. DOI: 10.1111/j.1365-2486.2009.02051.x.

Justice, C., L. Giglio, S. Korontzi, J. Owens, J. Morisette, D. Roy, J. Descloitres, S. Alleaume, F. Petitcolin, and Y. Kaufman (2002). The MODIS fire products. *Remote Sensing of Environment*, vol. 83, no. 1-2, pp. 244–262. DOI: 10.1016/S0034-4257(02)00076-7.

Kasischke, E. S. and E. E. Hoy (2012). Controls on carbon consumption during Alaskan wildland fires. *Global Change Biology*, vol. 18, no. 2, pp. 685–699. DOI: 10.1111/j.1365-2486.2011.02573.x.

Kasischke, E. S., E. J. Hyer, P. C. Novelli, L. P. Bruhwiler, N. H. F. French, A. I. Sukhinin, J. H. Hewson, and B. J. Stocks (2005). Influences of boreal fire emissions on Northern Hemisphere atmospheric carbon and carbon monoxide. *Global Biogeochemical Cycles*, vol. 19, no. 1, GB1012. DOI: 10.1029/2004GB002300.

Kasischke, E. S. and M. R. Turetsky (2006). Recent changes in the fire regime across the North American boreal region—Spatial and temporal patterns of burning across Canada and Alaska. *Geophysical Research Letters*, vol. 33, no. 9, p. L09703. DOI: 10.1029/2006GL025677.

Kasischke, E. S., D. L. Verbyla, T. S. Rupp, A. D. McGuire, K. A. Murphy, R. Jandt, J. L. Barnes, E. E. Hoy, P. A. Duffy, M. Calef, and M. R. Turetsky (2010). Alaska's changing fire regime — implications for the vulnerability of its boreal forests. *Canadian Journal of Forest Research*, vol. 40, no. 7, pp. 1313–1324. DOI: 10.1139/X10-098.

Kasischke, E. S., D. Williams, and D. Barry (2002). Analysis of the patterns of large fires in the boreal forest region of Alaska. *Int. J. Wildland Fire*, vol. 11, no. 2, pp. 131–144. DOI: 10.1071/WF02023.

Kaufman, Y. J., C. O. Justice, L. P. Flynn, J. D. Kendall, E. M. Prins, L. Giglio, D. E. Ward, W. P. Menzel, and A. W. Setzer (1998). Potential global fire monitoring from EOS-MODIS. *Journal of Geophysical Research*, vol. 103, PP. 32, 215–32, 238. DOI: 10.1029/98JD01644.

Li, Z., Y. J. Kaufman, C. Ichoku, R. Fraser, A. Trishchenko, L. Giglio, J. Jin, and X. Yu (2000a). A review of AVHRR-based active fire detection algorithms: principles, limitations, and recommendations. *Canada Cent. Remote Sens.*, Ottawa, Canada.

Li, Z., S. Nadon, and J. Cihlar (2000b). Satellite-based detection of Canadian boreal forest fires: Development and application of the algorithm. *International Journal of Remote Sensing*, vol. 21, no. 16, pp. 3057–3069. DOI: 10.1080/01431160050144956.

Liang, C. K., S. Mills, B. I. Hauss, and S. D. Miller (2014). Improved VIIRS Day/Night Band Imagery With Near-Constant Contrast. *IEEE Transactions on Geoscience and Remote Sensing*, vol. 52, no. 11, pp. 6964–6971. DOI: 10.1109/TGRS.2014.2306132.

Matson, M. and J. Dozier (1981). Identification of subresolution high temperature sources using a thermal IR sensor. *Photogrammetric Engineering and Remote Sensing*, vol. 47, no. 9, pp. 1311–1318.

Menzel, W. P. and E. M. Prins (1996). Monitoring biomass burning with the new generation of geostationary satellites. In: *Biomass Burning and Global Change*. Ed. by J. S. Levine. Vol. 1. MIT Press, pp. 56–64.

Pfister, G., L. K. Emmons, P. G. Hess, R. Honrath, J. F. Lamarque, M. Val Martin, R. C. Owen, M. A. Avery, E. V. Browell, and J. S. Holloway (2006). Ozone production from the 2004 North American boreal fires. *J. Geophys. Res.*, vol. 111, D24S07.

Pfister, G., P. G. Hess, L. K. Emmons, J.-F. Lamarque, C. Wiedinmyer, D. P. Edwards, G. Pétron, J. C. Gille, and G. W. Sachse (2005). Quantifying CO emissions from the 2004 Alaskan wild-fires using MOPITT CO data. *Geophysical Research Letters*, vol. 32, no. 11. DOI: 10.1029/2005GL022995.

Pfister, G., P. G. Hess, L. K. Emmons, P. J. Rasch, and F. M. Vitt (2008). Impact of the summer 2004 Alaska fires on top of the atmosphere clear-sky radiation fluxes. *Journal of Geophysical Research: Atmospheres*, vol. 113, no. D2. DOI: 10.1029/2007JD008797.

Polivka, T. N., J. Wang, L. T. Ellison, E. J. Hyer, and C. M. Ichoku (2016). Improving Nocturnal Fire Detection With the VIIRS Day-Night Band. *IEEE Transactions on Geoscience and Remote Sensing*, vol. 54, no. 9. DOI: 0.1109/TGRS.2016.2566665.

Prins, E. M. and W. P. Menzel (1994). Trends in South American biomass burning detected with the GOES visible infrared spin scan radiometer atmospheric sounder from 1983 to 1991. *Journal of Geophysical Research: Atmospheres*, vol. 99, no. D8, pp. 16719–16735. DOI: 10.1029/94JD01208.

Prins, E. and C. Schmidt (2001). GOES burns bright. *Geospatial Solutions*, vol. 11, no. 7, p. 33.

Randerson, J. T., H. Liu, M. G. Flanner, S. D. Chambers, Y. Jin, P. G. Hess, G. Pfister, M. C. Mack, K. K. Treseder, L. R. Welp, F. S. Chapin, J. W. Harden, M. L. Goulden, E. Lyons, J. C. Neff, E. a. G. Schuur, and C. S. Zender (2006). The Impact of Boreal Forest Fire on Climate Warming. *Science*, vol. 314, no. 5802, pp. 1130–1132. DOI: 10.1126/science.1132075.

Roman, J. (2015). The Year in Wildfire. *NFPA Journal*, vol. 2015, no. Nov/Dec.

Schroeder, W., P. Oliva, L. Giglio, and I. A. Csiszar (2014). The New VIIRS 375 m active fire detection data product: Algorithm description and initial assessment. *Remote Sensing of Environment*, vol. 143, pp. 85–96. DOI: 10.1016/j.rse.2013.12.008.

Schroeder, W., P. Oliva, L. Giglio, B. Quayle, E. Lorenz, and F. Morelli (2015). Active fire detection using Landsat-8/OLI data. *Remote Sensing of Environment*. DOI: 10.1016/j.rse.2015.08.032.

Schroeder, W., E. Prins, L. Giglio, I. Csiszar, C. Schmidt, J. Morisette, and D. Morton (2008). Validation of GOES and MODIS active fire detection products using ASTER and ETM+ data. *Remote Sensing of Environment*, vol. 112, no. 5, pp. 2711–2726. DOI: 10.1016/j.rse.2008.01.005.

Soja, A. J., N. M. Tchekakova, N. H. F. French, M. D. Flannigan, H. H. Shugart, B. J. Stocks, A. I. Sukhinin, E. I. Parfenova, F. S. Chapin III, and P. W. Stackhouse Jr. (2007). Climate-induced boreal forest change: Predictions versus current observations. *Global and Planetary Change*, vol. 56, no. 3–4, pp. 274–296. DOI: 10.1016/j.gloplacha.2006.07.028.

Stevens, E. (2014). *Joint Polar Satellite Systems (JPSS) Common Data Format Control Book – External - Volume III - SDR/TDR formats*. 474-00001-03-B0123. GSFC.

Chapter 3

FIRE DETECTION AND TEMPERATURE RETRIEVAL USING EO-1 HYPERION DATA OVER SELECTED ALASKAN BOREAL FOREST FIRES¹

Abstract

Infrared imaging spectrometers are used to map and characterize wildland fire based on their sensitivity to fire-emitted thermal radiation and ability to resolve spectral emission or absorption features. There is a general paucity of research on the use of space-borne imaging spectroscopy to study active fires in the North American boreal forest. We used hyperspectral data acquired by the Hyperion sensor on the EO-1 satellite over three wildfires in Alaska's boreal forest to evaluate three fire detection methods: A metric to detect an emission feature from potassium emitted by biomass burning; a continuum-interpolated band ratio (CIBR) that measures the depth of a carbon dioxide absorption line at 2010 nm; and the Hyperspectral Fire Detection Index (HFDI), which is a normalized difference index based on spectral radiance in the short-wave infrared range. We found that a modified version of the HFDI produces a well-defined map of the active fire areas. The CO₂ CIBR, though affected by sensor noise and smoke, contributes a slight improvement to the fire detection performance when combined with HFDI-type indices. In contrast, detecting a fire signal from potassium emission was not reliably possible in a practically useful way. We furthermore retrieved fire temperatures by modeling the at-sensor radiance as a linear mixture of two emitted and two reflected spectral radiance endmembers. High-temperature fire areas (the high-intensity fire front, modeled at 800-900 K) and low-temperature combustion (residual fire at 500-600 K), were mapped. High-temperature burning areas as small as half a percent of a Hyperion pixel (approx. 5 m²) were detectable. These techniques are of potential interest for fire characterization in the boreal areas of the circumpolar North using current and future satellite-borne imaging spectrometers.

¹Waigl, C. F., Prakash, A., Stuefer, M., Verbyla, D., & Dennison, P. (2017). Manuscript submitted to Remote Sensing of Environment

3.1 Introduction

Satellite-based infrared remote sensing has been in use since the 1980s as a cost-effective way to detect and investigate wildfires (e.g. Flannigan and Haar 1986; Ichoku et al. 2012; Prakash et al. 2011; Robinson 1991). Multispectral sensors, which typically offer a small number of carefully placed spectral bands, are widely used. For the detection of radiation emitted by active fire, the mid- and thermal infrared (MIR and TIR) regions of the electromagnetic spectrum are of particular interest (Briess et al. 2003; Giglio et al. 2003, 2016; Kaufman et al. 1998; Schroeder et al. 2014) as the fire-emitted radiance in the MIR range (approximately 4 μm) far exceeds background levels even if fire only occupies a small portion of a pixel. Other techniques employ shortwave infrared (SWIR) data from sensors with a spatial resolution of approximately 30 m and suitable sensitivity and saturation behavior (Giglio et al. 2008; Schroeder et al. 2015).

In contrast, in imaging spectroscopy (also called hyperspectral remote sensing), data is acquired in a large number of contiguous spectral bands that typically span the visible and near-infrared (VNIR) as well as the shortwave infrared regions of the electromagnetic spectrum. Given that an imaging spectrometer produces a radiance or reflectance spectrum at every pixel of the image, a frequently used approach consists in unmixing these spectra using spectral libraries of relevant land cover classes (Roberts et al. 1998). Imaging spectroscopy has been applied to wildfire analysis with respect to pre- and post-fire research topics such as vegetation classification (Dalmonte et al. 2013; Dennison et al. 2006; Goodenough et al. 2003), fire danger (Roberts et al. 2003), forest canopy fuel characteristics (Jia et al. 2006) and fire severity (Lewis et al. 2011). Nearly all of these works use airborne hyperspectral imagery. Studies of high-temperature events that are relevant to satellite-based hyperspectral remote sensing include applications to volcanology (Abrams et al. 2013; Wright et al. 2010), fire detection (Amici et al. 2011; Dennison 2006; Dennison and Roberts 2009) and fire characterization via fire temperature and fractional pixel area retrieval (Dennison et al. 2006; Dennison and Matheson 2011). These studies rely on the spectral emission and absorption features, sensitivity, and large number of data points produced by the hyperspectral instrument instead of MIR or TIR bands, which are generally not available.

Active fire in the boreal forest is currently not well-studied using imaging spectroscopy despite the fact that wildland fire is an important factor in the boreal forest eco-region (Chapin et al. 2000). For Alaska, where a majority of the boreal areas of the United States of America is located, wildfires consume an average of 7500 km² annually (Kasischke et al. 2010). The average annual burned area has been estimated to increase by 2.4 %/yr (Calef et al. 2015, for 1943-2012) to 3.1 %/yr (Giglio et al. 2013, for all of boreal North America, 1995-2011).

The Hyperion sensor on the National Aeronautic and Space Administration's (NASA's) EO-1 (Earth Observation 1) satellite platform (Middleton et al. 2013; Pearlman et al. 2003; Ungar et al. 2003) offers an opportunity to fill this gap and develop methodologies that will be more useful as future imaging spectrometers become available. Currently, planned missions are NASA's Hyperspectral Infrared Imager (HyspIRI) (Abrams et al. 2013; Lee et al. 2015; Middleton et al. 2010), the German Environmental Mapping and Analysis (EnMAP) instrument (Kaufmann et al. 2006), and the Spaceborne Hyperspectral Applicative Land and Ocean Mission (SHALOM) (Ben Dor et al. 2014; Feingersh and Ben Dor 2015), a collaboration of the space agencies of Israel and Italy. All of these missions will offer a spatial resolution comparable to Hyperion, a similar range of spectral channels, and reduced noise. HyspIRI will also include a multispectral TIR instrument (Realmuto et al. 2015; Roberts et al. 2012).

We explore the application of satellite-based imaging spectroscopy to the study of the properties of active fires in Alaska's boreal forest. In the following sections, we introduce our three study areas, which are located in interior Alaska, and provide an overview of the available Hyperion data. We then describe three known fire detection methods that have the potential to be applicable to our study scenes: the Hyperspectral Fire Detection Index (HFDI), the detection of a potassium (K) emission feature, and the carbon dioxide continuum-interpolated band ratio (CIBR), which relies on the measurement of an absorption feature to differentiate between emitted and reflected radiation. We also describe how sub-pixel active fire temperatures and fractional areas are retrieved using a linear combination of simulated atmospherically corrected emission spectra and reflected background spectra. The description of methods is followed by a summary of results and their discussion. We conclude by evaluating our findings with a view on how these

methods could be applicable to future satellite-borne hyperspectral sensors and which design features might be particularly beneficial for active boreal forest fire remote sensing.

3.2 Study Areas

We selected three study areas (Figure 3.1) based on the availability of EO-1 Hyperion data over large Alaskan wildfires. We searched the catalog of available scenes in the United States Geological Survey (USGS) data archive based on fire location and time data from the Alaska Large Fires Database (ALFD) (Kasischke et al. 2002) and subsequently selected all scenes that clearly showed several clusters of contiguous pixels with active combustion that were not obscured by smoke or clouds. The selected scenes represent the 2004 Boundary fire, the 2004 Crazy fire, and the 2009 Wood River fire.

With a burned area of 2150 km², the 2004 Boundary fire north of Fairbanks, Alaska, was the largest wildfire of the most extreme Alaska fire season on record: During the summer of 2004, a total of 27 000 km² burned in approximately 700 separate fire events (AICC 2004). The Boundary fire, discovered on June 13, 2004, was a highly destructive lightning-caused event which greatly impacted air quality (Grell et al. 2011) and aerial traffic across interior Alaska (Wendler et al. 2010), and was sufficiently severe to affect the post-fire succession of tree species in the boreal forest (Johnstone et al. 2010).

The 2004 Crazy fire was a smaller fire event (final burned area: 210 km²) whose active period overlapped with the Boundary fire. It started from a lightning-caused ignition on July 4, 2004, approximately 75 km north-east of the Boundary fire.

The Wood River fire of 2009 also had air quality impact on Fairbanks. It burned in an area reserved for military use south of the town. Its final size is given as approximately 500 km² (AICC 2009), but its burn perimeter includes considerable unburned areas. (The official designation of this fire event is "Wood River 1", but we omit the number for the sake of readability.)

The land cover in all three study areas is dominated by highly flammable black spruce forest. Stand density is much lower for the Wood River fire, which burned through a mix of forest and

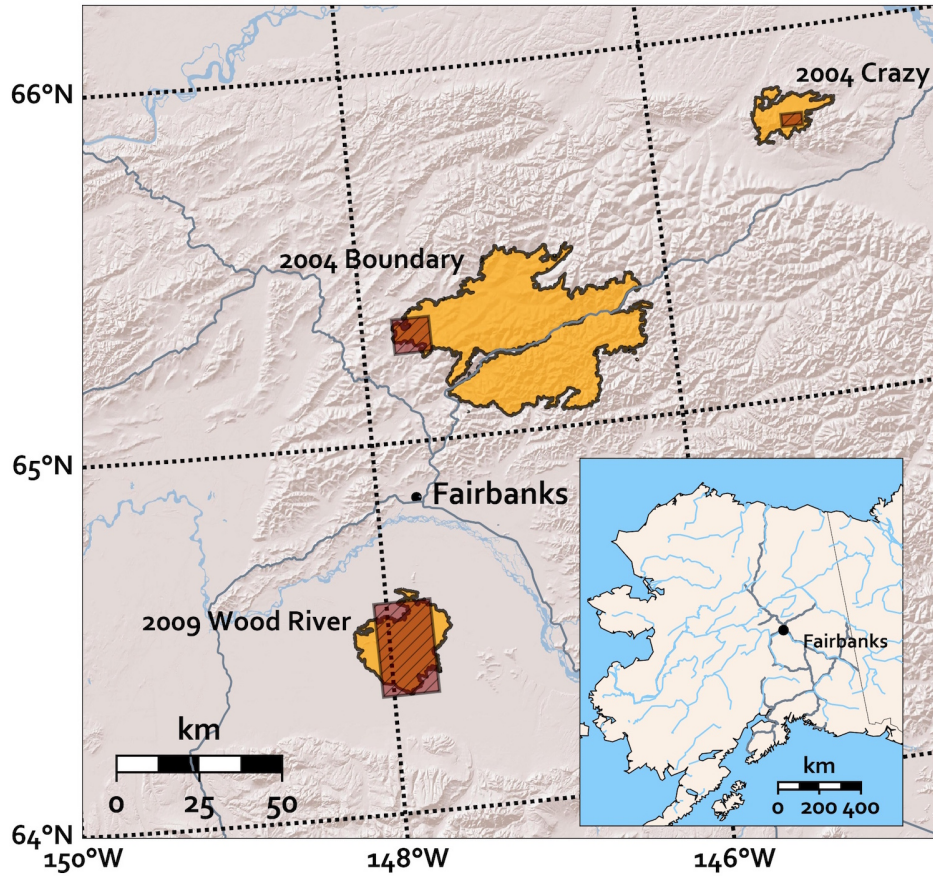


Figure 3.1: Map of study areas and corresponding final fire perimeters within interior Alaska. The rectangular areas represent the three Hyperion study scenes. Rivers and major roads are marked.

open brush land. The landscape is wetter and flatter than for the Boundary or the Crazy fire, located in hilly areas at higher elevations (500 to 1000 m above mean sea level). The Boundary fire also affected mixed conifer and hardwood stands.

3.3 Data

3.3.1 *The Hyperion sensor on EO-1*

The Hyperion sensor is a pushbroom instrument with a 7.7 km wide imaging swath and a ground-sampling distance (GSD) of 30 m (Ungar et al. 2003). It is composed of two separate spectrometers: A VNIR instrument (400 - 1000 nm) and a SWIR instrument (1000 - 2500 nm), both with a spectral bandwidth of 10 nm (Figure 3.2) (Barry 2001). In total, it has 242 spectral bands, with VNIR and SWIR channels overlapping around 1000 nm. Due to the moderate signal-to-

noise ratio (SNR), which deteriorates in the SWIR region compared to the VNIR, only 198 unique calibrated usable channels – 50 VNIR and 148 SWIR – are processed in the Level 1B product (Pearlman et al. 2003). The longest-wavelength calibrated channel is band 224 (central wavelength 2395.5 nm).

Originally conceived as a 1-year technology demonstration, the EO-1 mission went through several extensions (Middleton et al. 2013) after its initial operational phase (11/2000 – 2/2002) was completed. Orbital parameters were not preserved throughout the extensions. The data for the 2004 Boundary and Crazy fires were acquired during the initial extended phase that ended in late 2005, during which the EO-1 spacecraft was maintained in a 705 km orbit. In 2006, EO-1 was lowered until it reached an orbital height of 690 km, at which point, in 2007, the mission was revived (*ibid.*). The 2009 Wood River study scene was acquired during the phase that followed. 2016 was EO-1’s last operational year.

Hyperion data is distributed as 12-bit unsigned integer raster data, which is radiometrically and terrain-corrected (Simon 2006).

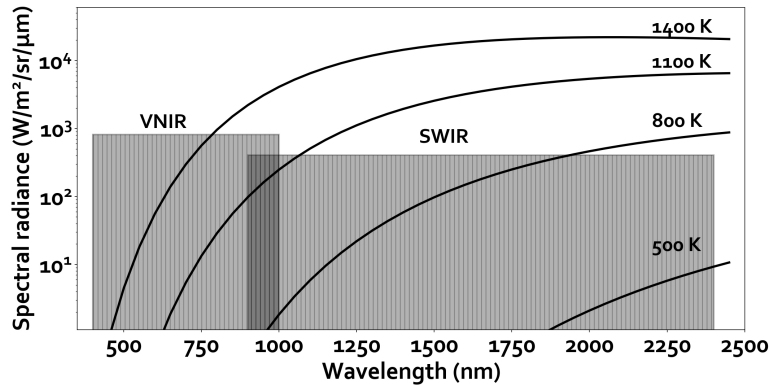


Figure 3.2: Wavelength range of the VNIR and SWIR instruments of the Hyperion sensor. Some blackbody spectra are superimposed for comparison.

3.3.2 Hyperion scenes

For all three study scenes, the Hyperion scene reference, scene start time stamp, sensor look angle and latitude/longitude of the center of the used subset are summarized in Table 3.1. All overpasses took place within 20 min of 1 pm Alaska Daylight Time, on a descending node.

The Hyperion scene available for the Boundary fire was acquired on July 19, 2004 and captures a small portion of the fire close to the western boundary of the final fire perimeter (Figure 3.1). Between the peak of the fire event on July 17 and the overpass of the EO-1 satellite two days later, traces of precipitation halted its progress. The Hyperion imagery for the Crazy fire was acquired on July 10, 2004, when it was highly active.

The third study scene was acquired over the Wood River fire on August 2, 2009, during a high-intensity phase of the fire event. Unfortunately, the Hyperion swath missed the most active portions of the fire front and only captured a number of relatively small fire pixel clusters, which are also spread over a larger area than in the 2004 Crazy and Boundary fire scenes. The 2009 data also appears to contain more noise and more pronounced pushbroom stripes than the earlier scenes. Therefore, we do not present any detailed maps of fire detection or temperature retrieval over this scene. However, the Wood River data was included in the evaluation of fire detection indices.

Table 3.1: EO-1 Hyperion scenes and central latitude/longitude (WGS 84) of the subsets used

Fire name	Hyperion scene	Scene starttime (UTC)	Sensor look angle	Latitude	Longitude
Crazy	EO1H0680132004192	2004-07-10 21:07:57	10.358°	65.74979°	-145.0569°
Boundary	EO1H0690142004201	2004-07-19 21:02:11	-2.4442°	65.28703°	-147.7966°
Wood River	EO1H0690142009214	2009-08-02 20:40:37	-16.446°	64.44595°	-147.8978°

3.4 Methods

Our Hyperion processing steps are summarized in Figure 3.3. After subsetting the swaths to the study areas, the digital numbers were converted to spectral radiance by dividing them by the scaling factors of 40 for the VNIR bands and 80 for the SWIR bands, specified in the scene metadata (*ibid.*). The theoretical upper limits for measurable radiance are $819.2 \text{ W}/(\text{m}^2 \mu\text{m sr})$ (VNIR) and $409.6 \text{ W}/(\text{m}^2 \mu\text{m sr})$ (SWIR), respectively.

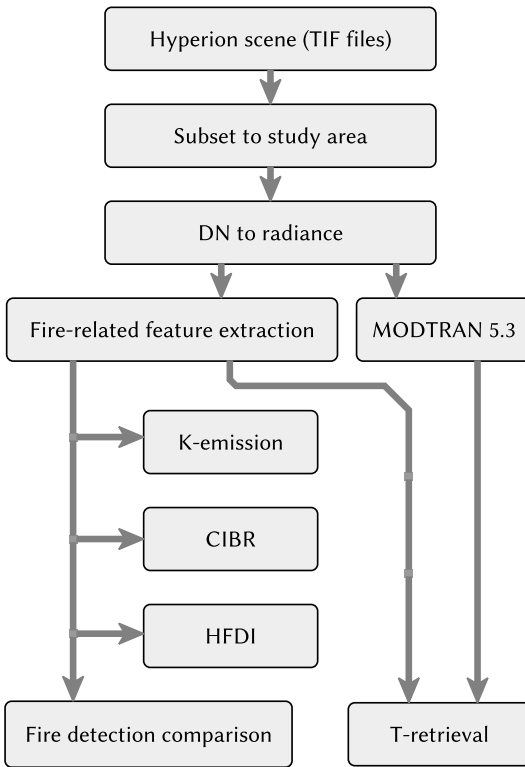


Figure 3.3: Hyperion processing flow

3.4.1 *Fire-related feature extraction*

The evaluation and comparison of fire detection methods requires labeled fire and non-fire pixel data, which we generated by applying supervised classification to the study scenes. We used a false natural-color RGB image of each scene (bands 150-50-23, with central wavelengths of 1648.9 nm, 854.18 nm, and 579.45 nm) to manually sample 20 pixels from each of the following four classes: fire, fresh fire scar, vegetation (forest or forest/shrubland), smoke/cloud. We carefully selected areas that were as pure as possible, avoiding mixed land cover classes and data anomalies such as saturation effects. By “fire” we mean pixels that contain actively burning areas. The Crazy fire imagery contained enough of both smoke and cloud that 20 pixels from each class were sampled, whereas the Wood River imagery is virtually smoke/cloud free, so the class was not sampled.

We further constrained the study areas more narrowly to the fire-adjacent region using a mask which we constructed by first applying a spectral radiance threshold of $5 \text{ W}/(\text{m}^2 \mu\text{m sr})$ in band 220 (2355.21 nm). The threshold was based on an inspection of non-fire pixels, whose spectral radiance was less than this value). For the Crazy fire scene, we additionally excluded cloud pixels, which are highly reflective in the SWIR. Then we drew a convex shape around the set of all pixels exceeding the threshold, leaving a 20 pixel buffer. The resulting mask ensures that only data located in the vicinity of active fire was processed. The pixels contained in these irregularly shaped final subsets were classified with a Random Forest classifier (Breiman 2001), a supervised classification method that has been successfully applied to Hyperion data (e.g. Ham et al. 2005), with the manually labeled sample pixels serving as training data. To assess the stability of the classifier and confirm the adequacy of using 20 training samples per class, we carried out a K-fold cross-validation ($K = 10$) (Friedman et al. 2001).

The pixels in the “fire” class served as a data source for labeled fire pixels to evaluate fire detection methods, while the “vegetation” and “fire scar” classes represented the non-fire background. The “fire” class also was used as the input for fire temperature retrieval.

3.4.2 Fire detection

Fire detection in imaging spectroscopy data can use a number of different approaches. One is to rely on the same methods as fire detection in multi-spectral imagery: to identify thermal anomalies based on the electromagnetic radiation emitted by a burning source. If we represent the fire as a blackbody held at a constant temperature, the emitted spectral radiance is given by Planck’s law:

$$L_\lambda = \frac{2hc^2}{\lambda^5 \left(e^{\frac{hc}{\lambda kT}} - 1 \right)} \quad (3.1)$$

with T the absolute temperature, λ the wavelength, h Planck’s constant, k Boltzmann’s constant and c the speed of light. With increasing temperature, the maximum of the emission curve

moves towards shorter wavelengths, in a relation that is inversely proportional to the temperature (Wien's law):

$$\lambda_{\max} \propto T^{-1} \quad (3.2)$$

The spectrum of a pixel that contains fire activity will therefore show a higher overall radiance of the longer SWIR wavelengths compared to what its spectrum would look like without fire.

Alternatively, hyperspectral remote sensing can make use of features that are caused by potassium emission and carbon dioxide absorption (Amici et al. 2011; Dennison 2006; Dennison and Roberts 2009; Vodacek et al. 2002).

We tested and, where necessary, adapted three known fire detection indices for hyperspectral data, each time proceeding in an identical fashion: Between all test scenes, we randomly sampled 250 fire pixels (from the “fire” class) and 250 background pixels (from the “vegetation” or “fire scar” class), calculated each index for all sample pixels and statistically analyzed the result for its ability to differentiate fire and background. We calculated all fire detection indices based on at-sensor spectral radiances that were uncorrected for atmospheric effects as a first approximation. During our analysis we also tested combinations of two or all three indices to maximize detection accuracy and minimize false detections (errors of commission).

3.4.2.1 *Potassium (K) emission*

This method uses the potassium (K) emission lines at 767 and 770 nm (Vodacek et al. 2002) characteristic for biomass burning. In Hyperion data, both emission lines fall within band 42 with a central wavelength of 772.78 nm. Its spectral radiance would be elevated in the presence of fire-stimulated potassium emissions (Cahill et al. 2008), but the neighboring band at 780 nm would not be.

Dennison and Roberts (2009) define a K-emission index as the ratio $L_{770\text{nm}}/L_{780\text{nm}}$ and use it with data from the Airborne Visible / Infrared Imaging Spectrometer (AVIRIS), while Amici et al.

(2011) examine high spectral resolution as well as simulated and real Hyperion data using a metric called the Advanced K-Band Difference (AKBD). In Hyperion data the AKBD metric translates to the band difference $L_{770\text{nm}} - L_{780\text{nm}}$.

Values for the K-emission ratio are expected to be <1 , and AKBD values <0 . This is because the 770 nm band is also the location of multiple oxygen absorption lines which overlap with the K-emission features (Vodacek et al. 2002) and, averaged over the width of the 770 nm Hyperion band, lead to a distinctly visible absorption feature (Amici et al. 2011).

3.4.2.2 Carbon dioxide continuum-interpolated band ratio (CO₂ CIBR)

The second fire detection method makes use of the CO₂ absorption feature at 2010 nm. It takes advantage of the principle that radiation emitted by a fire only has to travel through the atmosphere once to arrive at a satellite-borne sensor, whereas reflected sunlight traverses the atmosphere twice. Emitted radiation at this spectral location therefore undergoes less absorption than reflected radiation. Therefore, for fire pixels, the CO₂ absorption line should appear less pronounced than for background pixels. Mathematically, the depth of the absorption line is captured by defining an index called the carbon dioxide continuum-interpolated band ratio (CO₂ CIBR) (Dennison 2006; Dennison and Roberts 2009), used successfully for fire detection with Hyperion and AVIRIS data. As the absorption feature is located on an upslope section of the radiance spectrum, the two shoulders of the feature are not typically at the same value. This situation is reflected via interpolation factors used in the formula provided by Dennison (2006):

$$\text{CIBR} = \frac{L_{2010\text{nm}}}{0.666 L_{1990\text{nm}} + 0.334 L_{2040\text{nm}}} \quad (3.3)$$

3.4.2.3 Hyperspectral fire detection index (HFDI)

The third approach uses a normalized difference index calculated from the spectral radiance values in two suitable SWIR bands, which enables the detection of pixels that contain thermal

anomalies. (Dennison and Roberts 2009). Dennison and Roberts (*ibid.*) found the following HFDI performing the best on AVIRIS data for daytime detection of the Simi Fire in California:

$$\text{HFDI} = \frac{L_{2430\text{ nm}} - L_{2060\text{ nm}}}{L_{2430\text{ nm}} + L_{2060\text{ nm}}} \quad (3.4)$$

A threshold for detection is determined at a value that optimally separates fire pixels from non-fire pixels; it is typically close to zero, or has a small negative value (*ibid.*).

The value of 2430 nm exceeds the longest wavelength available in Hyperion's L1B calibrated spectral radiance product. We therefore determined a suitable combination of spectral bands to substitute the lower and upper wavelengths used in (3.4) and used this modified HFDI for further fire detection performance analysis.

3.4.3 MODTRAN for atmospheric correction

Active fire temperature retrieval requires atmospherically corrected sources of emitted infrared radiation. We used MODTRAN 5.3 (Berk et al. 2006) to generate transmittance profiles for each study scene across the wavelength region between 350 and 2500 nm. The MODTRAN input was based on user-specified model atmosphere from radiosonde data acquired at noon on the day of the respective overpass at Fairbanks International Airport (PAFA station) distributed by the University of Wyoming Atmospheric Sciences Department (<http://weather.uwyo.edu/upperair/sounding.html>). Due to the presence of active fire, and therefore smoke, in the study scene, we selected the predefined option "rural extinction, visibility 5 km". Additional MODTRAN input parameters are summarized in Table 3.2.

The transmittance profiles were then used to generate a set of simulated atmospherically corrected blackbody radiance spectra to serve as temperature endmembers in a linear model.

Table 3.2: Configuration used with MODTRAN 5.3

Parameter	Comment
MODEL = 7	User-specified model atmosphere from radiosonde data (PAFA station, noon)
ITYPE = 2	Vertical or slant path between two altitudes
IHAZE = 2	RURAL extinction, default VIS = 5 km
IEMSCT = 0	Spectral transmittance mode only
CO2MX = 390.0	CO ₂ mixing ratio
H1 / GNDALT	Determined from altitude of center of subset
H2	Determined from highest level available in radiosonde profile
ANGLE	Determined from sensor look angle
V1 = 350	Initial wavelength (nm)
V2 = 2500	Final wavelength (nm)
DV = 1	Wavelength step (nm)

3.4.4 Temperature retrieval

The spectrum measured at the pixel that is the site of active fire can be modeled as a linear mixture of emitted and reflected components (Dennison et al. 2006). We represented the measured at-sensor spectral radiance $L_{\lambda, m}$ as the sum of signals that originate from a number n of fractional areas each of which burns at a constant temperature T_i , plus uniform background components:

$$L_{\lambda, m} = \sum_{i=1}^n p_{i, \text{fire}} L_{\lambda}(T_i) + \sum_{j=1}^m p_{j, \text{background}} L_{j, \text{reflected}} \quad (3.5)$$

$L_{\lambda}(T_i)$ is the atmospherically corrected spectral radiance of the temperature component T_i , $L_{j, \text{reflected}}$ is the j th background component, and the p_i and p_j are the corresponding fractional pixel areas, which have to add up to 1. Atmospheric scattering was taken into account via the IHAZE parameter in the MODTRAN transmittance calculation (Section 3.4.3, Table 3.2). Otherwise, path radiance was neglected (following e.g. Dennison and Matheson 2011). This approach is similar to the two-component sub-pixel temperature and fractional area retrieval method developed by Dozier (1981) using mid- and thermal infrared data; the uncertainties in retrieved fire temperature and fractional area increase substantially when the fractional fire area becomes very small (Giglio and Kendall 2001).

In order to select suitable background components $L_{j,\text{reflected}}$ we considered that the reflected contribution dominates in the VNIR spectral range. To reduce the influence of the reflected radiation components and scattering by smoke at shorter wavelengths we limited the analysis to all wavelengths $\lambda > 1400$ nm (100 calibrated Hyperion channels). In the vicinity of active fires, we are likely to find two physically distinct background landcover types: vegetation and fire scar. After inspecting SWIR spectra from the “vegetation” and “fire scar” classes, we found them to be quite distinct, at least in the shorter wavelength part of the SWIR range (between 1400 and 1800 nm) and therefore opted for two separate background contributions ($m = 2$). The $p_{j,\text{background}}$ become the fractional areas p_{veg} and p_{scar} .

For the emitted components $L_\lambda(T_i)$ we used Planck blackbody spectra which we atmospherically corrected using the MODTRAN 5.3 transmittance profiles calculated for each acquisition date. For each study case, a catalog of these temperature endmembers was generated covering the temperature range between 40 K and 1200 K in steps of 10 K.

To determine the parameters T_i and p_i we used least-squares curve fitting for the set of all pixels in the “fire” class. The best-fitting n temperature endmembers are retained as modeled temperature components. Regarding the choice of n , Dennison et al. (2006) used a single temperature component, but at a much higher spatial resolution (AVIRIS GSD of 5 m instead of 30 m for Hyperion) which is more likely to be adequately described by a single fire temperature. A different example comes from an application to lava temperatures using Hyperion data (Abrams et al. 2013; Wright et al. 2010), where an n of 2 or 3 yielded a satisfactory fit. We started with a single temperature component followed by an increase of n to 2, checking whether the RMS error improved.

In our model, $m = 2$ and $n = 2$ means fitting five parameters to 100 Hyperion SWIR data points (T_1 , $p_{1,\text{fire}}$, T_2 , $p_{2,\text{fire}}$ and p_{veg} , with p_{scar} determined via the constraint that the sum of all fractional areas must be 1). Even though it would appear that there is no risk of overfitting, there are strong arguments against further increasing n : The spectral radiance values of a Hyperion SWIR spectrum are not arbitrary, but correlated with each other. They are also affected by sensor noise, and we made a number of simplifying assumptions (that the fire targets are blackbody radi-

ators, that path radiance is minimal and can be neglected, that the composition of the background is uniform). For the area footprint (900 m^2) of a Hyperion pixel, model output with two temperature components would appear to reasonably describe a physical reality, but this becomes less true when the number of temperature endmembers increases.

3.5 Results

3.5.1 *Fire detection and comparative analysis*

Fire, fire scar, vegetation and smoke/cloud areas (Figure 3.4) were delineated for each study area using a Random Forest classifier. We set the number of decision tree estimators in the classifier to 100 and verified the stability of the classification by repeat runs, observing that pixel counts in all classes remained roughly equal. Furthermore, a 10-fold cross-validation, each time with a different 60/40 split of the labeled input data into training and test sets, yielded accuracy and F1 (macro) scores (the harmonic average of true positive rate [or recall] and the positive predictive value [or precision]) of 0.97 ± 0.11 (for both). This good result also confirms that selecting 20 labeled training samples in each class was sufficient. The final classifications have 1019 pixels in the “fire” class for the Crazy fire test site, 662 for the Boundary fire scene, and 197 for the Wood River scene. Across the classified scenes, we randomly sampled 500 pixels for use as a labeled test set to evaluate fire detection indices (200 each from the Crazy and Boundary fire scenes and 100 from the Wood River scene, given the smaller number of fire pixels in this scene). Half the samples were drawn from the “fire” class and half from “fire scar” or “vegetation”, which together represent the “background” class for the purpose of fire detection.

Spectra from the “fire” class that are free from anomalies or saturation effects can be distinguished from background pixels by observing the spectral radiance values in the SWIR range: Unlike in pure background pixels, whose spectrum would continue to fall off, a contribution from emitted SWIR radiation is apparent (Figure 3.5 a). At higher fire intensities the longer-wavelength SWIR part of the spectra saturates, reaching spectral radiances close to the theoretical maximum of $409.6 \text{ W}/(\text{m}^2 \mu\text{m} \text{sr})$ (Figure 3.5 b) However, we observe that not all saturation effects manifest as a range of radiance values pinned to the theoretical maximum: in some pixels, and even

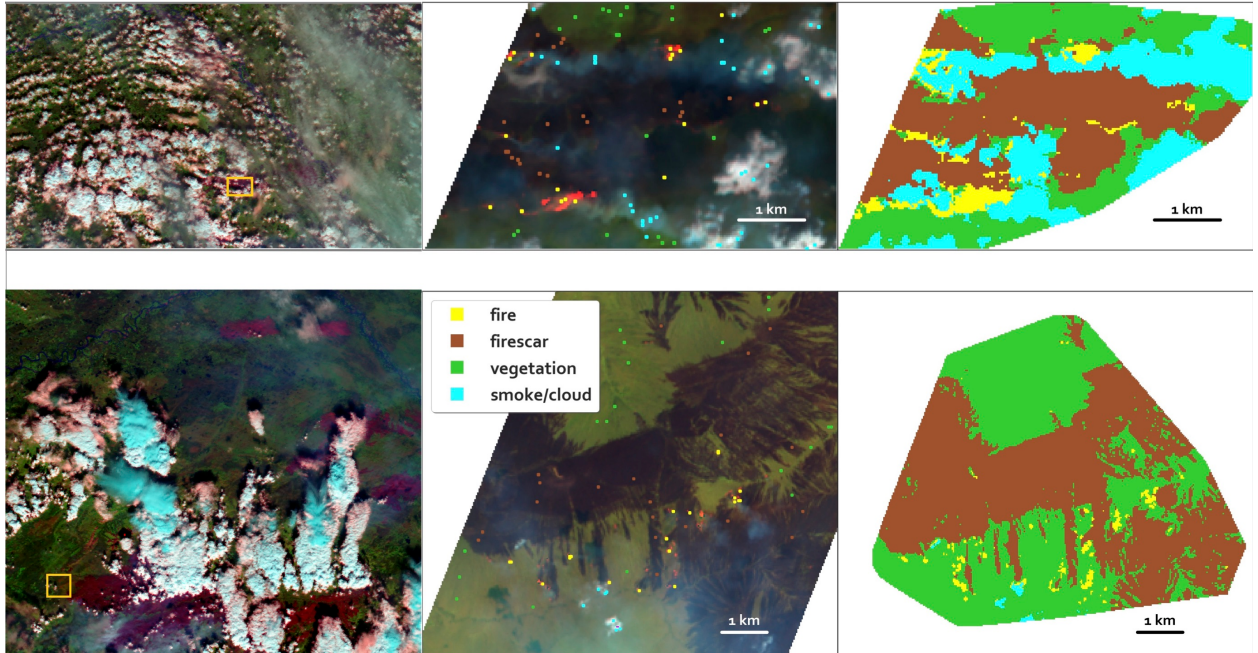


Figure 3.4: Crazy fire (top) and Boundary fire (bottom). Left: Overview plot from the Moderate-resolution Imaging Spectroradiometer (MODIS) on the Terra satellite, acquired the same day as the Hyperion scene. RGB composite using bands 7-2-1. The extents of the Hyperion scenes are marked by yellow rectangles. Middle: Hyperion RGB composite using bands 150-50-23 in RGB (1648.9 nm, 854.18 nm, and 579.45 nm), with manual samples marked. Right: classification output. Cloud and smoke classes are combined. The irregular shape of the classified subsets (right) reflects the final subset masks, which delineate the fire-adjacent zones using a simple SWIR radiance threshold.

at radiance levels below those of the most intense fires, individual bands exhibit spikes (which may or may not extend all the way to the saturation maximum) even when neighboring bands do not. This may be due to potential differences in the lag time between saturation and becoming operational again for individual Hyperion detector elements.

The CO₂ absorption feature used for calculating the CO₂ CIBR index is markedly present at approximately the expected location (Figure 3.5 c). After data inspection, we used bands 183 at 1981.86 nm and 188 at 2032.35 nm for the shoulders of the absorption line, and band 185 at 2002.06 nm, where the minimum of the absorption feature was consistently located, for its center. In contrast, no K-emission feature in band 42 is discernible with the naked eye (Figure 3.5 d).

We then evaluated all three indices over the labeled test set of 500 sample pixels (Figure 3.6). For the HFDI, band 224, with a central wavelength of 2395.5 nm, is the longest-wavelength cal-

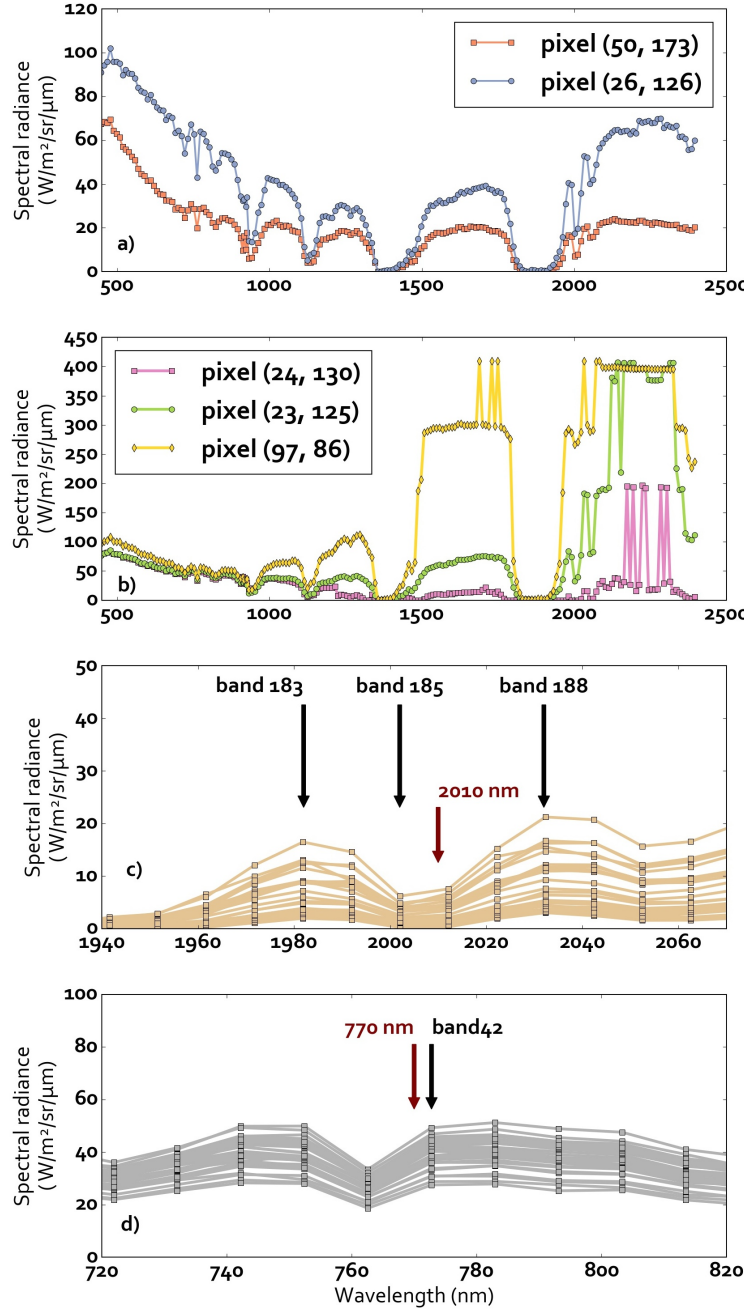


Figure 3.5: Examples of fire pixel radiance spectra. a) and b) represent a selection of fire pixel spectra (taken from the Crazy fire study area at the indicated pixel locations). c) and d) show the theoretical absorption or emission feature location and relevant bands used for fire detection with the the CO₂ CIBR and K-emission methods, respectively.

ibrated band, and we found the top of the Hyperion band range, beyond approximately band 220, to be extremely noisy. As for the shorter wavelength used to construct the published HFDI (Dennison and Roberts 2009), 2060 nm is closest to Hyperion's band 191. To consider a range of

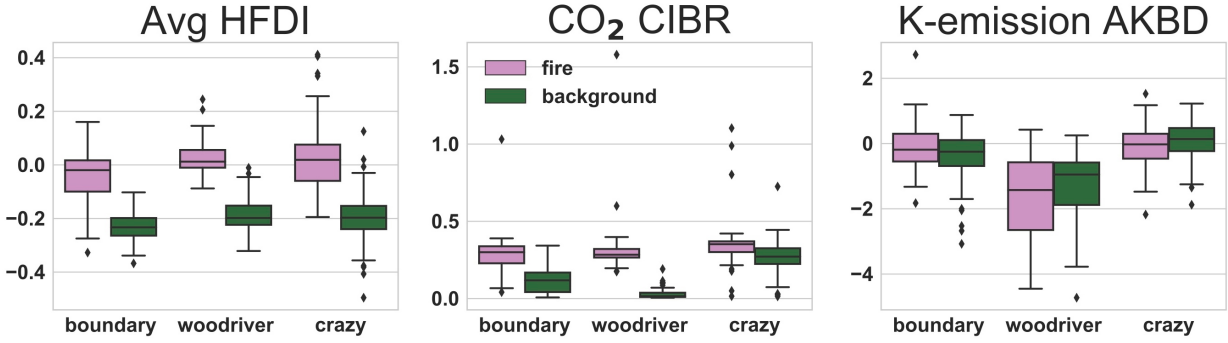


Figure 3.6: Comparison (box plots) of the distributions of average HFDI, carbon dioxide CIBR and K-emission band difference index across fire and background pixels for each fire event. The whiskers extend to the highest and lowest datum still within 1.5 times the inter-quartile range. Data points beyond this range are plotted as outliers.

candidate bands for a Hyperion-based HFDI we selected all combinations of shorter-wavelength and longer-wavelength bands that can be generated from any of the bands 190, 191, 192, 193, 194, 195, and 196 as the shorter-wavelength band and any of the bands 217, 218 and 219 as the longer-wavelength band. We thereby avoided the bands in the middle of the spectral radiance “plateau”, which are often affected by anomalies and saturation effects (Figure 3.5).

It was apparent that for an HFDI calculated with band 190 as the shorter-wavelength band, both the variance of HFDI values and the separation of fire and background HFDI values was worst, likely due to sensor noise in band 190. To further quantify the available choices for a Hyperion-specific HFDI, we modeled the distribution of HFDI values in both the fire and background class for each combination as normal distributions and calculated their overlap (which represents the sum of all errors of commission and of omission), the optimal cut-off value to separate fire from background, as well as the positive predictive value and the F1 score (Table 3.3), which takes into account both errors of commission and of omission.

Several potentially “best” combinations obtain very similar results in positive predictive value and F1 score and there is no clear cut-off other than removing band 190 from consideration. We therefore discarded the three combinations of band 190 with bands 217 to 219 and averaged the remaining 18 HFDI combinations. Averaging the indices calculated from multiple bands has the advantage of reducing the influence on single-band noise on the resulting mean index value.

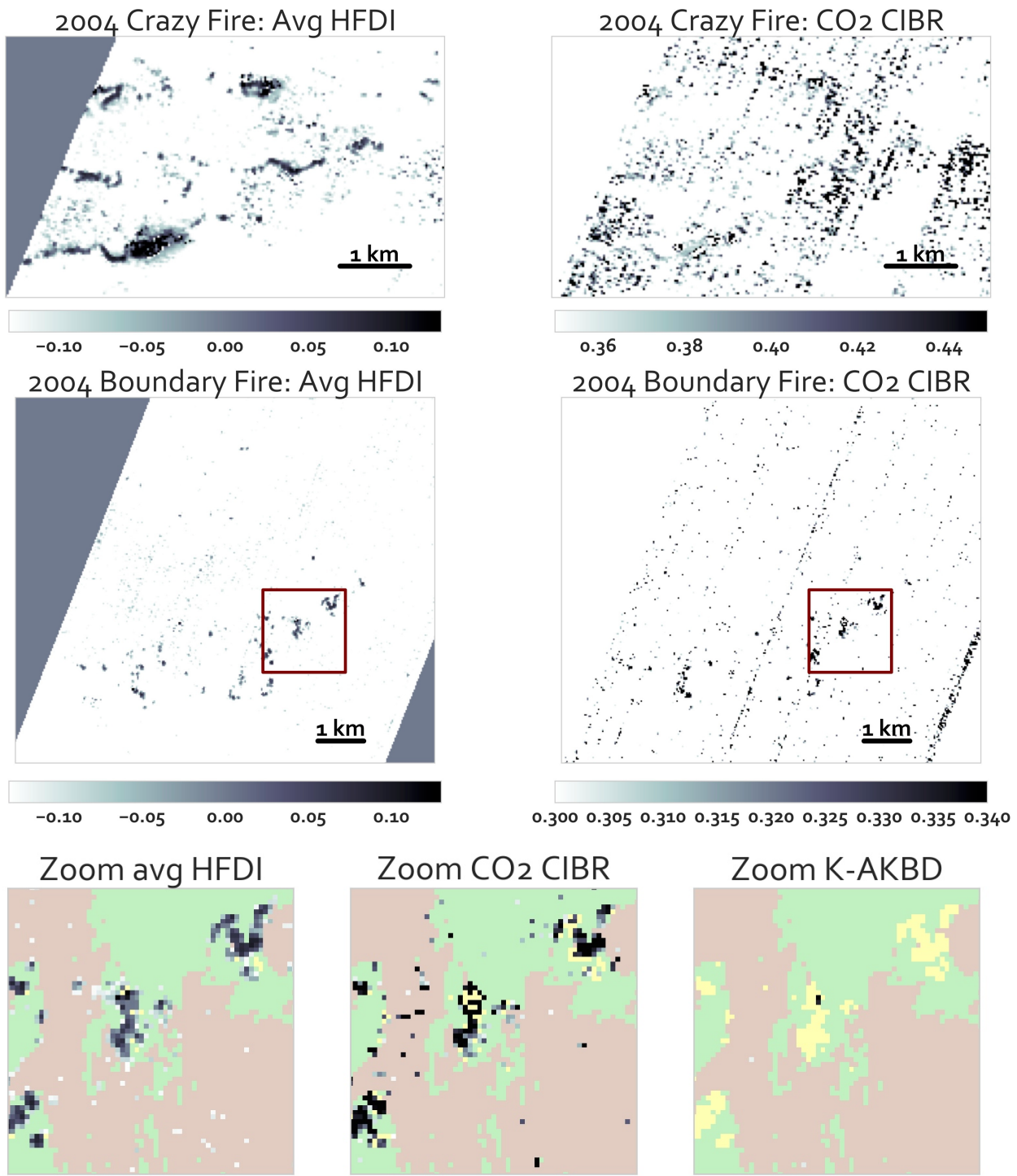


Figure 3.7: Values of average HFDI and CO₂ CIBR for the Crazy and Boundary fire study areas. For the Boundary fire, the sub-region, marked by a rectangle, is enlarged (bottom row). For the enlarged region, we added the K-emission (AKBD) metric (extreme outlying values only). The colors correspond to the supervised classification, identical to Figure 3.4: fire (yellow), fire scar (brown) and vegetation (green). The gray (including white) values are the fire detection metrics on the same color ramp as the zoomed-out plots.

Table 3.3: HFDI band combinations evaluated for 500 labeled sample pixels (fire and background). The cut-off column refers to the optimal HFDI value to separate fire from non-fire. The overlap column represents the modeled overlap between the fire and non-fire distribution. The true detection rate is the true positive rate calculated for fire detection. PPV represents the positive predictive value for fire detection.

Bands	Central λ (nm)	Cut-off	Overlap	True detection rate	PPV	F1 score
196, 217	2113.04, 2324.91	-0.172	0.138	0.868	0.879	0.873
196, 218	2113.04, 2335.01	-0.192	0.146	0.864	0.882	0.873
195, 218	2102.94, 2335.01	-0.192	0.143	0.86	0.885	0.872
195, 217	2102.94, 2324.91	-0.152	0.149	0.84	0.901	0.87
196, 216	2113.04, 2314.81	-0.172	0.134	0.84	0.897	0.868
195, 216	2102.94, 2314.81	-0.172	0.144	0.836	0.889	0.862
194, 218	2092.84, 2335.01	-0.172	0.169	0.836	0.878	0.857
193, 218	2082.75, 2335.01	-0.152	0.177	0.84	0.868	0.854
193, 217	2082.75, 2324.91	-0.111	0.185	0.812	0.894	0.851
194, 217	2092.84, 2324.91	-0.131	0.161	0.816	0.887	0.85
194, 216	2092.84, 2314.81	-0.152	0.149	0.824	0.873	0.848
192, 216	2072.65, 2314.81	-0.051	0.175	0.812	0.886	0.848
193, 216	2082.75, 2314.81	-0.131	0.172	0.828	0.855	0.841
192, 218	2072.65, 2335.01	-0.071	0.18	0.82	0.861	0.84
192, 217	2072.65, 2324.91	-0.051	0.184	0.828	0.848	0.838
191, 218	2062.55, 2335.01	0.03	0.215	0.82	0.82	0.82
191, 216	2062.55, 2314.81	0.051	0.21	0.804	0.824	0.814
191, 217	2062.55, 2324.91	0.071	0.222	0.792	0.822	0.807
190, 218	2052.45, 2335.01	0.071	0.313	0.792	0.692	0.739
190, 216	2052.45, 2314.81	0.111	0.318	0.728	0.728	0.728
190, 217	2052.45, 2324.91	0.111	0.334	0.764	0.687	0.723

For this “average HFDI” (Figure 3.6), we found an optimal cut-off value to separate fire from background of -0.13, based on our data.

The CO₂ CIBR index is also capable of separating fire from background (Figure 3.6), albeit with notable differences between the three study areas (Figures 3.6 and 3.7). This index also produces some extreme outliers. Between all 500 samples, the optimal CO₂ CIBR value to separate fire from background was determined to be 0.21. As for the K-emission index, we found no statistical ability to distinguish fire from background (Figure 3.6). For two of the test scenes, the median index value is even (slightly) greater for the background pixels than for the fire pixels.

We tested whether fire detection could be improved by retaining all 18 HFDI combinations separately and adding the CO₂ CIBR as well, effectively calculating a data vector of length 19

for each pixel. To evaluate the potential improvement over the averaged HFDI, we constructed a new Random Forest classifier using the 500 labeled test pixels. After executing a 10-fold cross-validation (60/40 split of the labeled samples in training and test sets) we determined a classification accuracy of 0.85 (std: 0.02) for the mean HFDI and 0.87 (std: 0.02) for the combined multi-HFDI-plus-CIBR classifier.

3.5.2 Temperature retrieval

The need for two separate background components was confirmed as we found that SWIR spectra from the “fire scar” and “vegetation” classes were quite distinct (Figure 3.8a). The distinction between the two classes was most pronounced in the shorter-wavelength SWIR region between 1400 and 1800 nm, while they vary much less in the longer-wavelength SWIR region above 1900 nm. For each study case, we used the sample-averages of the “fire scar” and “vegetation” spectra as reflective endmembers.

With a single emitted component (corresponding to three independently fitted parameters p , T , and p_{veg}), we found that the fit of fire spectra was often unsatisfactory. We therefore added a second temperature component (five independently fitted parameters, p_1 , T_1 , p_2 , T_2 , and p_{veg}), which greatly improved the result. There was no justification for adding a third temperature component.

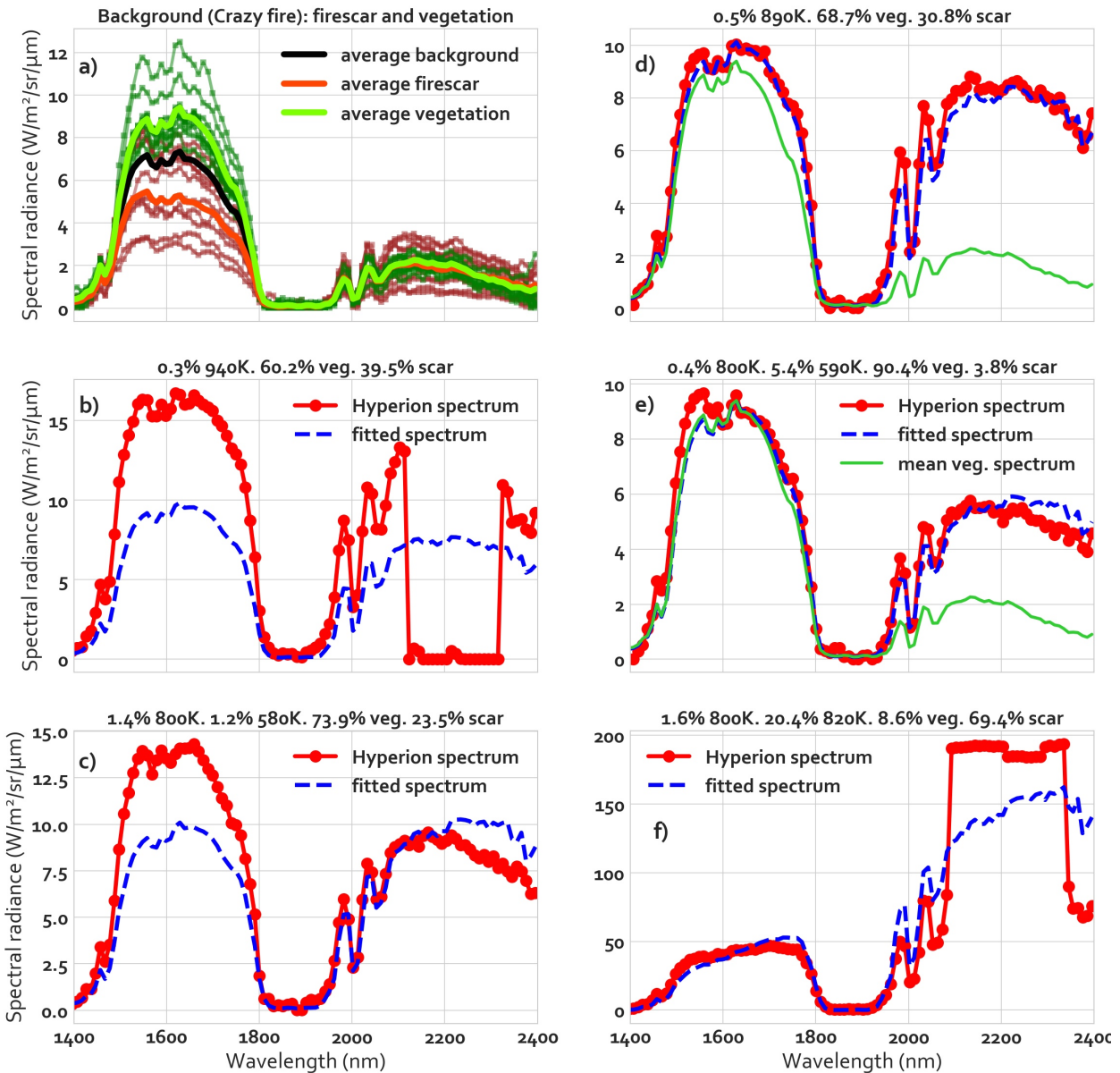


Figure 3.8: Example spectra for T-retrieval. a) sample spectra from vegetation and fire scar classes (green and brown), and average spectra (green, red-orange, black). b) to f) Examples of temperature and fractional area fit to individual Hyperion radiance spectra. b) and c) illustrate unsatisfactory fit in pixels with large reflective radiance contribution in the lower SWIR region, or due to data anomalies. d) to f) illustrate very good fit. In d), e), even small fractional active fire areas are clearly distinct from pure vegetation spectra (green curve).

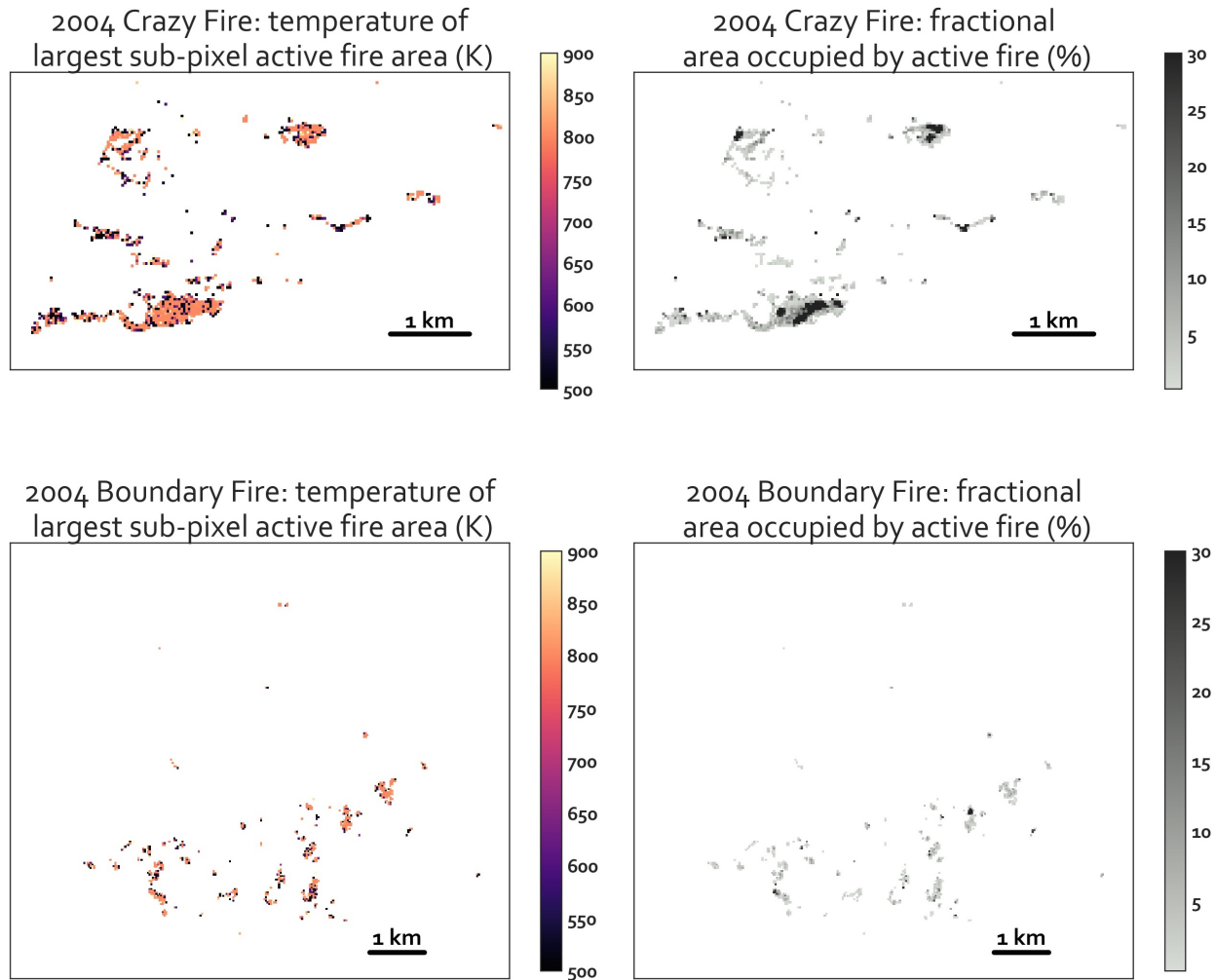


Figure 3.9: Burning areas of the Crazy and Boundary study sites: Temperature of the largest active fire fraction T_1 (left) and total fractional fire area $p_1 + p_2$ (right). The fire temperature map shows the most intense flaming combustion in bright colors and the pixels in which the largest fire contribution is from smoldering or other low-intensity fire in darker colors. The most intense fire front is represented by high fire temperatures on the left and high fractional areas (dark pixels) on the right. In contrast, low fire temperatures (dark tones) on the left combined with large fractional areas (dark tones) on the right would correspond to a pixel that is for a large part affected by low-intensity combustion.

Typically, the fit to the measured spectra was excellent, such as in cases of pixels that are dominated by a mix of vegetation and fire scar plus either a very small fraction of relatively high-temperature fire (Figure 3.8d) or a slightly larger fraction of low-temperature fire (Figure 3.8e). Both these cases yield spectra that are essentially identical to pure background spectra in the shorter-wavelength part of the SWIR range, but deviate strongly in the longer-wavelength part. Some pixels with saturation effects are also reasonably well fitted (Figure 3.8f). In contrast, Figures 3.8b) and c) illustrate cases of relatively poor curve fit.

The retrieved temperature T_1 that corresponds to the larger active fire fraction and the total fractional fire area ($p_1 + p_2$) are plotted in Figure 3.9 for the Crazy and Boundary fire scenes. (We labeled the indices so that $p_1 > p_2$.)

3.6 Discussion

The performance of the three fire detection methods varies. Using K-emission, we were unable to tell fire and background pixels apart. Amici et al. (2011), on the other hand, approach the method from a different angle and only look at pixels for which AKBD values are exceptionally high, which indeed, in one of the two sample scenes they examine (the 2007 Witch fire in California), enables them to detect a fire signal using Hyperion data. Following their approach, we also found an area within the the 2004 Boundary fire scene for which outliers in the AKBD metric correspond to locations of intense combustion (Figure 3.7, bottom row). However, the same does not apply to the 2004 Crazy or the 2009 Wood River fire, even though the Crazy fire scene contains the most intense fire across our three study sites.

Thus, even though we were able to reproduce the detection of a weak K-emission signal in one of three study cases, we cannot consider the K-emission method useful for fire detection in the Alaska boreal forest. It should be pointed out that the 2007 Witch fire was a very high intensity event that burned in chaparral shrubland near Escondido, California. This eco-region has a fire regime very different from that of a boreal forest fire in a black spruce dominated ecosystem. In the Alaska case, a large percentage of the biomass consumption comes from the sub-surface layers of organic matter (Randerson et al. 2006) rather than from quick-burning surface fuels.

Furthermore, the absence of a K-emission signal even in the highest-intensity fire pixels of the Crazy fire may be related to the presence of large amounts of smoke in the scene. The active fire pixels of the 2009 Wood River fire were generally of low intensity, and a signal was not expected in this case. The main factors limiting the usefulness of K-emission with Hyperion are the much coarser spatial resolution of the satellite-borne sensor, which leads to a lowered sensitivity, and the strong sensor noise.

The carbon dioxide CIBR, which is based on an absorption feature, shows a clear statistical difference between fire and background pixels. Fire areas are discernible in a map of CO₂ CIBR values (Figure 3.7), but on a background of substantial noise. The Crazy fire test scene is particularly hard to map using the CO₂ CIBR, and the plot suggests that areas containing smoke or clouds, and to a lesser degree burn scars, introduce a large number of false detections. The optimal CO₂ CIBR threshold to distinguish fire from background appears to vary from scene to scene. Zooming into known fire areas, we see that high CIBR values follow the outline of the fire front (Figure 3.7, bottom row). The CO₂ CIBR quantifies the proportion of emitted radiation in the measured spectral radiance value at a specific wavelength. To make it more useful standing on its own the image would have to be de-striped and cloud-masked, which would come at the cost of losing further detail in the signal.

An average of 18 HFDI band combination produces crisp fire maps with HFDI values that appear to correlate with fire intensities. Averaging helps reduce the noise inherent in Hyperion data. The Hyperion-specific averaged HFDI provided a reasonably stable detection threshold that did not vary greatly between three fire events in the Alaska boreal forest. A downside of band-averaging is that it effectively lowers the spectral resolution of the imaging spectrometry data, from 10 nm to 60 nm (six shorter-wavelength bands) and 30 nm (three longer-wavelength bands). Even a 60 nm bandwidth is still relatively small compared to common satellite-borne multispectral sensors (for example Landsat 8 OLI SWIR band 7: 187 nm). Essentially, opting for a band-averaged index rather than single-band index reflects a necessary choice to avoid noisy or sub-optimally located Hyperion bands. In general, a normalized-difference based index is likely to be less susceptible to spectral resolution than an index that relies on an individual spectral feature. Opportunities for better fire detection using the HFDI-type normalized detection indices

will require improved performance of future sensors in the 2400 - 2500 nm range, beyond the end of Hyperion's range of calibrated channels, and reduced noise across the SWIR range, rather than a finer spectral resolution.

Dennison and Roberts (2009) indicate that an HFDI-type index does not increase monotonically with fire intensity for very hot fires ($T > 1400$ K), for which the emitted radiance at the shorter wavelength (approximately 2060 nm) will begin to exceed the radiance at the longer wavelength (approximately 2400 nm). For Hyperion, however, we do not find non-saturated pixels with usable data in this temperature range and can therefore assume that for our data, higher HFDI values correspond to higher fire intensities. The HFDI values found in the Crazy and Boundary fire data appear to be consistent with this principle (Figure 3.7): The HFDI reveals rich fire intensity patterns, which are an improvement over the result we obtained from supervised classification. A mixed approach that relies on all 18 HFDI band combinations plus the CO₂ CIBR was able to achieve a small improvement in classification accuracy, but at the cost of losing a single meaningful scalar index.

The linear spectral mixture analysis yields an overall excellent result for retrieving active fire temperatures based on two constant background components (vegetation and fire scar) and two active fire components whose temperatures were allowed to vary freely from pixel to pixel. Measured spectra with very small fractional areas (< 1%, that is, 5 - 9 m²) of high-temperature active fire on a mixed vegetation and fire scar background were fitted extremely well (Figure 3.8d). The same is true for pixels that contain a somewhat larger fractional area of low-temperature fire (Figure 3.8e). Even pixels with 20 % to 25 % (approximately 200 m²) of high-intensity active fire (Figure 3.8e) were modeled quite well even though the Hyperion sensor saturates in the SWIR region at such signal intensities. Typical temperatures for high-temperature fire components ranged from 800 K to 900 K. This value, which is not very high for wildfire, is limited by the saturation behavior of the Hyperion sensor: Beyond 900 K, the spectral radiance contribution in the longer-wavelength part of the SWIR region (>1900 nm) saturates the sensor; a meaningful temperature retrieval becomes impossible. The low temperatures of fire components were typically at values of 500 K to 600 K, which falls within the region of smoldering combustion of organic forest soil matter (Rein et al. 2008). The model therefore provides a pixel-by-pixel characteriza-

tion of fire behavior properties. We were able to map hotter and cooler fire areas, and regions in which active fire occupies a larger or smaller fractional pixel area (Figure 3.9).

There are two limitations for temperature retrieval in our study: First, pixels with severe SWIR data anomalies such as drop-outs and some saturation behavior cannot be fitted well (Figure 3.8b). Second, some fire pixels are dominated by a reflected radiance component that exceeds the typical vegetation-type background at the shorter-wavelength end (1400 - 1800 nm). These pixels contain a source of reflected solar radiation that was not adequately captured by our choice of an averaged vegetation background spectrum (Figure 3.8c). Due to the small size of the study area (and the narrowness of the Hyperion swath) we considered it sufficient to use per-scene constant vegetation and fire scar endmembers; the unsatisfactory fit of some pixels highlights the limitation of this assumption. We could overcome it by applying a contextual selection and averaging mechanism to determine pixel-by-pixel background contributions. Such background contributions should continue to further distinguish between fire scar and vegetation and would provide improved information on the fractional areas of a pixel that are unburned versus already-burned.

3.7 Conclusions, recommendations, and future work

We have demonstrated the usefulness of a Hyperion-type hyperspectral sensor to detect, map, and characterize active fire in Alaska's boreal forest as well as the land cover changes introduced by fire (fire scar and unburned vegetation). We detected both high-intensity flaming fire and low-temperature combustion likely associated with smoldering fire. Sensors like Hyperion have great potential to further identify classes of fuel type (Dennison et al. 2006) and condition, as well as the properties of both fresh and older burn scars. One area for future research includes fire severity, which, in the Alaska boreal forest, is associated with the degree to which the sub-surface layers of organic matter are consumed (Lentile et al. 2006). Such work requires a field component.

Future instruments are already being designed with an emphasis on enhanced SNR, as is the case for HyspIRI at 500:1 (2200 nm) (Lee et al. 2015) and EnMAP at >150:1 (SWIR) (Kaufmann

et al. 2006) compared to Hyperion’s SNR of 38:1 at 2125 nm (Pearlman et al. 2003). Areas of active combustion represent a larger percentage of total pixel area as spatial resolution is increased, so finer spatial resolutions could make the detection of weak spectral features, such as the K-emission line, more likely. Such a requirement, though, is in conflict with a shorter repeat interval, which would be highly desirable for monitoring relatively rapid landscape processes such as a change in pre-fire fuel conditions or fire effects. Similarly, improved saturation behavior needs to be considered as a trade-off with sensor sensitivity (Realmuto et al. 2015). Design goals such as a short recovery lag before saturated sensor elements are operational again or a well-documented signature of sensor saturation are likely to be preferable to a high saturation threshold on a sensor that is incapable of picking up weak heat signals. We hope that new and enhanced satellite-borne imaging spectrometers will become available in the future as they would expand and improve our ability to understand wildfire.

3.8 Acknowledgements

This research was supported by NASA Headquarters under the NASA Earth and Space Science Fellowship Program – Grant NNX13AN90H. This publication is the result in part of research sponsored by the Cooperative Institute for Alaska Research with funds from the National Oceanic and Atmospheric Administration under cooperative agreement NA13OAR4320056 with the University of Alaska. The authors acknowledge support from Alaska EPSCoR NSF award #OIA-1208927 and the state of Alaska. We are thankful for the support of the Alaska Climate Research Center.

The authors thank the United States Geological Survey for Hyperion data, the University of Wyoming Atmospheric Sciences Department for the radiosonde data and BLM/Alaska Fire Service for fire perimeter data used in Figure 3.1.

The open-source scientific Python libraries scikit-learn (Pedregosa et al. 2011) and scipy (Jones et al. 2001–) were used for Random Forest classification and curve fitting.

References

- Abrams, M., D. Pieri, V. Realmuto, and R. Wright (2013). Using EO-1 Hyperion Data as HyspIRI Preparatory Data Sets for Volcanology Applied to Mt Etna, Italy. *IEEE Journal of Selected Topics in Applied Earth Observations and Remote Sensing*, vol. 6, no. 2, pp. 375–385. DOI: 10.1109/JSTARS.2012.2224095.
- AICC (2004). *Alaska Fire Season 2004*. Alaska Interagency Coordination Center.
- AICC (2009). *Alaska Fire Season 2009: Wildland Fire Summary and Statistics Annual Report*. Alaska Interagency Coordination Center.
- Amici, S., M. J. Wooster, and A. Piscini (2011). Multi-resolution spectral analysis of wildfire potassium emission signatures using laboratory, airborne and spaceborne remote sensing. *Remote Sensing of Environment*, vol. 115, no. 8, pp. 1811–1823. DOI: 10.1016/j.rse.2011.02.022.
- Barry, P. (2001). *EO-1/Hyperion science data user's guide, Level 1_B*. Redondo Beach, CA: TRW Space, Defense & Information Systems.
- Ben Dor, E., A. Kafri, and G. Varacalli (2014). SHALOM: An Italian-Israeli hyperspectral orbital mission—Update. In: *International Geoscience and Remote Sensing Symposium, Quebec, Canada, July 13–18, 2014*.
- Berk, A., G. P. Anderson, P. K. Acharya, L. S. Bernstein, L. Muratov, J. Lee, M. Fox, S. M. Adler-Golden, J. H. Chetwynd, M. L. Hoke, R. B. Lockwood, J. A. Gardner, T. W. Cooley, C. C. Borel, P. E. Lewis, and E. P. Shettle (2006). MODTRAN5: 2006 update. In: *Algorithms and Technologies for Multispectral, Hyperspectral, and Ultraspectral Imagery XII*. Vol. 6233. International Society for Optics and Photonics, 62331F. DOI: 10.1117/12.665077.
- Breiman, L. (2001). Random Forests. *Machine Learning*, vol. 45, no. 1, pp. 5–32. DOI: 10.1023/A:1010933404324.
- Briess, K., H. Jahn, E. Lorenz, D. Oertel, W. Skrbek, and B. Zhukov (2003). Fire recognition potential of the bi-spectral Infrared Detection (BIRD) satellite. *International Journal of Remote Sensing*, vol. 24, no. 4, pp. 865–872. DOI: 10.1080/01431160210154010.
- Cahill, C. F., T. A. Cahill, and K. D. Perry (2008). The size- and time-resolved composition of aerosols from a sub-Arctic boreal forest prescribed burn. *Atmospheric Environment*, vol. 42, no. 32, pp. 7553–7559. DOI: 10.1016/j.atmosenv.2008.04.034.

Calef, M. P., A. Varvak, A. D. McGuire, F. S. Chapin, and K. B. Reinhold (2015). Recent Changes in Annual Area Burned in Interior Alaska: The Impact of Fire Management. *Earth Interactions*, vol. 19, no. 5, pp. 1–17. DOI: 10.1175/EI-D-14-0025.1.

Chapin, F. S., A. D. McGuire, J. Randerson, R. Pielke, D. Baldocchi, S. E. Hobbie, N. Roulet, W. Eugster, E. Kasischke, E. B. Rastetter, S. A. Zimov, and S. W. Running (2000). Arctic and boreal ecosystems of western North America as components of the climate system. *Global Change Biology*, vol. 6, pp. 211–223. DOI: 10.1046/j.1365-2486.2000.06022.x.

Dalponte, M., H. O. Ørka, T. Gobakken, D. Gianelle, and E. Næsset (2013). Tree Species Classification in Boreal Forests With Hyperspectral Data. *IEEE Transactions on Geoscience and Remote Sensing*, vol. 51, no. 5, pp. 2632–2645. DOI: 10.1109/TGRS.2012.2216272.

Dennison, P. E. (2006). Fire detection in imaging spectrometer data using atmospheric carbon dioxide absorption. *International Journal of Remote Sensing*, vol. 27, no. 14, pp. 3049–3055. DOI: 10.1080/01431160600660871.

Dennison, P. E., K. Charoensiri, D. A. Roberts, S. H. Peterson, and R. O. Green (2006). Wildfire temperature and land cover modeling using hyperspectral data. *Remote Sensing of Environment*, vol. 100, no. 2, pp. 212–222. DOI: 10.1016/j.rse.2005.10.007.

Dennison, P. E. and D. S. Matheson (2011). Comparison of fire temperature and fractional area modeled from SWIR, MIR, and TIR multispectral and SWIR hyperspectral airborne data. *Remote Sensing of Environment*, vol. 115, no. 3, pp. 876–886. DOI: 10.1016/j.rse.2010.11.015.

Dennison, P. E. and D. A. Roberts (2009). Daytime fire detection using airborne hyperspectral data. *Remote Sensing of Environment*, vol. 113, no. 8. 00013, pp. 1646–1657. DOI: 10.1016/j.rse.2009.03.010.

Dozier, J. (1981). A method for satellite identification of surface temperature fields of subpixel resolution. *Remote Sensing of Environment*, vol. 11, pp. 221–229. DOI: 10.1016/0034-4257(81)90021-3.

Feingersh, T. and E. Ben Dor (2015). SHALOM—A Commercial Hyperspectral Space Mission. *Optical Payloads for Space Missions*, p. 247.

Flannigan, M. D. and T. H. V. Haar (1986). Forest fire monitoring using NOAA satellite AVHRR. *Canadian Journal of Forest Research*, vol. 16, pp. 975–982. DOI: 10.1139/x86-171.

Friedman, J., T. Hastie, and R. Tibshirani (2001). Chapter 7: Model assessment and selection. In: *The Elements of Statistical Learning*. Springer series in statistics Springer, Berlin.

Giglio, L., I. Csiszar, Á. Restás, J. T. Morisette, W. Schroeder, D. Morton, and C. O. Justice (2008). Active fire detection and characterization with the advanced spaceborne thermal emission and reflection radiometer (ASTER). *Remote Sensing of Environment*, vol. 112, no. 6, pp. 3055–3063. DOI: 10.1016/j.rse.2008.03.003.

Giglio, L., J. Descloitres, C. O. Justice, and Y. J. Kaufman (2003). An Enhanced Contextual Fire Detection Algorithm for MODIS. *Remote Sensing of Environment*, vol. 87, no. 2, pp. 273–282. DOI: 10.1016/S0034-4257(03)00184-6.

Giglio, L. and J. D. Kendall (2001). Application of the Dozier retrieval to wildfire characterization: a sensitivity analysis. *Remote Sensing of Environment*, vol. 77, no. 1, pp. 34–49. DOI: 10.1016/S0034-4257(01)00192-4.

Giglio, L., J. T. Randerson, and G. R. van der Werf (2013). Analysis of daily, monthly, and annual burned area using the fourth-generation global fire emissions database (GFED4). *Journal of Geophysical Research: Biogeosciences*, vol. 118, no. 1, pp. 317–328. DOI: 10.1002/jgrg.20042.

Giglio, L., W. Schroeder, and C. O. Justice (2016). The collection 6 MODIS active fire detection algorithm and fire products. *Remote Sensing of Environment*, vol. 178, pp. 31–41. DOI: 10.1016/j.rse.2016.02.054.

Goodenough, D., A. Dyk, K. Niemann, J. Pearlman, H. Chen, T. Han, M. Murdoch, and C. West (2003). Processing Hyperion and ALI for forest classification. *IEEE Transactions on Geoscience and Remote Sensing*, vol. 41, no. 6. 00211, pp. 1321–1331. DOI: 10.1109/TGRS.2003.813214.

Grell, G., S. R. Freitas, M. Stuefer, and J. Fast (2011). Inclusion of biomass burning in WRF-Chem: impact of wildfires on weather forecasts. *Atmos. Chem. Phys.* Vol. 11, no. 11, pp. 5289–5303. DOI: 10.5194/acp-11-5289-2011.

Ham, J., Y. Chen, M. M. Crawford, and J. Ghosh (2005). Investigation of the random forest framework for classification of hyperspectral data. *IEEE Transactions on Geoscience and Remote Sensing*, vol. 43, no. 3, pp. 492–501. DOI: 10.1109/TGRS.2004.842481.

Ichoku, C., R. Kahn, and M. Chin (2012). Satellite contributions to the quantitative characterization of biomass burning for climate modeling. *Atmospheric Research*, vol. 111, pp. 1–28. DOI: 10.1016/j.atmosres.2012.03.007.

Jia, G. J., I. C. Burke, M. R. Kaufmann, A. F. Goetz, B. C. Kindel, and Y. Pu (2006). Estimates of forest canopy fuel attributes using hyperspectral data. *Forest Ecology and Management*, vol. 229, no. 1, pp. 27–38. DOI: 10.1016/j.foreco.2006.03.021.

Johnstone, J. F., T. N. Hollingsworth, F. S. Chapin, and M. C. Mack (2010). Changes in fire regime break the legacy lock on successional trajectories in Alaskan boreal forest. *Global Change Biology*, vol. 16, no. 4, pp. 1281–1295. DOI: 10.1111/j.1365-2486.2009.02051.x.

Jones, E., T. Oliphant, P. Peterson, et al. (2001–). *SciPy: Open source scientific tools for Python*. [Online; accessed 2017-09-11]. URL: <http://www.scipy.org/>.

Kasischke, E. S., D. L. Verbyla, T. S. Rupp, A. D. McGuire, K. A. Murphy, R. Jandt, J. L. Barnes, E. E. Hoy, P. A. Duffy, M. Calef, and M. R. Turetsky (2010). Alaska's changing fire regime – implications for the vulnerability of its boreal forests. *Canadian Journal of Forest Research*, vol. 40, no. 7, pp. 1313–1324. DOI: 10.1139/X10-098.

Kasischke, E. S., D. Williams, and D. Barry (2002). Analysis of the patterns of large fires in the boreal forest region of Alaska. *Int. J. Wildland Fire*, vol. 11, no. 2, pp. 131–144. DOI: 10.1071/WF02023.

Kaufman, Y. J., C. O. Justice, L. P. Flynn, J. D. Kendall, E. M. Prins, L. Giglio, D. E. Ward, W. P. Menzel, and A. W. Setzer (1998). Potential global fire monitoring from EOS-MODIS. *Journal of Geophysical Research*, vol. 103, PP. 32, 215–32, 238. DOI: 199810.1029/98JD01644.

Kaufmann, H., K. Segl, S. Chabrillat, S. Hofer, T. Stuffler, A. Mueller, R. Richter, G. Schreier, R. Haydn, and H. Bach (2006). EnMAP A Hyperspectral Sensor for Environmental Mapping and Analysis. In: 2006 IEEE International Symposium on Geoscience and Remote Sensing, pp. 1617–1619. DOI: 10.1109/IGARSS.2006.417.

Lee, C. M., M. L. Cable, S. J. Hook, R. O. Green, S. L. Ustin, D. J. Mandl, and E. M. Middleton (2015). An introduction to the NASA Hyperspectral InfraRed Imager (HyspIRI) mission and preparatory activities. *Remote Sensing of Environment*. Special Issue on the Hyperspectral Infrared Imager (HyspIRI), vol. 167, pp. 6–19. DOI: 10.1016/j.rse.2015.06.012.

Lentile, L. B., Z. A. Holden, A. M. S. Smith, M. J. Falkowski, A. T. Hudak, P. Morgan, S. A. Lewis, P. E. Gessler, and N. C. Benson (2006). Remote sensing techniques to assess active fire characteristics and post-fire effects. *International Journal of Wildland Fire*, vol. 15, no. 3. 00293, pp. 319–345. DOI: 10.1071/WF05097.

Lewis, S. A., A. T. Hudak, R. D. Ottmar, P. R. Robichaud, L. B. Lentile, S. M. Hood, J. B. Cronan, and P. Morgan (2011). Using hyperspectral imagery to estimate forest floor consumption from wildfire in boreal forests of Alaska, USA. *International Journal of Wildland Fire*, vol. 20, no. 2, pp. 255–271. DOI: 10.1071/WF09081.

Middleton, E., P. K. E. Campbell, S. Ungar, L. Ong, Q. Zhang, K. Huemmrich, D. Mandl, and S. Frye (2010). Using EO-1 Hyperion images to prototype environmental products for HyspIRI. In: *Geoscience and Remote Sensing Symposium (IGARSS), 2010 IEEE International*. Geoscience and Remote Sensing Symposium (IGARSS), 2010 IEEE International, pp. 4256–4259. DOI: 10.1109/IGARSS.2010.5648946.

Middleton, E., S. Ungar, D. Mandl, L. Ong, S. Frye, P. Campbell, D. Landis, J. Young, and N. Pollock (2013). The Earth Observing One (EO-1) Satellite Mission: Over a Decade in Space. *IEEE Journal of Selected Topics in Applied Earth Observations and Remote Sensing*, vol. 6, no. 2. 00006, pp. 243–256. DOI: 10.1109/JSTARS.2013.2249496.

Pearlman, J., P. Barry, C. Segal, J. Shepanski, D. Beiso, and S. Carman (2003). Hyperion, a space-based imaging spectrometer. *IEEE Transactions on Geoscience and Remote Sensing*, vol. 41, no. 6. 00309, pp. 1160–1173. DOI: 10.1109/TGRS.2003.815018.

Pedregosa, F., G. Varoquaux, A. Gramfort, V. Michel, B. Thirion, O. Grisel, M. Blondel, P. Prettenhofer, R. Weiss, V. Dubourg, J. Vanderplas, A. Passos, D. Cournapeau, M. Brucher, M. Perrot, and É. Duchesnay (2011). Scikit-learn: Machine Learning in Python. *Journal of Machine Learning Research*, vol. 12, 2825–2830.

Prakash, A., K. Schaefer, W. K. Witte, K. Collins, R. Gens, and M. P. Goyette (2011). A Remote Sensing and GIS Based Investigation of a Boreal Forest Coal Fire. *International Journal of Coal Geology*, vol. 86, no. 1, pp. 79–86. DOI: 10.1016/j.coal.2010.12.001.

Randerson, J. T., H. Liu, M. G. Flanner, S. D. Chambers, Y. Jin, P. G. Hess, G. Pfister, M. C. Mack, K. K. Treseder, L. R. Welp, F. S. Chapin, J. W. Harden, M. L. Goulden, E. Lyons, J. C. Neff, E. a. G. Schuur, and C. S. Zender (2006). The Impact of Boreal Forest Fire on Climate Warming. *Science*, vol. 314, no. 5802, pp. 1130–1132. DOI: 10.1126/science.1132075.

Realmuto, V. J., P. E. Dennison, M. Foote, M. S. Ramsey, M. J. Wooster, and R. Wright (2015). Specifying the saturation temperature for the HyspIRI 4- μm channel. *Remote Sensing of Environment*. Special Issue on the Hyperspectral Infrared Imager (HyspIRI), vol. 167, pp. 40–52. DOI: 10.1016/j.rse.2015.04.028.

Rein, G., N. Cleaver, C. Ashton, P. Pironi, and J. L. Torero (2008). The severity of smouldering peat fires and damage to the forest soil. *CATENA. Fire Effects on Soil Properties*, vol. 74, no. 3, pp. 304–309. DOI: 10.1016/j.catena.2008.05.008.

Roberts, D. A., P. E. Dennison, M. Gardner, Y. Hetzel, S. Ustin, and C. Lee (2003). Evaluation of the potential of Hyperion for fire danger assessment by comparison to the Airborne Visible/Infrared Imaging Spectrometer. *IEEE Transactions on Geoscience and Remote Sensing*, vol. 41, no. 6. 00096, pp. 1297–1310. DOI: 10.1109/TGRS.2003.812904.

Roberts, D. A., M. Gardner, R. Church, S. Ustin, G. Scheer, and R. O. Green (1998). Mapping chaparral in the Santa Monica Mountains using multiple endmember spectral mixture models. *Remote Sensing of Environment*, vol. 65, no. 3. 00684, pp. 267–279. DOI: 10.1016/S0034-4257(98)00037-6.

Roberts, D. A., D. A. Quattrochi, G. C. Hulley, S. J. Hook, and R. O. Green (2012). Synergies between VSWIR and TIR data for the urban environment: An evaluation of the potential for the Hyperspectral Infrared Imager (HypIRI) Decadal Survey mission. *Remote Sensing of Environment. Remote Sensing of Urban Environments*, vol. 117, pp. 83–101. DOI: 10.1016/j.rse.2011.07.021.

Robinson, J. M. (1991). Fire from space: Global fire evaluation using infrared remote sensing. *International Journal of Remote Sensing*, vol. 12, no. 1, pp. 3–24. DOI: 10.1080/01431169108929628.

Schroeder, W., P. Oliva, L. Giglio, and I. A. Csiszar (2014). The New VIIRS 375 m active fire detection data product: Algorithm description and initial assessment. *Remote Sensing of Environment*, vol. 143, pp. 85–96. DOI: 10.1016/j.rse.2013.12.008.

Schroeder, W., P. Oliva, L. Giglio, B. Quayle, E. Lorenz, and F. Morelli (2015). Active fire detection using Landsat-8/OLI data. *Remote Sensing of Environment*. DOI: 10.1016/j.rse.2015.08.032.

Simon, K. (2006). *Hyperion Level 1GST (L1GST) Product Output Files Data Format Control Book (DFCB)*. EO1-DFCB-0003. Department of the Interior US Geological Survey.

Ungar, S., J. Pearlman, J. Mendenhall, and D. Reuter (2003). Overview of the Earth Observing One (EO-1) mission. *IEEE Transactions on Geoscience and Remote Sensing*, vol. 41, no. 6. 00243, pp. 1149–1159. DOI: 10.1109/TGRS.2003.815999.

Vodacek, A., R. L. Kremens, A. J. Fordham, S. C. Vangorden, D. Luisi, J. R. Schott, and D. J. Latham (2002). Remote optical detection of biomass burning using a potassium emission signature. *International Journal of Remote Sensing*, vol. 23, no. 13, pp. 2721–2726. DOI: 10.1080/01431160110109633.

Wendler, G., J. Conner, B. Moore, M. Shulski, and M. Stuefer (2010). Climatology of Alaskan wild-fires with special emphasis on the extreme year of 2004. *Theoretical and Applied Climatology*, vol. 104, no. 3, pp. 459–472. DOI: 10.1007/s00704-010-0357-9.

Wright, R., H. Garbeil, and A. G. Davies (2010). Cooling rate of some active lavas determined using an orbital imaging spectrometer. *Journal of Geophysical Research: Solid Earth (1978–2012)*, vol. 115. DOI: 10.1029/2009JB006536.

Chapter 4

SENSITIVITY CONSIDERATIONS IN FIRE DETECTION AND SUB-PIXEL FIRE TEMPERATURE RETRIEVAL WITH SUOMI-NPP VIIRS¹

Abstract

The sensitivity of fire detection performance to sensor zenith angle was investigated for the Visible Infrared Imaging Radiometer Suite (VIIRS). The test case was a dataset consisting of 146 scenes covering 16 days of acquisition over a large boreal forest fire in north-eastern interior Alaska. Both the global VIIRS 375 m I-band product and the VIIRS I-band Fire Detection Algorithm for High Latitudes (VIFDAHL) were examined. In either case, the fire detection likelihood falls off at sensor zenith angles above approximately 50°. VIFDAHL detects more active fire locations than the global product at zenith angles between 20° and 40°, whereas at angles >50°, where the detection performance of both products falls off, the global product performs somewhat better than VIFDAHL. Furthermore, active fire temperatures and fractional fire areas were retrieved using VIIRS 750 m M-band data. The resulting temperature range from 500 K to >1100 K, with fractional areas between 0.1 % and 3 % of a pixel.

4.1 Introduction

Whenever we use or evaluate a satellite-based fire detection product (e.g. Csiszar et al. 2014; Giglio et al. 2003, 2016; Schroeder et al. 2014; Waigl et al. 2017), it is useful to keep its potential limitations in mind: To what extent does the product characterize fire adequately and without bias? If there are biases and sensitivities, what parameters and properties are affected? What further processing steps could be taken to enhance fire characterization? This chapter builds on our previous work on global and Alaska-specific (VIFDAHL) active fire detection products

¹Waigl C. F. et al., manuscript in preparation (formatted for submission to the International Journal of Applied Earth Observation and Geoinformation)

using at-sensor spectral radiance data from the Visible Infrared Imaging Radiometer Suite (VIIRS) (Waigl et al. 2017). It addresses the following two topics:

- the scan angle dependency of VIIRS-based fire detections,
- the feasibility of sub-pixel active fire temperature retrieval with VIIRS data.

Sensitivity considerations are integral to any detection methodology. Fire detection limits are typically evaluated using case studies with available high-resolution proxy-data complementing the detection algorithm of interest (Giglio et al. 2003). Schroeder et al. (2008) validated fire detections from the Moderate Resolution Imaging Spectroradiometer (MODIS) and the Wildfire Automated Biomass Burning Algorithm (WF_ABBA) based on data from the Geostationary Operational Environmental Satellite (GOES) using higher resolution data acquired by the Advanced Spaceborne Thermal Emission and Reflection Radiometer (ASTER) or Landsat's Enhanced Thematic Mapper (ETM+). In a different type of sensitivity analysis, Schroeder et al. (2010) indicated that retrievals of Fire Radiative Power (FRP) from MODIS and GOES/WF_ABBA may be sensitive to biomass density as well as affected by errors caused by the effects of the point-spread function.

Regarding active fire detection, a dependency on sensor look angle can be expected: Data acquired at large angles is affected to a greater degree by atmospheric effects and topography. Furthermore, the footprint of a pixel on the ground increases, so a fire source is likely to occupy a smaller percentage of the pixel. Boles and Verbyla (1999) found that for the Advanced Very High Resolution Radiometer (AVHRR), a sensor in the 1-km class of spatial resolution, fire detection likelihoods did not vary very much with scan angle.

Uncertainty and sensitivity considerations are also particularly relevant in sub-pixel fire temperature and fractional area retrieval studies. Sub-pixel fire temperature retrieval was first developed in the 1980s for AVHRR, a sensor on several polar-orbiting weather satellites operated by the United States National Oceanic and Atmospheric Administration (NOAA) (Dozier 1981; Matson and Dozier 1981). The approach is widely referred to as the Dozier method. It relies on measuring spectral radiance in two bands that are sensitive to the emitted thermal background, and operate in sufficiently distinct wavelength ranges to distinguish between high-temperature sources and

non-fire background. This method is conceptually similar to fire (or lava) temperature retrieval in hyperspectral data using a linear spectral mixture model (Abrams et al. 2013; Dennison et al. 2006): measured radiance data is used to fit model parameters which include active fire temperatures and the fractional area of a pixel occupied by fire at that temperature. In multispectral sensors such as AVHRR, MODIS or GOES the fire-sensitive band is typically a mid-infrared (MIR) band with a central wavelength of approximately 4 μm , while a thermal infrared (TIR) band centered at approximately 11 μm is used for background detection. The Dozier method is an integral part of WF_ABBA for geostationary satellites (Prins and Menzel 1994) and was fundamental to the design of the Bi-spectral Infrared Detection (BIRD) satellite system (Briess et al. 2003). The method has been extended to other sub-pixel retrieval problems, such as snow properties (Dozier and Painter 2004).

Giglio and Kendall (2001) described the limitations of Dozier's two-component approach. They found that for MODIS, at and above a realistic limit for fractional pixel area of 0.5% of a pixel's size, errors in retrieved fire temperature and in retrieved fire pixel area up to 100 K and 50%, respectively, are possible. But for smaller fractional areas, errors quickly overwhelm the retrieval result. Furthermore, at larger fractional pixel areas occupied by fire, the MODIS 3.959 μm MIR band 21 saturates at a fractional active fire area of approximately 3% of a pixel, so the window for a meaningful application of the Dozier method to MODIS data is rather narrow. The situation is even less favorable for AVHRR, which has a MIR channel more prone to saturation. Similarly, Giglio and Justice (2003) indicated that wavelength selection can have a rather dramatic effect on the retrieved active fire temperatures and fractional pixel areas, based on data from MODIS and AVHRR.

Sub-pixel fire characterization is not only applied to fire temperature. Schroeder et al. (2010) combined active fire temperature retrieval in MODIS (and WF_ABBA) with a study of the associated FRP. Peterson et al. (2012) (see also Peterson and Wang 2013) calculated FRP on the basis of physical principles (the Stefan-Boltzmann equation) instead of the empirical formula used in the MODIS fire products (Kaufman et al. 1998).

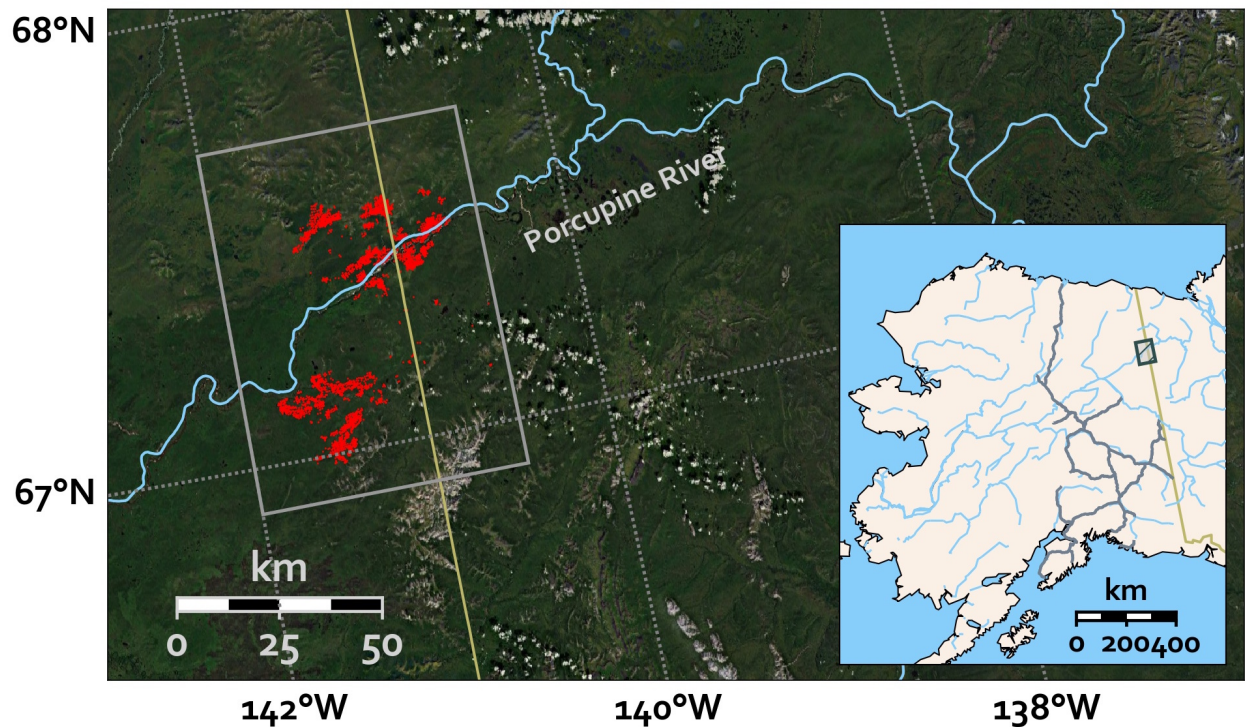


Figure 4.1: Within the rectangular area, all fire detections from the global VIIRS I-band product between July 9, 2017 and July 24, 2017, are shown in red

Other uses of sub-pixel active fire detection include a Dozier-like method applied to ~30 m resolution Landsat data for the detection of sub-surface coal seam fires with TM and ETM+ data (Prakash and Gupta 1999) and the construction of a spectral mixture model based on the full 36-band MODIS spectrum (Eckmann et al. 2008). Similarly, up to 8 bands of VIIRS 750 m (“moderate resolution”) M-band data has been used to retrieve fire temperatures (Liew et al. 2015), but results appear to have a strong sensitivity to the addition or omission of individual TIR bands.

In this work, we also use VIIRS M-band data for sub-pixel fire retrieval, but focus on two components that are as close as possible to Dozier’s original mode: one mid-infrared and one thermal infrared band.

4.2 Study area and data used

Our study area consists of a cluster of wildfires that were ignited by lightning in the remote area along the Alaska/Canadian border north and south of the Porcupine River between late June

and early July 2017. We selected this site because it experienced sustained wildfire that was active over an extended period of time (one full VIIRS repeat cycle of 16 days), with limited cloud cover and little variation in vegetation cover and topography. The site is moderately rugged and inaccessible by road; the vegetation is dominated by black spruce. Other than the protection of a small number of cabins and archaeological sites, including the historical site of Rampart House located very close to the border, there was little fire suppression activity. The study area is located between 66.9°N and 67.7°N latitude, 140.5°W and 142.0°W longitude (Figure 4.1)

The time interval of the study extended from July 9, 2017 to July 24, 2017 (UTC). During this 16-day interval, VIIRS executed 227 orbits. The full set of corresponding VIIRS Sensor Data Record (SDR) datasets, which contain at-sensor corrected radiance raster data, was downloaded from the direct readout downlink station operated by the Geographic Information Network of Alaska at the University of Alaska Fairbanks (UAF), which receives and processes VIIRS data to SDR level. The dataset consisted of 146 scenes that overlap with the study area (Table 4.2), each of them a granule that corresponds to ~85 sec of data acquisition, with a swath width of ~3040 km. We used band M13, centered at 4.05 μm and band M15, centered at 10.763 μm (Cao et al. 2014).

In addition to VIIRS SDR data, we also downloaded all VIIRS I-band (375 m) global fire detections (Schroeder et al. 2014) from NASA's Fire Information for Resource Management System (FIRMS) [<https://earthdata.nasa.gov/firms>] for the study area and time interval.

4.3 Methods

4.3.1 *Fire detection*

For the fire pixels provided by the global VIIRS I-band (375 m) active fire product (Figure 4.1), we determined the corresponding original granule by matching the location and the acquisition time stamp, and counted the detections associated with each granule. We also determined the sensor zenith angle at the center of the study area for each granule from the granule's geolocation data. The variation of the sensor zenith angle across our small study areas is <1°, so we considered it sufficient to use the study area center to associate global VIIRS I-band (375 m) fire detections with sensor zenith angles.

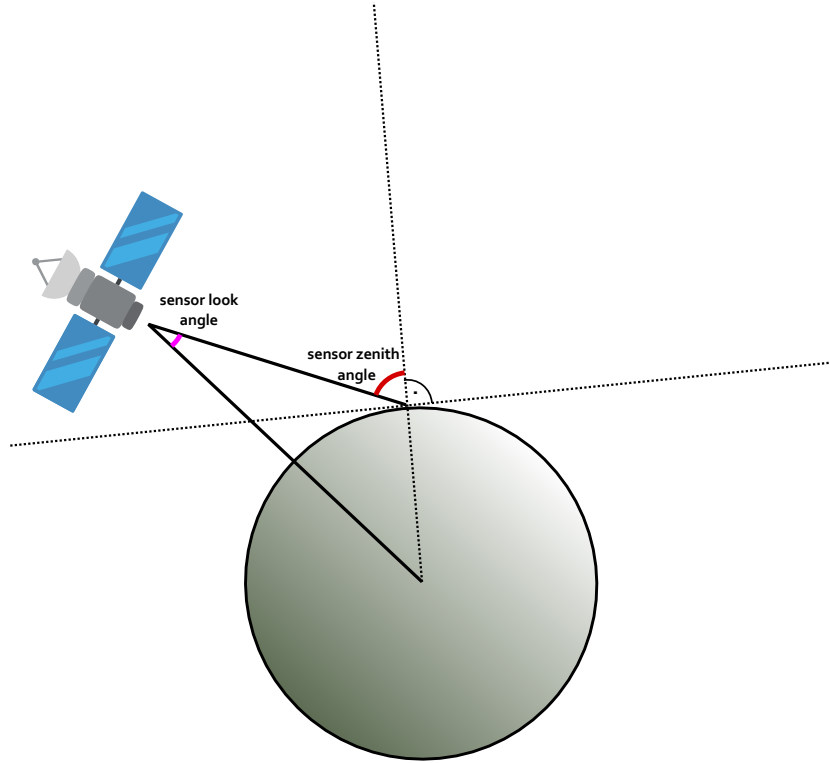


Figure 4.2: Sensor look angle (pink) and sensor zenith angle (red). The first is a property of the sensor design, the second depends on the sensor look angle and the earth’s radius.

We also processed all 146 granules in the study set with VIFDAHL, which provided a second set of fire pixels, separated into high- and low-intensity detections. Our implementation of VIFDAHL simultaneously extracts the sensor zenith angle associated with each fire pixel from the geolocation dataset.

4.3.2 *Sensor angle statistics*

The VIIRS sensor scans the earth at a scan angle (or sensor look angle, both defined with reference to nadir) of $\pm 56.28^\circ$ from nadir (Cao et al. 2014). In our data, this translates in sensor zenith angles that vary from 0° to just over 70° on either side of nadir. (The zenith angle is larger than the scan angle because of the curvature of the earth surface, see Figure 4.2.) Retaining all granules with at least one fire detection from either VIFDAHL or the global VIIRS I-band (375 m) product, we examined the distribution of the zenith angles associated with fire detections.

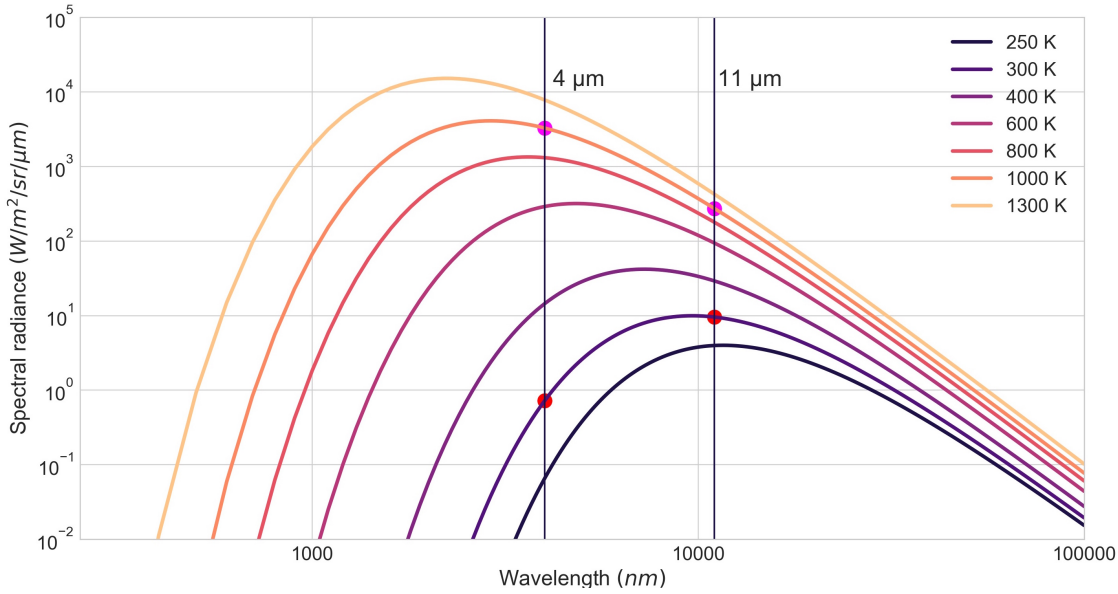


Figure 4.3: Planck blackbody spectral radiance curves. The approximate locations of the MIR ($4 \mu\text{m}$) and TIR ($11 \mu\text{m}$) bands are marked with vertical lines.

4.3.3 Temperature retrieval

A body at a temperature T with a wavelength-dependent emissivity ε_λ emits electromagnetic radiation with a spectral radiance that follows Planck's Law:

$$L_\lambda = \varepsilon_\lambda \frac{C_1}{\lambda^5} \frac{1}{\pi (e^{\frac{C_2}{\lambda T}} - 1)} = \varepsilon_\lambda \frac{K_1(\lambda)}{e^{\frac{K_2(\lambda)}{T}} - 1} = \varepsilon_\lambda B(\lambda, T) \quad (4.1)$$

with

constants $C_1 = 2\pi \hbar c^2$ and $C_2 = hc/k_B$

wavelength-dependent parameters $K_1 = C_1/\pi \lambda^5$ and $K_2 = C_2/\lambda$

Planck's constant $\hbar = 6.626\,070\,04 \times 10^{-34} \text{ m}^2\text{kg/s}$

Boltzmann's constant $k_B = 1.380\,648\,52 \times 10^{-23} \text{ m}^2\text{kg/(s}^2\text{K)}$

speed of light $c = 2.997\,924\,58 \times 10^8 \text{ m/s}$.

In the following we will assume an emissivity value of 1 as a first approximation.

If the footprint of a pixel consisted of two homogeneous sub-pixel areas – a fractional area p that is burning at a flaming temperature of T (e.g., 1000 K) and a background area $1 - p$ at the land surface temperature (in the vicinity of 300 K) – the spectral radiance emitted by the mixed pixel would be the sum of the two contributions:

$$L_{\lambda, \text{pixel}} = \tau_\lambda p B(\lambda, T_{\text{fire}}) + (1 - p) L_{\lambda, b} \quad (4.2)$$

with

$L_{\lambda, \text{pixel}}$: observed radiance of a pixel

$L_{\lambda, b}$: observed radiance of the background

τ_λ : upward atmospheric transmittance

p : fractional area of the pixel occupied by fire (between 0 and 1)

$B(\lambda, T_{\text{fire}})$: Planck spectral radiance curve at the fire temperature

In Equation 4.2, the first (“fire”) term is corrected with the wavelength-dependent transmittance τ_λ , and T_{fire} stands for a real (kinetic) temperature. The background radiance term $L_{\lambda, b}$ represents the measured at-sensor spectral radiance of the background, and the corresponding temperature T_b is a brightness temperature value.

The concept underlying Dozier’s method is that the active fire component of the mixed pixel contributes a higher spectral radiance in the MIR (4 μm) than in the TIR (11 μm), and that the opposite is true for the cooler background component (see Figure 4.3). For a single band, the measured spectral radiance could result from a small fire area burning at a high temperature, or a larger fire area burning at a lower temperature. If, however, we take the data from both a MIR and a TIR band, only one fire temperature and fractional area combination fits the measured radiance according to Equation 4.2. The values for K_1 and K_2 resulting from the band M13 and M15 wavelengths are summarized in Table 4.1.

Table 4.1: Parameters for VIIRS M-bands used in Dozier retrieval

VIIRS band	Central wavelength (μm)	K1 W/($\text{m}^2 \mu\text{m sr}$)	K2 (K)
M13	4.05	109308	3552.53
M15	10.763	824.630	1336.78

4.3.4 Atmospheric correction

For the atmospheric transmittance value in Equation 4.2 we used wavelength-dependent values from Giglio and Schroeder (2014) in the MIR (band M13) and a constant value of 0.86 (e.g. Giglio and Kendall 2001). These published values are based on the MODTRAN radiative transfer model (Berk et al. 2006).

4.3.5 Uncertainty estimation

We could solve the two equations 4.2 (one for the MIR band and one for the TIR band) numerically for each fire pixel to fit values of p and T_{fire} . This, however, would not provide us with any information about the uncertainties inherent in fire temperature retrieval. We therefore use a slightly different approach. Equation 4.2 has the form of a forward model, in which the measured data $d = (L_{\text{MIR,pixel}}, L_{\text{TIR,pixel}})$ are expressed in terms of model parameters $m = (p, T_{\text{fire}}, T_{b,\text{MIR}}, T_{b,\text{TIR}})$. Such a model can be solved using inverse modeling (e.g. Tarantola 2005). We express the error between the calculated model and the measured data for set of model parameters m via a misfit function $F(m)$, which incorporates both model and data errors.

The method allows for great flexibility to incorporate sources of uncertainties or error. As a very simple approximation, the only type of data error we took into consideration was the uncertainty in the VIIRS SDR brightness temperatures. Based on the range of values offered in Cao et al. (2014), we used the values of 0.5 K for band M13 and 0.2 K for band M15. The misfit function is used to calculate a Bayesian posterior probability distribution function:

$$S(m) = K \exp(-F(m)) \quad (4.3)$$

The normalization constant K does not have to be evaluated, as we can sample relative probabilities with a Monte Carlo method according to the Metropolis-Hastings (e.g. Hastings 1970; Metropolis et al. 1953; Tarantola 2005, ch. 2.3). We sample the distribution of model parameters, the spread of which is driven implicitly by the uncertainties incorporated. In each step of the Monte Carlo random walk, a new set of model parameters is randomly selected, and then accepted or not by the rules of the Metropolis algorithm, depending on the posterior distribution. New model parameters are randomly drawn based on a set of prior distribution. The method is not very sensitive to the choice of these priors. For T_{fire} we selected a uniform distribution of temperatures between a minimum of 500 K and a maximum of 1500 K. For background brightness temperatures in both bands we selected a normal distribution centered on 300 K value with a standard deviation of 20 K. Last, because the fractional pixel area is by its nature a ratio (or percentage), a reasonable choice for a prior distribution is a beta distribution (Kruschke 2014, Chapter 5). As we expect modeled pixel areas <5%, a suitable beta function is beta(2, 40), which has a sharply defined peak around 0.025.

4.4 Results and discussion

4.4.1 *Zenith angle dependency of fire detection*

We found that out of the 146 VIIRS scenes that overlap with the study area, 62 granules have at least one fire detection from either the VIIRS I-band (375 m) product or VIFDAHL (Table 4.2). Across this dataset, the number of total global VIIRS I-band detections (3252) and the VIFDAHL detections (3247) are almost identical. Scenes with fire detections are frequently associated with large sensor zenith angles: for 21 out of the 62 granules the zenith angle at the study site exceeds 60° (Figure 4.4). Regarding the fire pixel counts themselves, we found higher counts for VIFDAHL compared to the global VIIRS I-band product at sensor zenith angles between 20° and 40°, and higher counts for the global product at angles >60° (Figure 4.5, a) and c)). Normalizing fire pixel counts by the number of scenes in each zenith angle bin (Figure 4.5, b) and d)), effectively dividing the histograms (Figure 4.5, a) and c)) by the one in Figure 4.4, it became clear that the fire detection

efficiency falls off sharply at angles $>60^\circ$ for both products. The fall-off is more pronounced for VIFDAHL.

Table 4.2: List of 62 VIIRS SDR granules used in this study with non-zero fire detection counts for at least one method (VIIRS I-band or VIFDAHL). Totals are 3252 detections from the global VIIRS I-band product and 3247 from VIFDAHL.

VIIRS orbit	VIIRS granule ID	Date (UTC)	Time (UTC)	Node	Sensor zenith angle	VIIRS-I count	VIFDAHL count
29525	NPP001802682471	2017-07-09	10:30	desc	59.2°	0	1
29526	NPP001802743069	2017-07-09	12:11	desc	2.2°	21	4
29527	NPP001802803668	2017-07-09	13:52	desc	51.4°	0	3
29531	NPP001803040941	2017-07-09	20:28	asc	35.7°	6	0
29532	NPP001803101539	2017-07-09	22:09	asc	32.7°	51	40
29540	NPP001803595716	2017-07-10	11:52	desc	16.6°	0	1
29540	NPP001803596569	2017-07-10	11:54	desc	16.3°	2	0
29545	NPP001803834696	2017-07-10	18:31	asc	65.3°	13	8
29546	NPP001803893587	2017-07-10	20:09	asc	43.7°	90	80
29546	NPP001803894441	2017-07-10	20:10	asc	43.0°	0	1
29546	NPP001803954186	2017-07-10	21:50	asc	20.0°	314	353
29548	NPP001804014784	2017-07-10	23:31	asc	65.8°	93	74
29554	NPP001804387764	2017-07-11	09:52	desc	69.1°	46	0
29555	NPP001804448362	2017-07-11	11:33	desc	29.7°	14	12
29556	NPP001804508961	2017-07-11	13:14	desc	37.8°	2	3
29557	NPP001804627597	2017-07-11	16:32	asc	70.2°	1	0
29559	NPP001804687342	2017-07-11	18:12	asc	67.1°	18	17
29560	NPP001804747087	2017-07-11	19:51	asc	50.1°	122	116
29560	NPP001804806832	2017-07-11	21:31	asc	5.8°	285	370
29561	NPP001804867431	2017-07-11	23:12	asc	60.6°	84	28
29569	NPP001805361607	2017-07-12	12:55	desc	28.1°	15	2
29574	NPP001805659479	2017-07-12	21:12	asc	8.6°	17	21
29575	NPP001805720077	2017-07-12	22:53	asc	54.2°	8	5
29582	NPP001806153655	2017-07-13	10:56	desc	49.8°	6	0
29583	NPP001806214254	2017-07-13	12:37	desc	16.3°	4	0
29584	NPP001806273999	2017-07-13	14:16	desc	57.4°	2	1
29585	NPP001806333744	2017-07-13	15:56	desc	69.1°	3	1
29586	NPP001806392635	2017-07-13	17:34	asc	69.4°	2	2
29587	NPP001806452380	2017-07-13	19:13	asc	59.0°	39	35
29588	NPP001806512125	2017-07-13	20:53	asc	21.6°	213	197
29589	NPP001806572724	2017-07-13	22:34	asc	46.3°	218	146
29596	NPP001807006302	2017-07-14	10:37	desc	57.1°	116	11

Table 4.2 Continued.

VIIRS orbit	VIIRS granule ID	Date (UTC)	Time (UTC)	Node	Sensor zenith angle	VIIRS-I count	VIFDAHL count
29597	NPP001807066900	2017-07-14	12:18	desc	2.6°	6	7
29598	NPP001807127499	2017-07-14	13:59	desc	53.0°	0	8
29599	NPP001807186390	2017-07-14	15:37	desc	67.9°	0	2
29600	NPP001807246135	2017-07-14	17:16	asc	70.1°	3	5
29601	NPP001807305027	2017-07-14	18:55	asc	62.1°	76	83
29602	NPP001807364772	2017-07-14	20:34	asc	32.5°	194	233
29603	NPP001807425370	2017-07-14	22:15	asc	36.4°	367	414
29611	NPP001807858948	2017-07-15	10:18	desc	62.9°	158	10
29612	NPP001807919547	2017-07-15	11:59	desc	11.9°	27	30
29613	NPP001807980145	2017-07-15	13:40	desc	47.5°	8	9
29614	NPP001808039037	2017-07-15	15:18	desc	66.3°	0	5
29614	NPP001808039890	2017-07-15	15:19	desc	66.4°	0	4
29616	NPP001808157673	2017-07-15	18:36	asc	64.6°	22	22
29616	NPP001808158527	2017-07-15	18:37	asc	64.4°	0	4
29617	NPP001808217418	2017-07-15	20:15	asc	41.2°	134	155
29618	NPP001808278017	2017-07-15	21:56	asc	24.3°	273	431
29619	NPP001808338615	2017-07-15	23:37	asc	67.4°	9	10
29632	NPP001809130663	2017-07-16	21:37	asc	10.5°	29	45
29632	NPP001809191262	2017-07-16	23:18	asc	62.5°	2	3
29659	NPP001810776211	2017-07-18	19:20	asc	57.8°	2	2
29660	NPP001810835956	2017-07-18	20:59	asc	17.5°	23	49
29661	NPP001810896555	2017-07-18	22:40	asc	49.1°	21	34
29668	NPP001811330133	2017-07-19	10:43	desc	54.8°	4	0
29673	NPP001811628858	2017-07-19	19:01	asc	61.2°	2	3
29673	NPP001811688603	2017-07-19	20:40	asc	29.1°	34	52
29674	NPP001811749201	2017-07-19	22:21	asc	39.9°	16	50
29687	NPP001812481504	2017-07-20	18:42	asc	63.8°	11	12
29688	NPP001812541249	2017-07-20	20:22	asc	38.5°	2	0
29688	NPP001812601848	2017-07-20	22:03	asc	28.6°	12	10
29689	NPP001812662446	2017-07-20	23:44	asc	68.8°	12	13

It is at first glance surprising that we did not find a larger number of VIFDAHL detections, as in our previous study (Waigl et al. 2017) VIFDAHL consistently outperformed the global product. This result is mitigated when we group the fire pixel counts by node: In VIIRS, the ascending node corresponds to mid-day overpasses, while late evening and early morning acquisitions take place

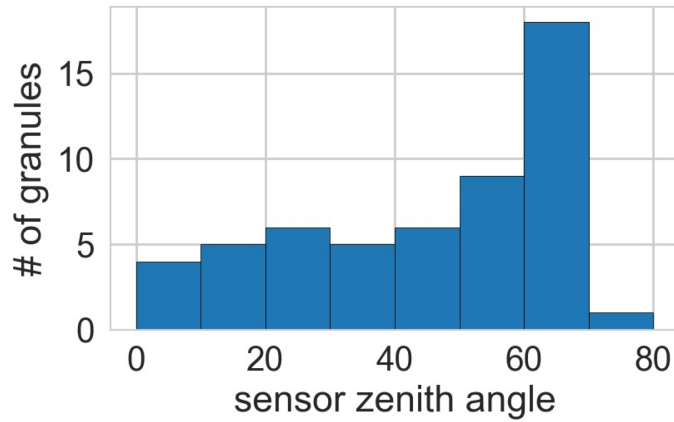


Figure 4.4: Distribution of zenith angles at the center of the 62 VIIRS scenes with nonzero VIFDAHL detections.

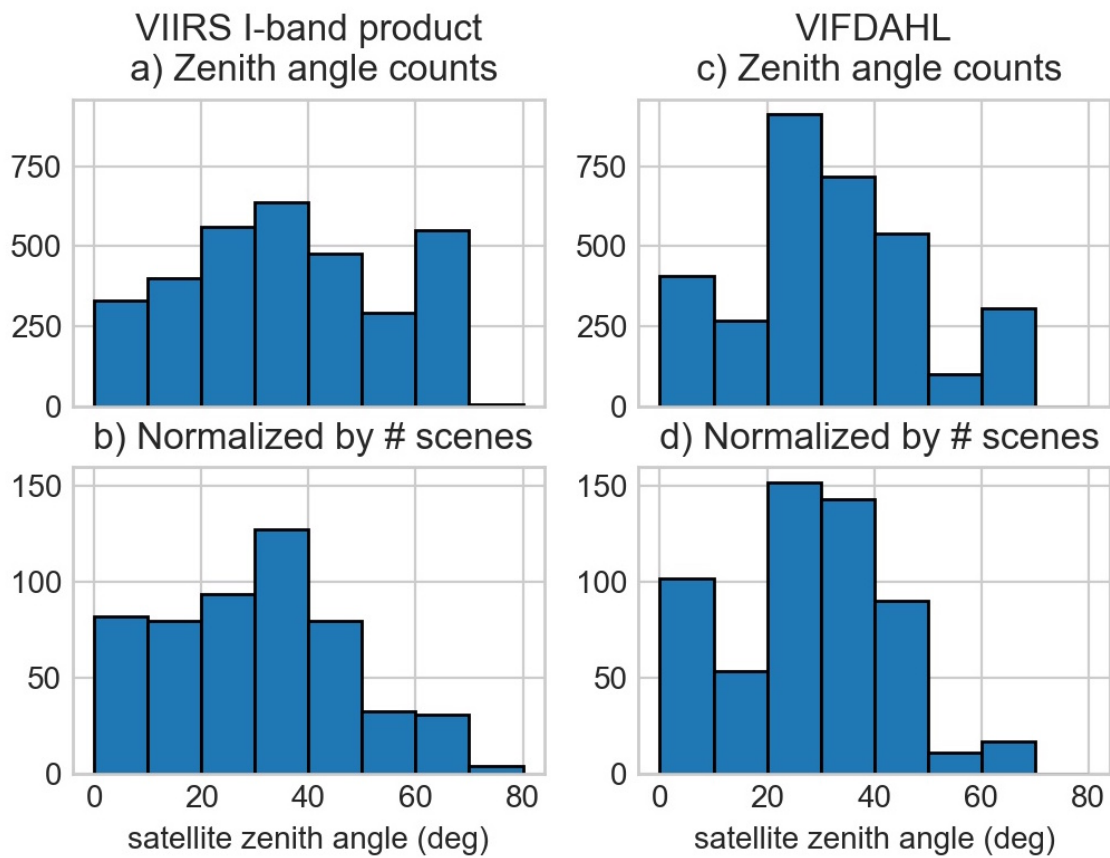


Figure 4.5: VIIRS I-band fire detection counts as a function of satellite zenith angle.

on a descending node. We counted 2818 global VIIRS I-band daytime detections compared to 3123 VIFDAHL daytime detections; conversely, for the evening, night and early morning detections, VIFDAHL yielded only 114 compared to 434 in the global product. The data used originally to tune VIFDAHL contained more day than night scenes, and largely scenes acquired at small zenith angles, and VIFDAHL performs better on ascending-node data and zenith angles $<50^\circ$.

Another aspect of the fire detection comparison is linked to data removal at the granule edge and bowtie overlaps (that is, the geometric growth of the pixel footprint at large scan angles). VIIRS I-band and M-band SDR data undergoes a bowtie deletion scheme which partially, but not completely, removes pixel duplication due to the bowtie effect (Hillger et al. 2015; Hillger et al. 2014). Our implementation of VIFDAHL quite aggressively removes all residual bowtie overlaps as well as any duplication of detection location at adjacent granule edges. Example scenes for which the VIIRS I-band product retains overlapping detections eliminated by VIFDAHL are the two granules from orbit 29688 in Table 4.2.

4.4.2 Fire temperature and partial pixel area retrieval

To carry out sub-pixel temperature and fractional area retrieval, we selected a sample scene from an active phase of the fire, acquired on July 13 at 20:53 UTC (197 VIFDAHL detections). This is a daytime scene acquired on an ascending node, and at a moderate sensor zenith angle of approximately 21° . The 197 VIFDAHL detections are located within 106 M-band pixels (with a resolution of 750 m at nadir) (Figure 4.6). Four I-band pixels are nested within each M-band pixel.

These 106 M-band pixels formed the basis for the application of Dozier's method (Equation 4.2). For the TIR transmittance parameter in the thermal infrared, Giglio and Kendall (2001) used a value of 0.86. We use the same value for VIIRS as an approximation, as the spectral locations of MODIS TIR band 31 and VIIRS band M15 are close (Cao et al. 2014). In contrast, VIIRS band M13 is positioned at the very edge of its atmospheric window at a central wavelength of 4.05 μm (Figure 4.7 a)), where the atmospheric transmittance is already reduced. We therefore turned the transmittance values provided by Schroeder and Giglio (2016), using model output based on MODTRAN (Figure 4.7 b)). They show that even at nadir, the atmospheric transmittance only

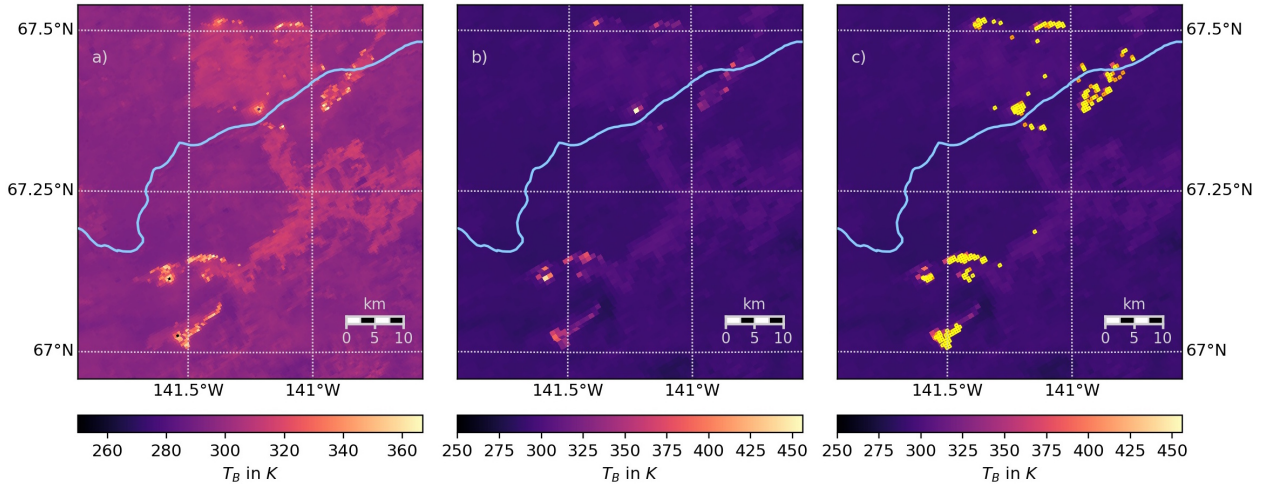


Figure 4.6: VIIRS MIR spectral radiance for one example scene (2017-07-13 20:53 UTC / 12:53 AKDT) with 197 VIFDAHL detections. a) Band I4. b) Band M13. c) Band M13 with VIFDAHL detections overlaid in yellow (high intensity) and orange (low intensity). The VIFDAHL detections map very well to the the M13 brightness temperature plot. The Porcupine River is marked in blue.

Table 4.3: Sample results of M-band sub-pixel temperature retrieval, sorted by fractional pixel area occupied by fire. Temperatures are given in K, and spectral radiances in $\text{W}/(\text{m}^2 \mu\text{m sr})$.

T_b (MIR)	T_b (TIR)	Spectral radiance (MIR)	Spectral radiance (TIR)	Pixel (fraction)	Fire temperature
367.4	291.8	7.0	8.5	0.1%	1500
301.8	290.6	0.9	8.4	0.1%	500
308.8	291.0	1.1	8.4	0.2%	587
335.4	292.5	2.8	8.6	0.2%	814
351.0	294.2	4.5	8.9	0.3%	844
325.4	292.6	2.0	8.6	0.3%	662
351.0	295.9	4.5	9.1	0.6%	728
342.9	295.5	3.5	9.0	0.7%	668
300.9	296.2	0.8	9.1	0.7%	500
379.0	299.7	9.5	9.6	0.8%	833
390.1	302.3	12.3	10.0	1.0%	849
362.1	298.8	6.1	9.5	1.0%	712
442.3	311.3	36.0	11.4	1.0%	1129
336.5	296.1	2.9	9.1	1.1%	591
357.6	301.1	5.4	9.8	1.8%	623
323.4	297.1	1.9	9.3	1.9%	500
339.8	298.6	3.2	9.5	1.9%	555
352.0	300.4	4.6	9.7	1.9%	599
395.4	308.6	13.9	11.0	2.0%	742
419.2	313.4	23.2	11.7	2.0%	836

322.7	298.2	1.9	9.4	2.0%	500
322.3	298.6	1.8	9.5	2.0%	500
357.4	301.8	5.4	9.9	2.1%	607
326.9	297.8	2.1	9.4	2.2%	500
345.9	300.9	3.9	9.8	2.5%	552
379.2	308.9	9.5	11.0	3.0%	636
346.8	302.5	4.0	10.0	3.2%	536
456.0	332.2	45.7	15.0	3.8%	848

barely exceeds 0.7 and falls off steeply at the swath edge. We used a transmittance value of 0.7 for the 21° MIR data.

Active fire temperature was allowed range from 500 K and 1500 K. For some pixels that were examined, the retrieved fire temperatures in the model output took on one of these values. For example, a low retrieved temperature with a small fractional pixel area can occur when a single low-intensity fire detection occurs within a (larger) M-band pixel. In other pixels, a very high fire temperature is associated with unreliable detection of fractional pixel area when one of the bands is close to saturation. These cases represent the limits of the Dozier method. A sample of pixels with meaningful results of the Dozier retrieval is presented in Table 4.3. For these pixels, fractional fire areas of the order of 0.2–2% of a pixel are common; associated errors (one standard deviation) varied between 0.2% and 0.8%. Average standard of the retrieved fire temperatures were 9 K for low-temperature fire and approximately 27 K for temperatures of the 800–900 K range. The background brightness temperatures, which we treated as model parameters, were distributed around the values of 300 K in band M13 and 290 K in band M15, with standard deviations varying between 1 K and 6 K.

In this example scene, fire temperature and fractional fire area retrieval yielded a plausible result. Dozier’s bi-spectral model is applicable to VIIRS M-band data. At the lower detection limit, 0.2% of a 750 m pixel corresponds to an area of about 33 × 33 m.

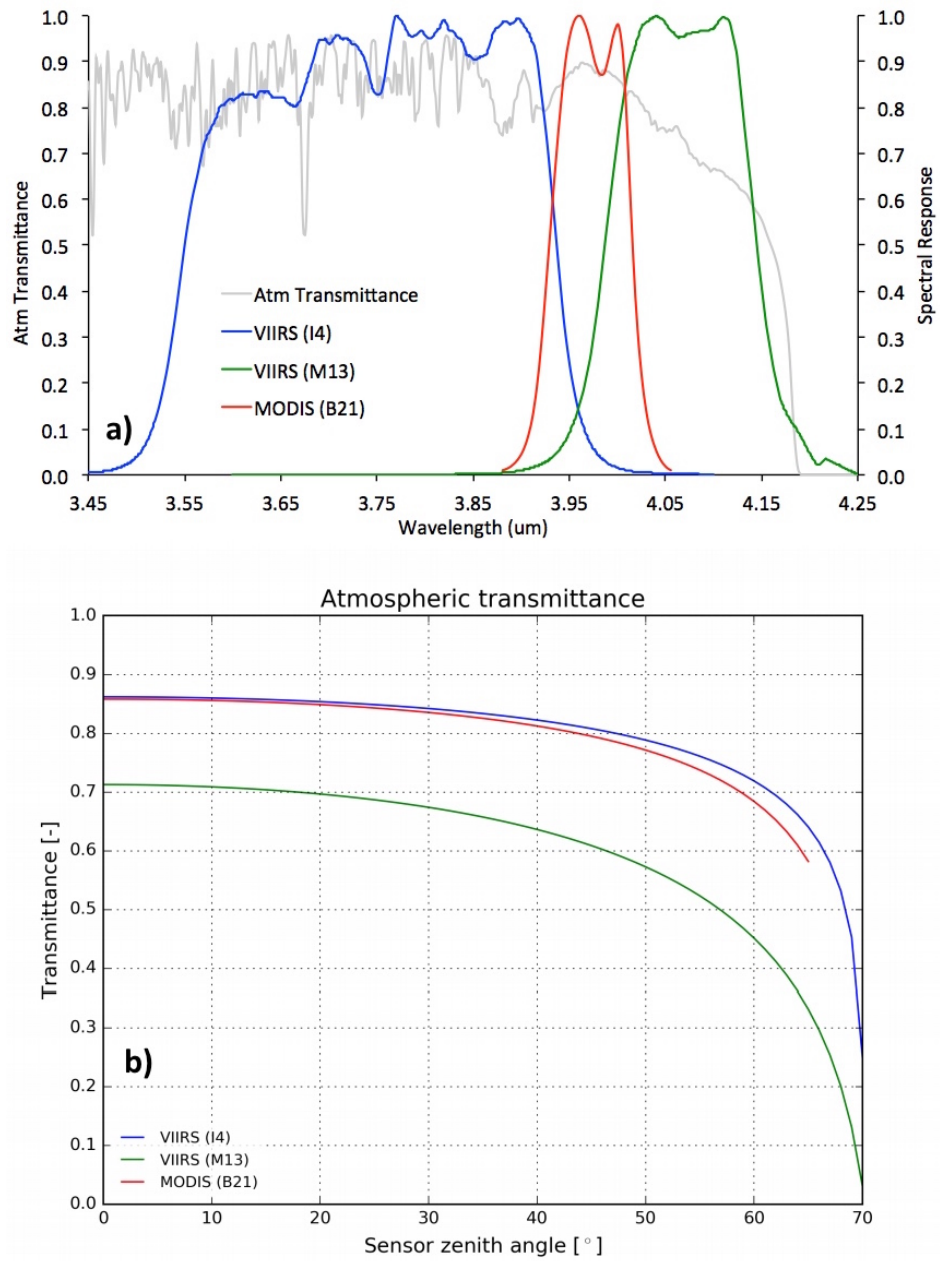


Figure 4.7: Spectral response function and atmospheric transmittance for MIR bands available on VIIRS (I4, M13) and MODIS (B21/B22), according to Schroeder and Giglio (2016). The band placement of the 750 m band M13 leads to much greater atmospheric extinction than for the 375 m band I4 or the equivalent MODIS bands.

4.5 Conclusions

In this work, we compared fire detections from the global VIIRS I-band product with VIFDAHL. VIFDAHL detects approximately 40% more fire pixels than the global product at sensor zenith angles between 20° and 40°, and approximately 10% more fire pixels during mid-day acquisitions.

However, at large sensor zenith angles $>60^\circ$, and to a lesser degree for nighttime detections, the global VIIRS I-band product performed slightly better in the selected case study. For both products, detection sensitivity falls off strongly at the edge of the swath.

Using a prototype VIIRS scene, we demonstrated sub-pixel fire temperature and fractional pixel area retrieval with the MIR band M13 and the TIR band M15, and uncertainty analysis based on the noise in at-sensor brightness temperature data. In future work, it will be important to take into account a complete set of uncertainties, including, but not limited to: error in atmospheric correction, inter-band co-registration error and geolocation error.

This study reveals the need to adjust VIFDAHL for the data acquisition geometry and nighttime detection. Adapting VIFDAHL for very large sensor zenith angles is a great opportunity to improve fire detection in general. The adapted VIFDAHL method will enable us to take better advantage of those VIIRS scenes acquired at large sensor zenith angle.

References

- Abrams, M., D. Pieri, V. Realmuto, and R. Wright (2013). Using EO-1 Hyperion Data as HyspIRI Preparatory Data Sets for Volcanology Applied to Mt Etna, Italy. *IEEE Journal of Selected Topics in Applied Earth Observations and Remote Sensing*, vol. 6, no. 2, pp. 375–385. DOI: 10.1109/JSTARS.2012.2224095.
- Berk, A., G. P. Anderson, P. K. Acharya, L. S. Bernstein, L. Muratov, J. Lee, M. Fox, S. M. Adler-Golden, J. H. Chetwynd, M. L. Hoke, R. B. Lockwood, J. A. Gardner, T. W. Cooley, C. C. Borel, P. E. Lewis, and E. P. Shettle (2006). MODTRAN5: 2006 update. In: Algorithms and Technologies for Multispectral, Hyperspectral, and Ultraspectral Imagery XII. Vol. 6233. International Society for Optics and Photonics, 62331F. DOI: 10.1117/12.665077.
- Boles, S. H. and D. L. Verbyla (1999). Effect of scan angle on AVHRR fire detection accuracy in interior Alaska. *International Journal of Remote Sensing*, vol. 20, no. 17, pp. 3437–3443.
- Briess, K., H. Jahn, E. Lorenz, D. Oertel, W. Skrbek, and B. Zhukov (2003). Fire recognition potential of the bi-spectral Infrared Detection (BIRD) satellite. *International Journal of Remote Sensing*, vol. 24, no. 4, pp. 865–872. DOI: 10.1080/01431160210154010.

Cao, C., F. J. D. Luccia, X. Xiong, R. Wolfe, and F. Weng (2014). Early On-Orbit Performance of the Visible Infrared Imaging Radiometer Suite Onboard the Suomi National Polar-Orbiting Partnership (S-NPP) Satellite. *IEEE Transactions on Geoscience and Remote Sensing*, vol. 52, no. 2, pp. 1142–1156. DOI: 10.1109/TGRS.2013.2247768.

Csiszar, I., W. Schroeder, L. Giglio, E. Ellicott, K. P. Vadrevu, C. O. Justice, and B. Wind (2014). Active fires from the Suomi NPP Visible Infrared Imaging Radiometer Suite: Product status and first evaluation results. *Journal of Geophysical Research: Atmospheres*, vol. 119, no. 2, 2013JD020453. DOI: 10.1002/2013JD020453.

Dennison, P. E., K. Charoensiri, D. A. Roberts, S. H. Peterson, and R. O. Green (2006). Wildfire temperature and land cover modeling using hyperspectral data. *Remote Sensing of Environment*, vol. 100, no. 2, pp. 212–222. DOI: 10.1016/j.rse.2005.10.007.

Dozier, J. (1981). A method for satellite identification of surface temperature fields of subpixel resolution. *Remote Sensing of Environment*, vol. 11, pp. 221–229. DOI: 10.1016/0034-4257(81)90021-3.

Dozier, J. and T. H. Painter (2004). Multispectral and hyperspectral remote sensing of alpine snow properties. *Annual Review of Earth and Planetary Sciences*, vol. 32, no. 1, pp. 465–494. DOI: 10.1146/annurev.earth.32.101802.120404.

Eckmann, T. C., D. A. Roberts, and C. J. Still (2008). Using multiple endmember spectral mixture analysis to retrieve subpixel fire properties from MODIS. *Remote Sensing of Environment*, vol. 112, no. 10, pp. 3773–3783. DOI: 10.1016/j.rse.2008.05.008.

Giglio, L. and C. O. Justice (2003). Effect of wavelength selection on characterization of fire size and temperature. *International Journal of Remote Sensing*, vol. 24, no. 17, pp. 3515–3520. DOI: 10.1080/0143116031000117056.

Giglio, L., J. Descloitres, C. O. Justice, and Y. J. Kaufman (2003). An Enhanced Contextual Fire Detection Algorithm for MODIS. *Remote Sensing of Environment*, vol. 87, no. 2, pp. 273–282. DOI: 10.1016/S0034-4257(03)00184-6.

Giglio, L. and J. D. Kendall (2001). Application of the Dozier retrieval to wildfire characterization: a sensitivity analysis. *Remote Sensing of Environment*, vol. 77, no. 1, pp. 34–49. DOI: 10.1016/S0034-4257(01)00192-4.

Giglio, L. and W. Schroeder (2014). A global feasibility assessment of the bi-spectral fire temperature and area retrieval using MODIS data. *Remote Sensing of Environment*, vol. 152, pp. 166–173. DOI: 10.1016/j.rse.2014.06.010.

Giglio, L., W. Schroeder, and C. O. Justice (2016). The collection 6 MODIS active fire detection algorithm and fire products. *Remote Sensing of Environment*, vol. 178, pp. 31–41. DOI: 10.1016/j.rse.2016.02.054.

Hastings, W. K. (1970). Monte Carlo sampling methods using Markov chains and their applications. *Biometrika*, vol. 57, no. 1, pp. 97–109.

Hillger, D., T. Kopp, C. Seaman, S. Miller, D. Lindsey, E. Stevens, J. Solbrig, W. Straka III, M. Kreller, A. Kuciauskas, and A. Terborg (2015). User Validation of VIIRS Satellite Imagery. *Remote Sensing*, vol. 8, no. 1, p. 11. DOI: 10.3390/rs8010011.

Hillger, D., C. Seaman, C. Liang, S. Miller, D. Lindsey, and T. Kopp (2014). Suomi NPP VIIRS Imagery evaluation. *Journal of Geophysical Research: Atmospheres*, vol. 119, no. 11, 2013JD021170. DOI: 10.1002/2013JD021170.

Kaufman, Y. J., C. O. Justice, L. P. Flynn, J. D. Kendall, E. M. Prins, L. Giglio, D. E. Ward, W. P. Menzel, and A. W. Setzer (1998). Potential global fire monitoring from EOS-MODIS. *Journal of Geophysical Research*, vol. 103, PP. 32, 215–32, 238. DOI: 199810.1029/98JD01644.

Kruschke, J. (2014). *Doing Bayesian Data Analysis, Second Edition: A Tutorial with R, JAGS, and Stan*. 2nd edition. Boston: Academic Press. 776 pp.

Liew, S. C., A. S. Chia, and L. K. Kwoh (2015). Estimating the characteristics of sub-pixel fires using Suomi-NPP VIIRS data. In: *2015 IEEE International Geoscience and Remote Sensing Symposium (IGARSS)*. 2015 IEEE International Geoscience and Remote Sensing Symposium (IGARSS), pp. 2163–2165. DOI: 10.1109/IGARSS.2015.7326232.

Matson, M. and J. Dozier (1981). Identification of subresolution high temperature sources using a thermal IR sensor. *Photogrammetric Engineering and Remote Sensing*, vol. 47, no. 9, pp. 1311–1318.

Metropolis, N., A. W. Rosenbluth, M. N. Rosenbluth, A. H. Teller, and E. Teller (1953). Equation of State Calculations by Fast Computing Machines. *The Journal of Chemical Physics*, vol. 21, no. 6, pp. 1087–1092. DOI: 10.1063/1.1699114.

Peterson, D. and J. Wang (2013). A sub-pixel-based calculation of fire radiative power from MODIS observations: 2. Sensitivity analysis and potential fire weather application. *Remote Sensing of Environment*, vol. 129, pp. 231–249. DOI: 10.1016/j.rse.2012.10.020.

Peterson, D., J. Wang, C. Ichoku, E. Hyer, and V. Ambrosia (2012). A sub-pixel-based calculation of fire radiative power from MODIS observations: 1: Algorithm development and initial assessment. *Remote Sensing of Environment*. DOI: 10.1016/j.rse.2012.10.036.

Prakash, A. and R. P. Gupta (1999). Surface fires in Jharia coalfield, India-their distribution and estimation of area and temperature from TM data. *International Journal of Remote Sensing*, vol. 20, no. 10, pp. 1935–1946. DOI: 10.1080/014311699212281.

Prins, E. M. and W. P. Menzel (1994). Trends in South American biomass burning detected with the GOES visible infrared spin scan radiometer atmospheric sounder from 1983 to 1991. *Journal of Geophysical Research: Atmospheres*, vol. 99, no. D8, pp. 16719–16735. DOI: 10.1029/94JD01208.

Schroeder, W., I. Csiszar, L. Giglio, and C. C. Schmidt (2010). On the use of fire radiative power, area, and temperature estimates to characterize biomass burning via moderate to coarse spatial resolution remote sensing data in the Brazilian Amazon. *Journal of Geophysical Research: Atmospheres*, vol. 115. DOI: 10.1029/2009JD013769.

Schroeder, W. and L. Giglio (2016). *Visible Infrared Imaging Radiometer Suite (VIIRS) 750 m Active Fire Detection and Characterization Algorithm Theoretical Basis Document 1.0*. NASA/Goddard Space Flight Center.

Schroeder, W., P. Oliva, L. Giglio, and I. A. Csiszar (2014). The New VIIRS 375 m active fire detection data product: Algorithm description and initial assessment. *Remote Sensing of Environment*, vol. 143, pp. 85–96. DOI: 10.1016/j.rse.2013.12.008.

Schroeder, W., E. Prins, L. Giglio, I. Csiszar, C. Schmidt, J. Morisette, and D. Morton (2008). Validation of GOES and MODIS active fire detection products using ASTER and ETM+ data. *Remote Sensing of Environment*, vol. 112, no. 5, pp. 2711–2726. DOI: 10.1016/j.rse.2008.01.005.

Tarantola, A. (2005). *Inverse Problem Theory and Methods for Model Parameter Estimation*. Other Titles in Applied Mathematics. DOI: 10.1137/1.9780898717921. Society for Industrial and Applied Mathematics. 348 pp.

Waigl, C. F., M. Stuefer, A. Prakash, and C. Ichoku (2017). Detecting high and low-intensity fires in Alaska using VIIRS I-band data: An improved operational approach for high latitudes. *Remote Sensing of Environment*, vol. 199, pp. 389–400. DOI: 10.1016/j.rse.2017.07.003.

Chapter 5

GENERAL CONCLUSION

We have demonstrated that improvements to the detection of low-intensity fires and fire temperature retrieval for Alaska's boreal forest fire are achievable by analyzing spectral radiance data from satellite-based infrared remote sensing. In high latitude regions, sensors such as MODIS or VIIRS on polar-orbiting satellites, with spatial resolutions that vary between several 100 m and several km, acquire new imagery of any location of interest multiple times per day. During cloud-free periods, these images serve as a good data source for monitoring forest fires. Existing global active fire products have obvious advantages such as product stability and the availability of long-term consistent datasets, which cannot be easily matched by algorithms tuned to the conditions found in a small region of the globe. However, regionally adapted algorithms have the benefit of taking into account the specific local conditions and therefore can be superior for meeting particular fire detection and monitoring needs. This is evidenced by the VIIRS I-band Fire Detection Algorithm for High Latitude (VIFDAHL), which we developed based on the 375 m imaging bands of VIIRS on Suomi-NPP: We used near-simultaneous higher-resolution imagery from Landsat to show that VIFDAHL offers better detection and mapping of low-intensity boreal forest fires in Alaska compared to the global product.

A better understanding of low-intensity fires opens up numerous avenues both for fire management applications and scientific research. Low-intensity residual fires can persist for a long time in the soil and cause fire re-starts under favorable weather conditions; moreover, weak signals from low-intensity fires can indicate early fire starts and therefore make it possible to detect new fires earlier. Fire managers are therefore interested in timely maps of such detections. Data transfer across the internet, at several gigabytes per dataset, is still to this day a factor that introduces delays and the risk of data loss. Near real-time applications thus highlight the advantage of using locally downlinked data from direct-readout systems such as the downlink station oper-

ated by the Geographic Information Network of Alaska (GINA) at UAF, and optionally processing them using a regionally adapted algorithm.

We also analyzed the performance of existing global active fire products in the context of wildfires in Alaska. For real-time applications like fire monitoring, the user community benefits from understanding at what times of the day new data will most likely be available, and how detections are distributed across a management area such as the state of Alaska. The properties of near real-time fire detection products depend largely on orbital parameters, sensor geometry (swath width) and the number of sensors in operational use. Thus, even though VIIRS-based fire detections are more numerous than MODIS detections by approximately a factor of 3, they are clustered in narrower temporal bands around the early afternoon and early morning hours. MODIS detections are distributed more widely across the day because they are generated by two sensors on complementary orbits. The use of VIIRS data also requires excluding volcanic and industrial sources of high-temperature signals.

The effectiveness of both the global VIIRS I-band (375 m) product and VIFDAHL has a dependency on the sensor zenith angle at which data is acquired. The VIIRS swath is approximately 3040 km wide; therefore, zenith angles $>60^\circ$ are common. That far off-nadir, the pixel footprint is much larger and the atmospheric path length is increased compared to the nadir view. We found that the detection likelihood falls off at angles $>50^\circ$ for both the global VIIRS I-band (375 m) product and VIFDAHL, with a sharper decrease for VIFDAHL. On the other hand, VIFDAHL performs better at angles $<40^\circ$ where the bulk of the fire pixels are detected.

VIFDAHL offers a promising product, suited to generating input data for fire spread models and smoke dispersion forecasting. It can also be used for the early detection of “hold-over” fires that reside in the sub-surface layer throughout the winter, and to monitor nearly-extinguished fires that pose a risk of re-starting large-scale burns. The next version of VIFDAHL should incorporate a correction factor for sensor zenith angle and potentially improved nighttime detection.

In ~ 1 km resolution imagery, active fire is bound to occupy only a small portion of a pixel’s footprint. The investigation of fire properties therefore needs to operate at the sub-pixel level. We

showed that the method pioneered by Dozier (1981) and Matson and Dozier (1981) for AVHRR data extends to VIIRS scenes acquired over Alaskan boreal forest fires. Sub-pixel temperature retrieval in MODIS and similar data sets requires careful attention to uncertainty. We found that the VIIRS detection limits are similar to those described by Giglio and Kendall (2001) for MODIS, especially at small partial pixel areas. We used a Monte Carlo method to estimate uncertainties in model parameters and applied it to a prototype problem under simplified assumptions about data uncertainties. The method can be generalized to other known sources of error.

In hyperspectral data, the large number of spectral bands makes it possible to determine fire temperatures as well as the fractional pixel areas occupied by fire and background components. Using archived Hyperion scenes acquired over Alaska wildfires from 2004 and 2009, we fitted a spectral mixture model to the SWIR spectra acquired by the sensor and were able to achieve an excellent correspondence between measured spectra and a model consisting of fire scar background, unburned vegetation background, and two active fire components. Typically, we found one component at a lower temperature within the smoldering range (~500 K to 600 K), and one within the flaming range (~800 K to 900 K). The retrieved flaming fire temperatures are here limited by sensor saturation and represent a lower bound on realistic actual flame temperatures.

We examined fire detection in imaging spectroscopy and found that a modified and band-averaged version of the Hyperspectral Fire Detection Index is a reliable detection metric that is well-suited for boreal forest fires. A carbon dioxide Continuum Interpolated Band Ratio index was sensitive to fire but quite strongly affected by noise and smoke. The signal from a potassium emission feature was just barely discernible in a small part of one out of three sample scenes, but as far as fire detection is concerned, is more promising for airborne or in-situ measurements rather than satellite-based remote sensing.

To take a broader view of fire remote sensing in boreal Alaska, we note that the contribution of low-intensity residual fire to carbon consumption and fire emissions from the organic surface layers in the boreal forest is currently not well characterized. For black spruce forests common in Alaska, fire severity is represented by the percentage of organic sub-surface layers consumed in a fire event (Lentile et al. 2006). We believe that fire severity could be explored using VIFDAHL

to estimate fire residence times in the surface layers. Alternatively, direct observation of post-fire soil conditions with hyperspectral remote sensing would be a promising direction for new research. Both approaches should include validation with field data.

Related methods also apply to other high-temperature phenomena that occur in the region, such as coal seam fires, tundra fires, or volcanic eruptions. In the Appendix, we explored the topic of coal seam fire hazard mapping: the detection of locations that exhibit persistent thermal anomalies in a time series of Landsat images. The study took place in the coal-bearing area of Healy, AK. We successfully correlated these thermal anomalies with known locations of historical or recurring coal seam fires.

Future work would be facilitated if a larger number of VIIRS or MODIS-type sensors in complementary polar orbits were made available. Additionally, imaging spectrometers designed with lower signal-to-noise ratio than Hyperion, a better characterized saturation behavior and a usable spectral range that extends at least throughout the whole SWIR region would undoubtedly enable research to deepen our understanding of the processes that characterize boreal forest fires.

References

- Dozier, J. (1981). A method for satellite identification of surface temperature fields of subpixel resolution. *Remote Sensing of Environment*, vol. 11, pp. 221–229. DOI: 10.1016/0034-4257(81)90021-3.
- Giglio, L. and J. D. Kendall (2001). Application of the Dozier retrieval to wildfire characterization: a sensitivity analysis. *Remote Sensing of Environment*, vol. 77, no. 1, pp. 34–49. DOI: 10.1016/S0034-4257(01)00192-4.
- Lentile, L. B., Z. A. Holden, A. M. S. Smith, M. J. Falkowski, A. T. Hudak, P. Morgan, S. A. Lewis, P. E. Gessler, and N. C. Benson (2006). Remote sensing techniques to assess active fire characteristics and post-fire effects. *International Journal of Wildland Fire*, vol. 15, no. 3. 00293, pp. 319–345. DOI: 10.1071/WF05097.
- Matson, M. and J. Dozier (1981). Identification of subresolution high temperature sources using a thermal IR sensor. *Photogrammetric Engineering and Remote Sensing*, vol. 47, no. 9, pp. 1311–1318.

Appendix A

COAL-FIRE HAZARD MAPPING IN HIGH-LATITUDE COAL BASINS: A CASE STUDY FROM INTERIOR ALASKA¹



Figure A.1: Remote Rugged Winter Landscape: Typical of Many High-Latitude Regions. Photo Credit: National Park Service/Ed Christensen, 2012, Unpublished.

¹Published as a book chapter: Waigl, C. F., Prakash, A., Ferguson, A., & Stuefer, M. (2015). Chapter 24 - Coal-Fire Hazard Mapping in High-Latitude Coal Basins: A Case Study from Interior Alaska. In E. V. Sokol, G. B. Stracher, & A. Prakash (Eds.), Coal and Peat Fires: a Global Perspective (Vol. 3, pp. 633–649). Boston: Elsevier. <http://dx.doi.org/10.1016/B978-0-444-59509-6.00024-7>

A.1 High latitude coal fires

A.1.1 *Introduction*

Coal fires are a common occurrence in most coal bearing areas of the world, as is well documented by Stracher et al. (2010; 2012; 2015). Much has been published about coal fires in active and abandoned coal mines (e.g. Kim 2007; Prakash et al. 1999; Prakash and Gupta 1999; Prakash et al. 1997; Prakash et al. 2013; Stracher et al. 2009). The most intensively studied coal fires are those that occur in tropical and temperate latitudes (Engle et al. 2011; Gupta and Prakash 1998; Kuenzer et al. 2012; Prakash and Gens 2011). Relatively little is known about coal fires that occur in the vast unexplored **high-latitude regions** of the world (Hudspith et al. 2012; Prakash et al. 2011). It is difficult to imagine that these regions, many of which have sub-zero temperatures for well over six months a year, could have repeated occurrences of coal fires.

Some coal fires can start from mining related activities or accidents, such as from frictional heat from machines, short circuiting, mining-induced subsidence, human negligence, or contact of hot mining debris with coal outcrops (Prakash 2014; Stracher et al. 2009). These causes are common in mining areas and are not constrained by latitude. **Spontaneous combustion, forest fires, and lightning strikes** are other common natural causes of coal fires. Of the latter, forest fires and lightning strikes are not uncommon in high latitudes, especially in the drier regions (Dissing and Verbyla 2003; Fauria and Johnson 2008). The phenomena of local heating and spontaneous combustion warrant further discussion in the context of geographic location and geomorphological setting of coal-rich areas.

Higher latitude areas generally witness low sun angles or **solar elevation angles** (solar elevation angle at a particular point on the Earth is defined by the angle subtended by the tangent to the Earth at that point and a straight line between that point and the center of the Sun (Figure A.2a). Consequently they receive low **insolation** or incoming solar irradiation, causing only a gradual warming of the Earth's surface. However, during the summer months, the higher latitude regions have extended daylight hours (Figure A.2b). The night-time is short (and for some time non-existent above 66.5 degrees) making it difficult for the Earth to cool down. In rugged and

mountainous terrains, the south facing slopes particularly receive and retain more heat, raising the general land surface temperature (LST) on these slopes. Coal outcrops and surface carbonaceous materials present on such south facing slopes easily warm up, increasing their chance to catch fire by spontaneous combustion.

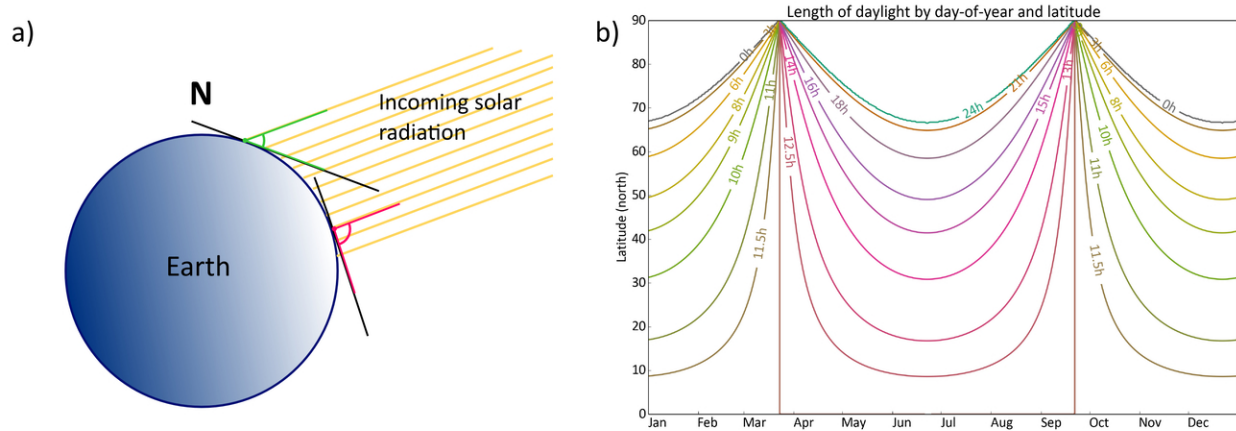


Figure A.2: This representation shows the Earth in relation to the incoming solar radiation during summer in the northern hemisphere. a. High latitude areas generally have lower solar elevation angles (green) compared to the lower latitudes (compare with the large red angle). b. Seasonal variation in daylight hours in the northern hemisphere. On summer solstice, there is one day with 24 hours daylight at 66.5 degrees latitude. The daylight hours continue to increase with an increase in latitude.

Much of the northern high-latitude regions are vegetated, being covered by tundra or by boreal forests. Once a coal fire starts in such landscapes, it becomes a source for forest fires (Prakash et al. 2011; Whitehouse and Mulyana 2004). Forest fires, even after they are put-out, leave burn scars that have remanent heat (Figure A.3). A following cold winter season may not be enough to bring down the LST to ambient temperatures, making the carbonaceous material in the fire scar areas more prone to re-ignition, a phenomenon that we also document with the following case study (Section A.2).

A.1.2 Alaskan Context

Alaska is the only high-latitude state within the United States of America, and it has vast reserves of coal (Figure A.4). Estimates from (Flores et al. 2004) place the combined measured, indicated, inferred, and hypothetical coal resources in three major provinces of the State at over



Figure A.3: Burn pattern typical for wildfire in an Alaskan boreal forest, dominated by black spruce. This photograph is of the 2013 Stuart Creek 2 fire east of Fairbanks, Alaska. The hillside in the foreground is approximately 2 km wide. This and other photographs of the Stuart Creek 2 fire can be viewed at the Incident Information System Website (InciWeb, 2013). Photo credit: Bureau of Land Management, 2013.

5,000 billion metric ton, which exceeds the total coal resources of the rest of the contiguous US states by 40 percent.

Alaska is vast and poorly mapped. Over 80 percent of the geological maps available for the State are at best 1:250,000 scale, and about 16 percent of these are based on mapping efforts prior to 1957 (Newberry 2013, personal communication). A good spatial coverage of large scale maps showing locations of coal outcrops and surface deposits of carbonaceous materials just does not exist. The sparse transportation network within the State (Figure A.5) makes it uneconomical to mine many of the known coal reserves.

Coal and other carbonaceous material remain exposed on the surface, vulnerable to catching fire, across the vast State (Figure A.6). Delineating these **coal fire hazard** areas is important to both commercial mining operators and public agencies charged with wildfire management and suppression, who in Alaska cooperate via the Alaska Interagency Coordination Center (2014). **Remote sensing** offers the only feasible way to map these exposures and delineate coal fire hazard areas.

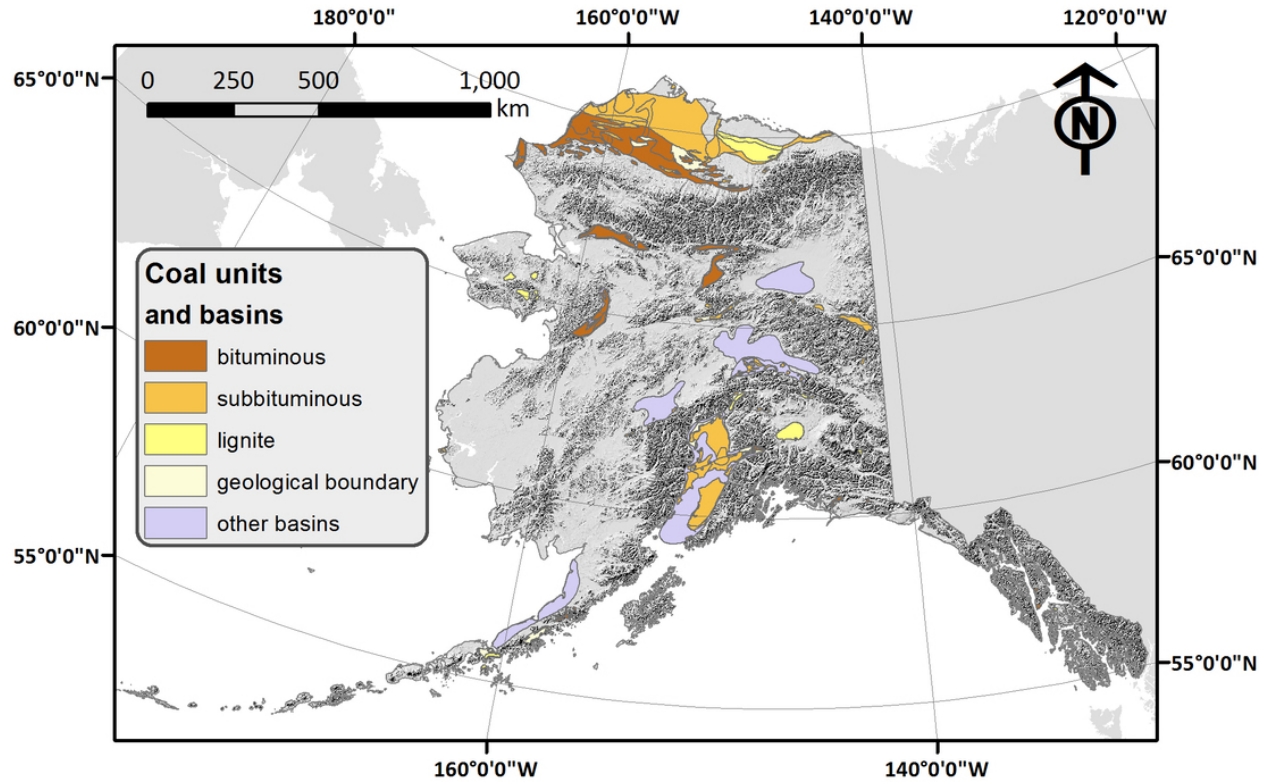


Figure A.4: Map of Alaska showing the major coal basins and coal deposits by rank (where known). The grey background is a shaded relief image where high elevation areas appear in darker grey tones. Map generated by Christine Waigl using data available from Alaska Department of Natural Resources, this work.

A.2 Case Study from Interior Alaska

A.2.1 *Introduction*

The remote sensing based approach to coal fire hazard mapping is based on the hypothesis that some areas persistently show slightly elevated temperatures (**thermal anomalies**) over time (Kuenzer et al. 2007; Raju et al. 2013; Zhang et al. 2004). Should such high temperature areas overlap or closely border on coal seams, coal rubble, or other surface deposits of combustible carbon-rich materials, then there is an increased likelihood of coal fires starting through spontaneous combustion. Such areas should be mapped as hazardous areas, not only for coal fires but also for related forest fires, and should be made a target for frequent monitoring during the fire seasons. As remote sensing provides a synoptic overview of large areas, such hazard mapping can be undertaken even for areas that are otherwise inaccessible and not well-mapped in the past (Prakash and Vekerdy 2004).

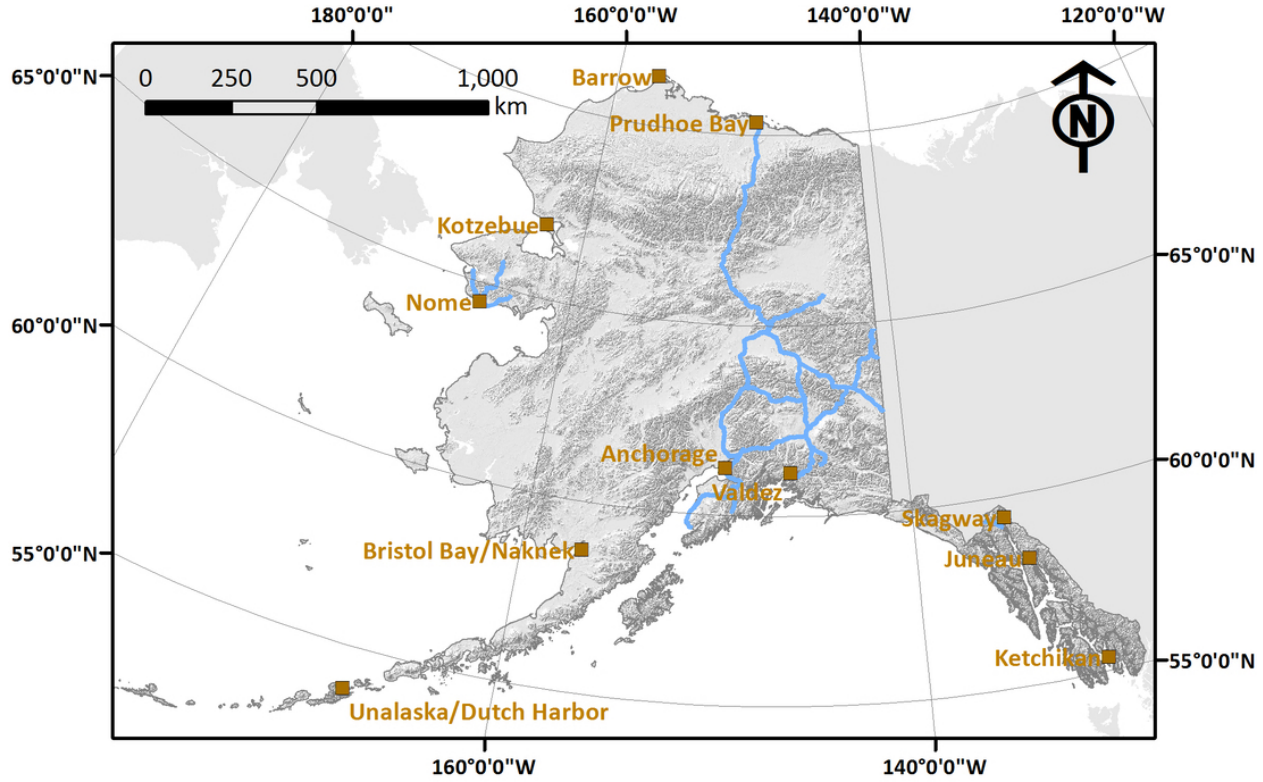


Figure A.5: Map of Alaska showing the major coal basins and coal deposit by rank (where known). The grey background is a shaded relief image where high elevation areas appear in darker grey tones. Map generated using data available from Alaska Department of Natural Resources.

The case study presented here is from a region in the dry boreal forests of interior Alaska, within the central part of the **Nenana coal basin**, which is one of the three large coal basins in the State of Alaska. Freely available Landsat satellite images acquired over a period of multiple years have been processed to generate a coal fire hazard map, following a largely automated work-flow that can form the basis for an operational protocol for large area hazard mapping in high-latitudes, or in other cold-temperature regions such as the high-altitude coal fire prone areas in China and Mongolia.

A.2.2 Study Area

The selected study area (Figure A.7) extends in latitude from 64.238°N to 63.795°N (~50km north-south), and in longitude from 149.224°W to 147.810°W (~70 km west-east). Several coalfields (cream-colored polygons in Figure A.7) lie within the Nenana coal basin that covers large parts of the area under investigation. Usibelli Coal Mine Inc., the only active coal mine in the State,



Figure A.6: A field photograph of the 2012 Windfall Mountain fire, east of the case study area. Carbonaceous material (oil shale) is seen burning even in deep winter when the landscape is snow covered. Spruce trees in this area are typically 6 – 10m tall. Several spruce trees burned during a previous fire. Burned and fallen trees are visible on the snow-covered slopes in the fore-ground. The diagonal brown burn scar is approximately 300m long. This and other photographs of the Windfall Mountain fire are available on the National Park Service (NPS) photo gallery website (NPS 2012). Photo Credit: National Park Service / Ed Christensen, 2012.

is based in Healy and lies in the western part of the study area. One highway running north-south through the town of Healy, and a few unpaved private roads are the only transportation infrastructure available.

The terrain is generally rugged with mountainous areas ranging in elevation from approximately 500m to 1400m. The principal land cover is boreal forests with a predominance of **black spruce** (*Picea mariana*). The boreal forests in interior Alaska experience frequent **wildfires** with large variation between low and extreme fire years, burning at an average nearly 4000 km² of forest area a year (Wendler et al. 2010). Wildfire is the predominant mechanism for renewal of forest

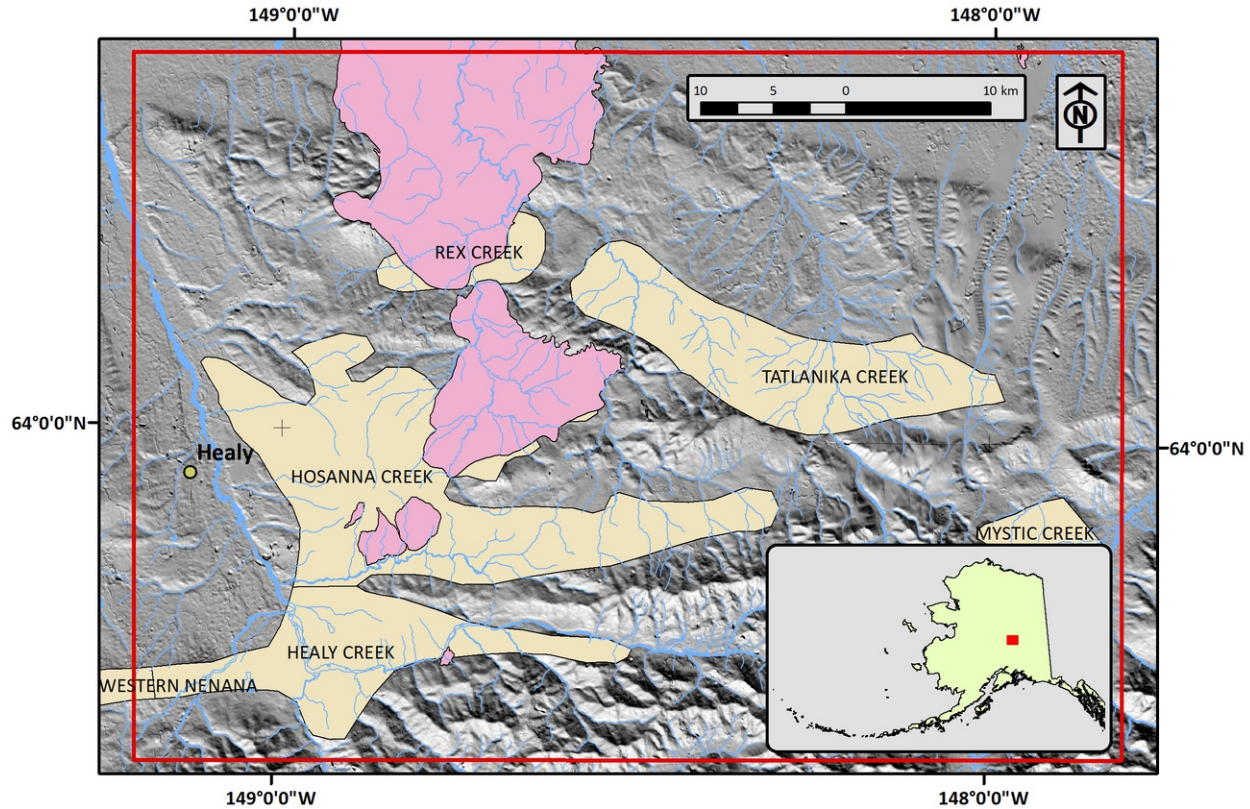


Figure A.7: This map shows the extent of the study area (red rectangle) and its location within interior Alaska (inset), as well as relief and hydrology of the area. The coal mining town of Healy is located in the western part of the study area near the banks of the Nenana River. Coal fields within the Nenana coal basin are shown in beige, and the expanse of the 2009 to 2011 wildfires are shown in pink.

stands in black spruce dominated boreal forests, with a fire recurrence interval of approximately 50 to 150 years (Chapin et al. 2006; Kasischke et al. 2002).

A.2.3 Data

The study is based on a wealth of data sets including many satellite images, **digital elevation model** and its derivative products, **geographic information system** (GIS) compatible vector data, and limited field observations.

40 royalty-free summer-time satellite images, acquired between 2006 and 2013 by the Landsat series of satellites, were selected and downloaded from the USGS Earth Explorer web portal (2014) and formed the main database for this study. This dataset excluded any image that had over 40% cloud cover, complete or near-complete snow cover, or extensive signature of smoke from

wildfires. All the images were in the Universal Transverse Mercator (UTM) Zone 6N coordinate reference system. Table A.1 summarizes the Landsat scene identification number, the respective Landsat platform from which the image was acquired, the date of image acquisition, and the native spatial resolution of the **thermal infrared (TIR)** image/band used for thermal anomaly detection.

On average, five suitable Landsat scenes per year were available for the study. The Thematic Mapper (TM), Enhanced Thematic Mapper (ETM+), and Operational Land Imager/Thermal Infrared Scanner (OLI/TIRS) sensors available of Landsat 5, Landsat 7, and Landsat 8, respectively scan the earth in the visible, near infrared, shortwave infrared and TIR wavelengths (USGS 2012). While the visible through shortwave infrared bands have been used to classify the general land cover and mask-out the cloud/snow areas, the TIR bands form the main data source for fire hazard detection. The TIR sensors used in this study are Landsat 5 TM band 6 (10.40-12.50 μm ; 120m spatial resolution), high-gain dataset from Landsat 7 ETM+ (10.40-12.50 μm ; 60m spatial resolution), and Landsat 10 TIRS band 10 (10.60 - 11.19 μm ; 100m spatial resolution) (see Table A.1). All TIR images are resampled to 30m pixel-size by the data-provider, and data processing has followed at this pixel size.

Six ASTER DEM tiles at a 1 arc second resolution, each spanning 1 by 1 degree of latitude/longitude were downloaded from Alaska Mapped (2014) that is run by the Geographic Information Network of Alaska (GINA 2014), mosaicked, reprojected to UTM zone 6N, resampled to 30m pixel size, and clipped to the extents of the study area, to have a perfect overlap with the Landsat images. Slope, aspect, and gradient images, standard derivative products from digital elevation models, were generated and used as further input data to provide a geomorphological context to thermal anomaly detection and fire hazard mapping. For this study all pixels were forced to classify into north or south facing slopes, with zero slope pixels (flat areas) being combined with the south facing slopes.

Vector files included point data for port and city locations (GNIS 2013), line data for transportation network, coastlines, boundaries and hydrology (ASGDC 2014; Global Administrative Areas 2014; GNIS 2013) and polygon data for coal basins and coal fields (Merritt and Hawley

Table A.1: List of 40 Landsat scenes used to retrieve persistent thermal anomalies. Data available from the U.S. Geological Survey. The scenes were downloaded from the USGS EarthExplorer web portal (<http://earthexplorer.usgs.gov/>).

Landsat scene ID	Date	Satellite	Original spatial resolution of TIR band (resampled to 30 m)
LE70690152006206EDC02	2006-07-25	Landsat 7	60 m
LT50690152006246PAC01	2006-09-03	Landsat 5	120 m
LT50690152006262PAC01	2006-09-19	Landsat 5	120 m
LE70690152006286EDC00	2006-10-13	Landsat 7	60 m
LE70690152007145EDC00	2007-05-25	Landsat 7	60 m
LE70690152007209EDC00	2007-07-28	Landsat 7	60 m
LE70690152008132EDC00	2008-05-11	Landsat 7	60 m
LT50690152008172GLC00	2008-06-20	Landsat 5	120 m
LT50690152008236GLC00	2008-08-23	Landsat 5	120 m
LE70690152008244EDC00	2008-08-31	Landsat 7	60 m
LE70690152009134EDC00	2009-05-14	Landsat 7	60 m
LE70690152009166EDC00	2009-06-15	Landsat 7	60 m
LE70690152009182EDC00	2009-07-01	Landsat 7	60 m
LT50700152009197GLC00	2009-07-16	Landsat 5	120 m
LE70690152009198EDC00	2009-07-17	Landsat 7	60 m
LT50700152009229GLC00	2009-08-17	Landsat 5	120 m
LE70690152009246EDC00	2009-09-03	Landsat 7	60 m
LE70700152009285EDC00	2009-10-12	Landsat 7	60 m
LE70700152010256EDC00	2010-09-13	Landsat 7	60 m
LT50690152010257GLC00	2010-09-14	Landsat 5	120 m
LE70690152010265EDC00	2010-09-22	Landsat 7	60 m
LT50690152011132GLC00	2011-05-12	Landsat 5	120 m
LE70700152011147EDC00	2011-05-27	Landsat 7	60 m
LT50700152011187GLC00	2011-07-06	Landsat 5	120 m

Table A.1 continued.

Landsat scene ID	Date	Satellite	Original spatial resolution of TIR band (resampled to 30 m)
LE70690152012175EDC00	2012-06-23	Landsat 7	60 m
LE70690152012191EDC00	2012-07-09	Landsat 7	60 m
LE70690152012207EDC00	2012-07-25	Landsat 7	60 m
LE70690152012223EDC00	2012-08-10	Landsat 7	60 m
LC80700152013144LGN00	2013-05-24	Landsat 8	100 m
LC80680152013146LGN00	2013-05-26	Landsat 8	100 m
LC80690152013153LGN00	2013-06-02	Landsat 8	100 m
LC80700152013160LGN00	2013-06-09	Landsat 8	100 m
LC80680152013162LGN00	2013-06-11	Landsat 8	100 m
LC80690152013169LGN00	2013-06-18	Landsat 8	100 m
LC80700152013176LGN00	2013-06-25	Landsat 8	100 m
LC80690152013185LGN00	2013-07-04	Landsat 8	100 m
LC80680152013194LGN00	2013-07-13	Landsat 8	100 m
LC80700152013224LGN00	2013-08-12	Landsat 8	100 m
LC80690152013233LGN00	2013-08-21	Landsat 8	100 m
LC80680152013258LGN00	2013-09-15	Landsat 8	100 m

1986). Additionally, wildfire start point and burn area perimeter information was retrieved from the Alaska Interagency Coordination Center (AICC, 2014). Limited sightings of coal fire and forest fire locations were made by authors Waigl and Stuefer via overflights in summer 2013, and also by colleagues from the National Park Service.

A.2.4 Data Processing

The purpose of the data processing was to identify persistent thermal anomalies in coal-rich regions, and map them as proxies for coal fire hazards. The two-step process to achieve this included: (i) thermal anomaly detection on an individual Landsat scene and (ii) persistent anomaly

detection from a stack of processed images. Data processing was carried out using a combination of command-line tools provided in the Geospatial Data Abstraction Library (GDAL Development Team 2011) and custom-made scripts written by Waigl in Python using the Numpy, Scipy and scikit-learn libraries (Oliphant 2007; Pedregosa et al. 2011). The coal fire hazard locations were displayed on satellite images and the final maps were generated using open-source and commercial GIS software packages such as QGIS and ArcGIS.

A.2.4.1 *Thermal anomaly detection on an individual Landsat scene*

Using the Landsat 7 image acquired on May 27, 2011 as an example, the data processing flow for thermal anomaly detection on an individual image is further explained.

As a first step the Landsat image was clipped to match the study area extents and the TIR bands were extracted and processed to retrieve temperature values. The rationale for temperature estimation as a first step in the processing chain was to be able to compare the results of temperature statistics derived from the entire image scene with the temperature statistics from a scene where obvious confounding error pixels were already removed, as discussed later in this section. The digital numbers of the TIR bands were converted first to radiance and then to at-satellite **radiant temperatures** measured in Kelvin as described in (Chander et al. 2009). As the purpose of this study was not to derive accurate ground-surface temperatures (kinetic temperatures as measured by a contact thermometer), but to detect areas that were relatively warmer than the surrounding areas with similar landcover, further analysis was carried out using at-satellite radiant temperatures as proxy for the LST.

Satellite images record response from several features such as clouds, shadow, snow/ice, active fires and fire scars, and also from malfunctioning of the detectors themselves that impede the identification of thermal anomalies (Figure A.8). Pixels that included signal from clouds and active fire needed to be masked out to ensure that the digital values from such pixels did not distort the overall image statistics for further analysis. Similarly, image pixels dominated by snow/ice were removed from processing. The location of multi-year fire scars is of interest for relating results to landscape surface features and burn history.

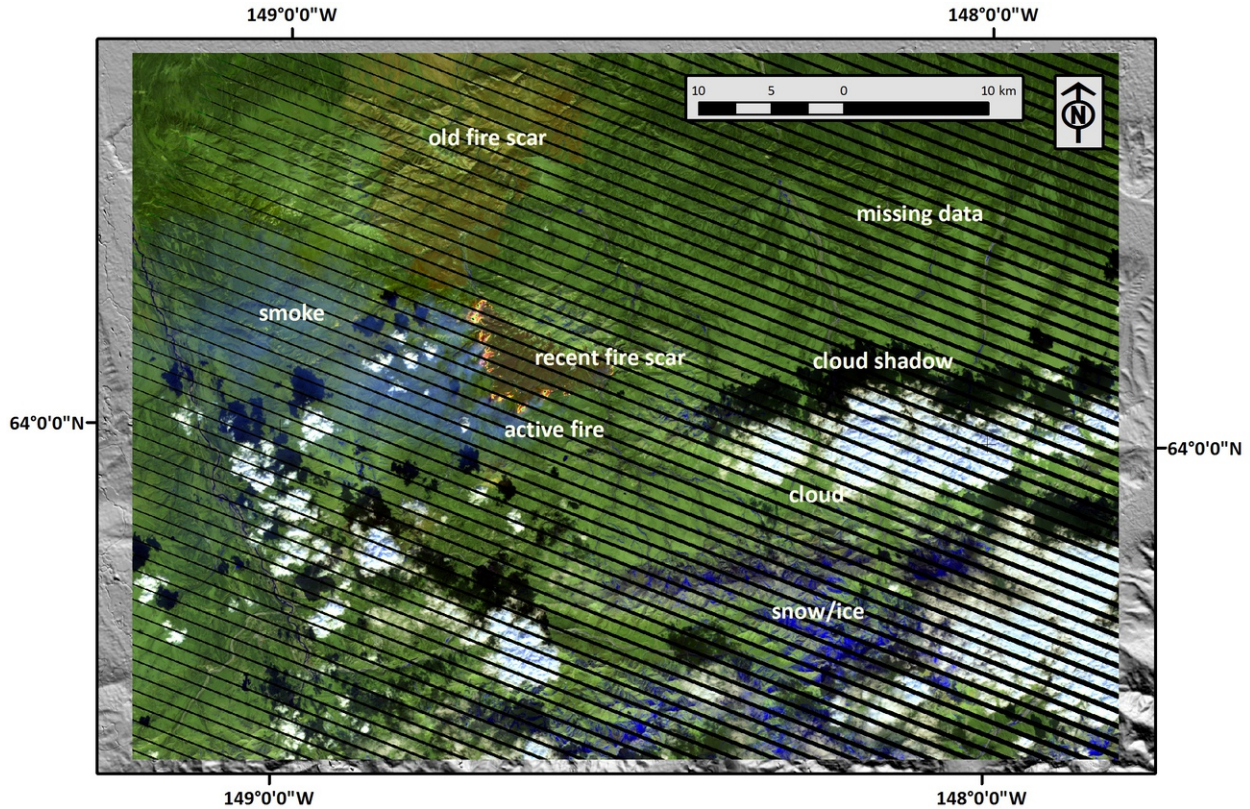


Figure A.8: A subset of the selected 2011 Landsat image covering the study area. The image is a false color composite (FCC) generated by displaying the shortwave infrared band in red, the near infrared band in green, and the red band in blue. On this FCC healthy vegetation appears green and ice appears bright blue. Many features pose a problem for coal fire hazard mapping. These include flaming fire (bright yellow and red points), fires scars (shades of brown), clouds (white), shadows (dark patches close the white clouds), smoke (semi-transparent light blue region) and missing data (black diagonal stripes) that are clearly visible on this image.

To proceed with the **masking**, a four band stack of visible, near infrared, and shortwave infrared images was classified using an LTK algorithm (Oreopoulos et al. 2011) into bare soil, water, ice, cloud, vegetated ground, and no data classes (Figure A.9). Using this algorithm smoke from the wild fires misclassified as clouds. This misclassification was advantageous. Clouds, smoke and no data pixels could all be masked out from subsequent processing based on the LTK classification results. Furthermore, some shadow and cold bare soil surfaces were misclassified as water, but not reliably enough to use this class to remove them. Thermal anomalies located in cloud shadow areas would be unlikely to be identified in single scene, though for the identification of persistent anomalies via an image stacking approach, transient cloud shadows are not expected to introduce gross distortions.

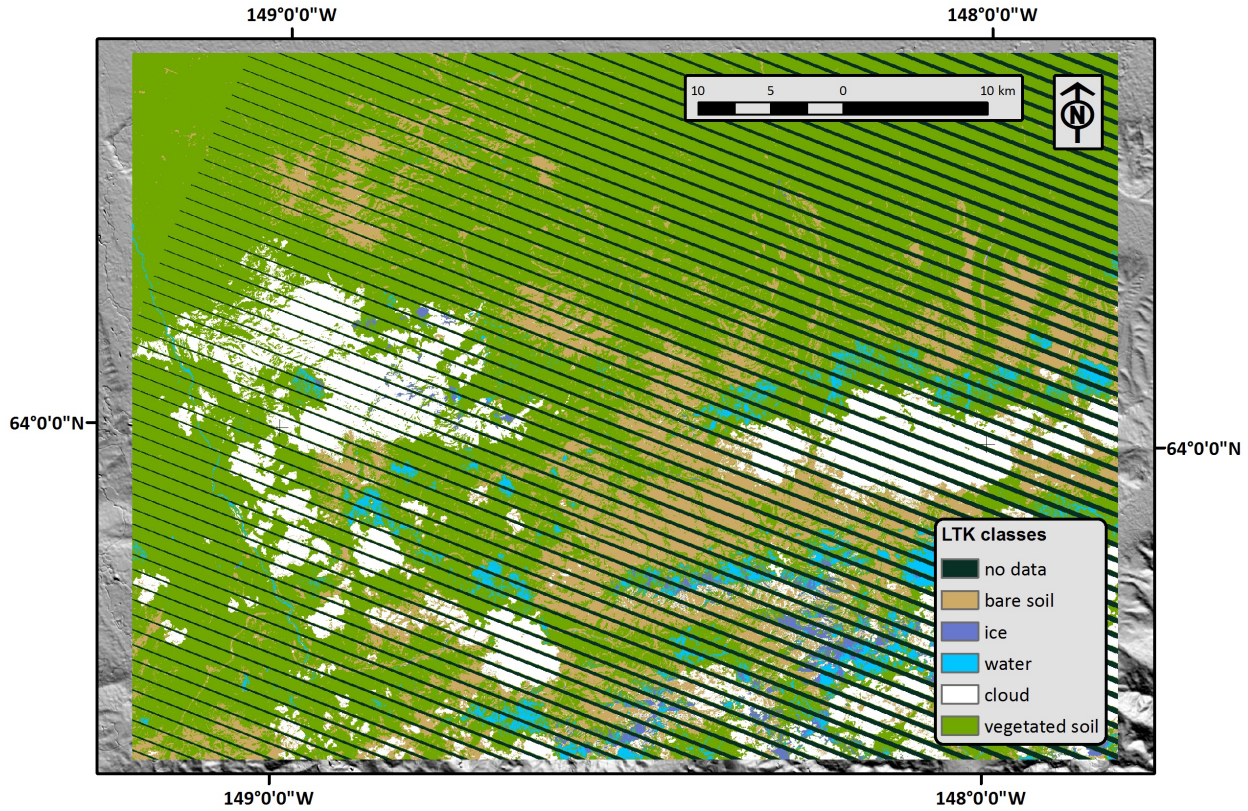


Figure A.9: Result of classifying the selected 2011 Landsat image using the LTK algorithm. This product produces a very suitable mask for cloud and smoke.

Active fires and freshly burnt ground was masked using a threshold of -0.4 on a Normalized Burn Ratio image. This widely used index (Key and Benson 2006) makes use of the fact that active fires and charcoal return a strong signal in the shortwave infrared but a comparatively weak one in the near infrared spectral region. (Figure A.10) shows a fully masked version of the example Landsat image.

Next, the statistics of the derived radiant temperature distribution were plotted as a **histogram**, with the radiant temperatures on the x-axis and the probability distribution function on the y-axis (Figure A.11). For a complete and systematic analysis, four separate histograms were generated that showed the radiant temperature statistics for (a) the entire scene (all valid data), (b) the entire scene after complete masking, (c) only north-facing pixels of the masked scene, and (d) only south-facing pixels of the masked scene. The resulting distributions were poorly approximated by normal distributions (blue curve). However, a Gaussian mixture model combining two independent normal distributions (green curve) led to an excellent fit. This was

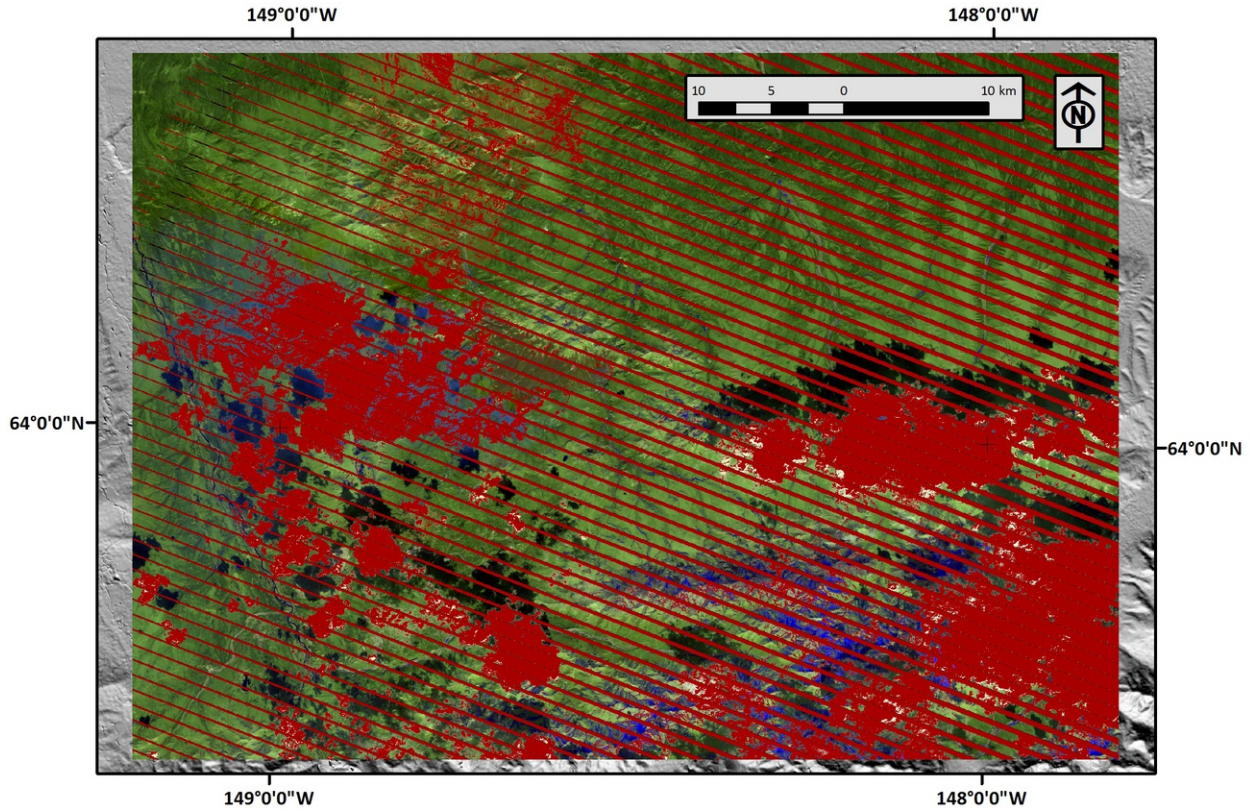


Figure A.10: Selected 2011 Landsat image after masking out clouds, smoke, active fires, fresh burn scars, and missing data pixels. Cloud shadow is not masked out, but its impact is minimized by the averaging influence of the image stacking step in the processing chain.

the case for all 40 scenes of the study set. Pixels were identified as thermally anomalous (hotspots) if their radiant temperature was more than 4 standard deviations above the mode of the dominant normal distribution (T_1 in Figure A.11). Positive thermal anomalies were identified and extracted separately for both north facing and south facing slopes.

A.2.4.2 Persistent anomaly detection from a stack of processed images

All 40 image scenes were processed separately following the steps outlined in the previous section. To declare a thermally anomalous pixel as persistent, it would have to be tracked on multiple date images acquired over a period of time. Therefore, all processed image scenes were stacked and an **anomaly occurrence index** was calculated for each anomalous pixel. The index only took into consideration statistics if the pixel had valid data that was not masked out. For example, an anomaly occurrence index of 0.5 meant that the pixel in question was anomalous in

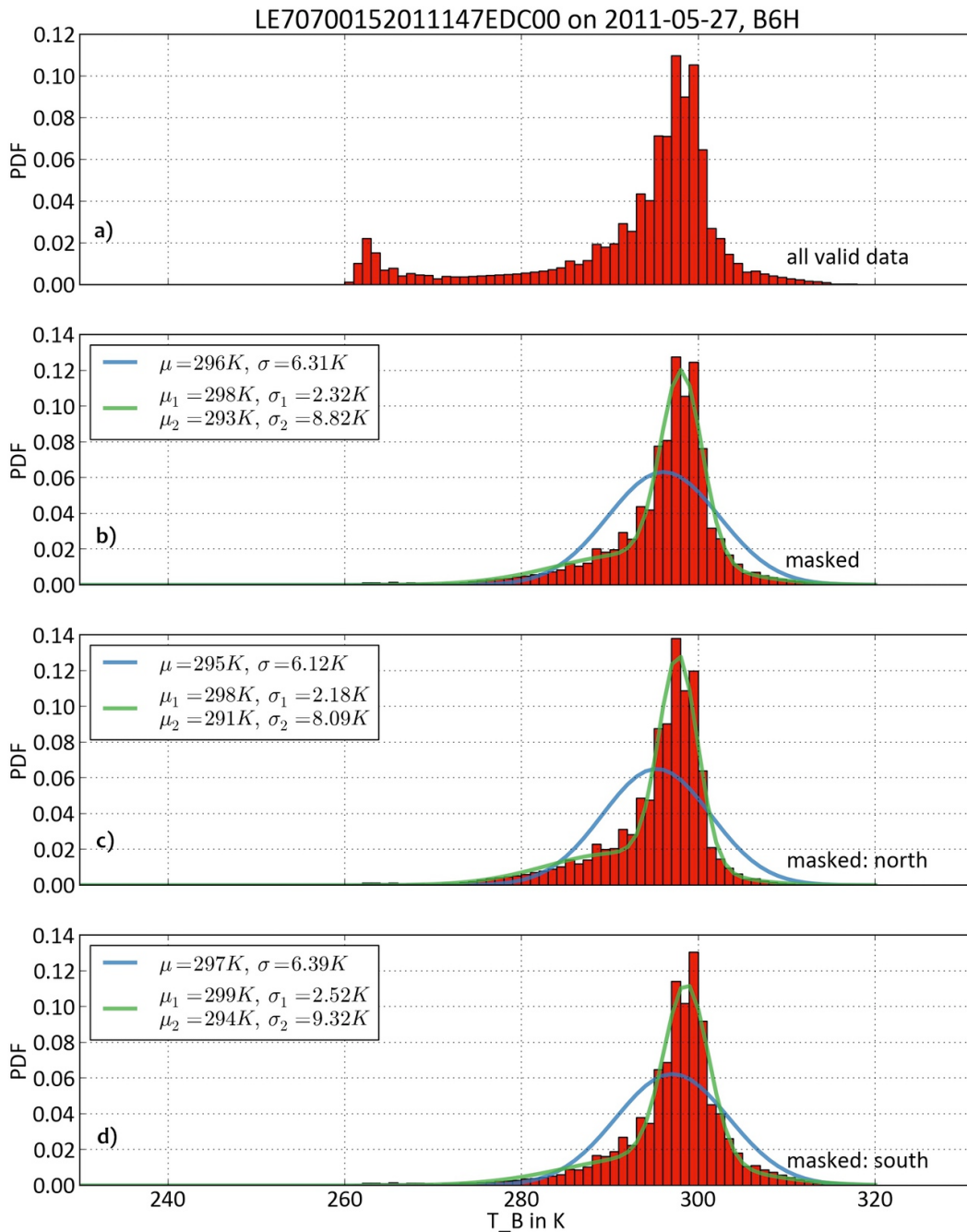


Figure A.11: Distribution of radiant temperature calculated from the thermal infrared band of the selected 2011 Landsat image for (a) the entire scene (all valid data), (b) the entire scene after complete masking, (c) only north-facing pixels of the masked scene, and (d) only south-facing pixels of the masked scene. The left tail of the (a) graph from the 'cold' clouds disappears after cloud masking (b). Compared to (c), the graph (d) is skewed to the right due to higher temperatures on the south facing slopes. A linear combination of two Gaussians curves provides a much better fit (green) than a single Gaussian curve (blue).

half of the scenes in which it was included. The distribution of anomaly occurrence indices of the image stack was then plotted over the interval between 0 and 1, and by observing the fall-off of the distribution, the threshold was set to 0.33, which implied that a pixel was counted as persistently anomalous if it appeared in more than one third of the scenes in which it was present as valid, non-masked data.

A.2.5 *Results*

Results of the histogram plot for the radiant temperatures from the entire scene (Figure A.11a) showed a clear low peak to the left due to clouds, which are typically colder than the earth surface. As expected, this peak disappeared after masking (Figure A.11 b). The distribution of radiant temperatures retrieved from north facing slopes (Figure A.11c) was skewed towards lower temperatures compared to the south facing slopes (Figure A.11d). This is a direct consequence of the higher solar insolation received by the south facing slopes in the summer season.

Result of thermal anomaly detection on a single Landsat image is shown in Figure A.12. Thermal anomalies are plotted in red and magenta, for pixels on south facing and north facing slopes, respectively. It is clear that for this particular scene the thermal anomalies occur predominantly within the perimeters of a large 2009 wildfire as well as the 2011 fire that was, at the time of image acquisition, still ongoing. Whether these anomalies are transient or persistent can only be assessed after stacking this result with information retrieved from other scenes over a period of time.

Result of persistent anomaly detection from the complete set of 40 summer-time Landsat scenes acquired between 2006 and 2013 (Table A.1) is shown in Figure A.13. The persistent anomalies are a small fraction of the total number of thermal anomalies detected while investigating all individual scenes. The 2009 wildfire area still encompasses many of the persistent anomalies, and would constitute the focal region for coal fire and forest fire hazards. In addition, fire hazard clusters are identified within commercially developed mining zones (see Figure A.13, inset images).

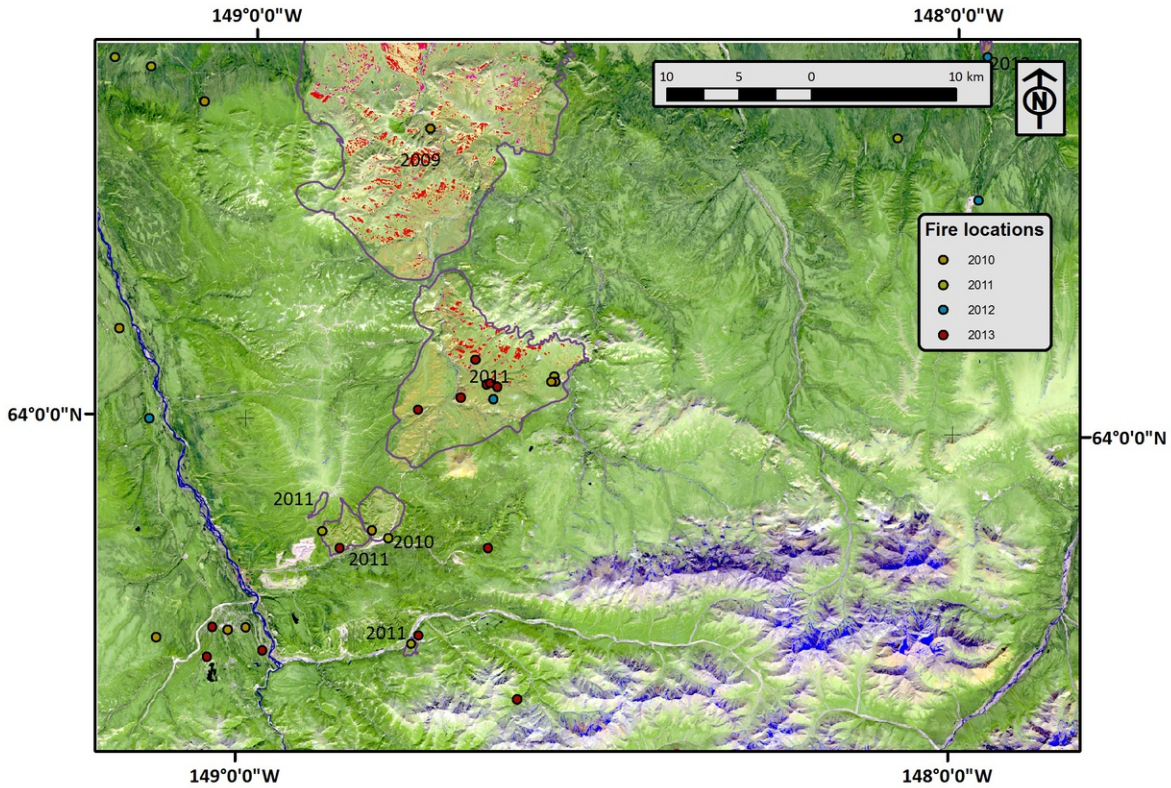


Figure A.12: Thermal anomalies retrieved from the 2011 Landsat scene are shown in red (south facing slopes) and magenta (north facing slope). Majority of the thermal anomalies are on the south facing slopes within the boundaries of the fire scars. The 2011 fire area (central part of the image) experienced multiple small localized fires in 2012 and 2013, likely due to the subsequent ignition of coal seams. The background image is a June 2013 Landsat scene.

A.2.6 Discussion

This study area includes several regions where a forest fire occurred in the recent past (see pink regions in Figure A.7, and grey outlines in Figure A.12). The Rex Creek fire occurred in 2009 and was investigated by Prakash et al. (2011) who found that persistent “hotspots” existed on the slopes of this region going as far back as 1999. They concluded that the Rex Creek fire was a boreal forest fire started from a burning coal seam. Consistent with the earlier results, the present study also shows the presence of several persistent thermal anomalies within the perimeter of the Rex Creek fire.

The persistent thermal anomalies within the perimeter of the 2011 fire scar are in close proximity to the starting points of a series of local fires that were associated with burning coal seams

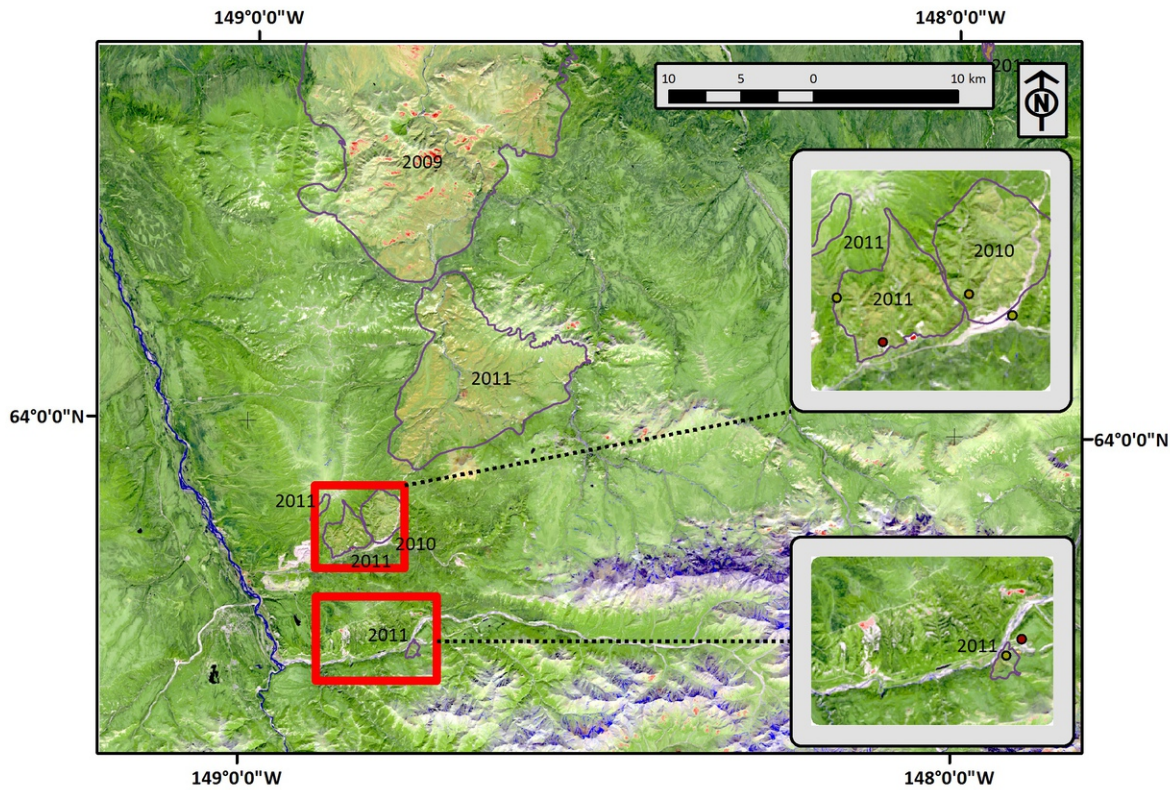


Figure A.13: Persistent thermal anomalies (red and magenta) delineated after stacking 40 processed Landsat scenes between 2006 and 2013. The insets show areas where persistent anomalies appeared in close proximity to active mines.

and appeared along the creek beds in 2012 and 2013 (Figure A.12, red and blue circles within the 2011 fire perimeter). This result highlights the need to closely monitor fire scars for multiple post-fire seasons, as these regions continue to pose a higher risk for new coal seam fires and forest fires.

Another significant finding of this study is that despite the application of a lower threshold, persistent thermal anomalies on north facing slopes are underrepresented by at least a factor of 4. Some scenes do not contain any pixels classified as anomalous on north facing slopes. This confirms the importance of differential solar heating on north and south facing slopes in high-latitudes. The south facing slopes that are directly exposed to incoming solar radiation for a longer duration warm up considerably more, raising their ambient LST and increasing the chance of spontaneous combustion of exposed coal on these slopes.

Persistent surface thermal anomalies due to the presence of underground heat sources and remnant heat from fire scars, however, show up on both north and south facing slopes, regardless of the differences in solar heating.

Of particular interest to resource development operations are hotspots in the vicinity of infrastructure and active mining zones such as those shown in the inset in Figure A.13.

The processing protocol followed in this study is largely automated and has the potential to be implemented as an operational hazard mapping system. The only manual step is the selection of a suitable threshold for the anomaly occurrence index. Should this processing protocol be applied and tested on other high-latitude regions, there would be a larger research database to rely on, that can possibly help to find a robust way to set the threshold for the anomaly occurrence index.

A.2.7 *Conclusions*

This study exemplifies that the long archive of free Landsat images offers an exceptional opportunity to map and monitor coal fire hazards in large coal bearing areas. The Landsat TIR images contain valuable information on LST that can be used to retrieve thermal anomalies. By stacking multiple datasets, the location of anomalies that persist for multiple months or years can be detected. These locations should then receive heightened attention from fire monitoring personnel.

Two main conclusions can be drawn by analyzing the thermal anomalies in conjunction with information on terrain elevation and past fire history: (i) that the south facing slopes on rugged terrain warm up considerably more than the north facing slopes, and pose a greater hazard for spontaneous combustion of exposed coal, and (ii) past burn scars show a higher presence of persistent thermal anomalies, which implies that the surface carbonaceous material here can start or re-ignite a coal fire, which in turn can trigger another cycle of forest fire. Boreal forests over the coal basins of interior Alaska are a model for such a scenario.

Data processing can be largely automated making it conceivable to design a long-term operational coal fire hazard monitoring system with only modest investments. Though such a mapping

and monitoring system would be useful in any part of the world, it is particularly important for vast, remote, infrastructure-poor regions of the world. Remote sensing based monitoring is the only practical and economical solution for such areas.

A.2.8 Acknowledgements

This work was supported in part by funding from the NASA Earth and Space Science Fellowship Grant NNX13AN90H; the University of Alaska Fairbanks (UAF) Subaward 11-07JNA from a US Department of Agriculture Grant 2010-38821-21456; and UAFs Geophysical Institute. We thank Linda Stromquist and Ed Christensen from the National Park Service for sharing their field experience and field photographs. We thank Glenn Stracher for constant encouragement and for editorial help.

A.2.9 Important Terms

Alaska	lightning strikes
anomaly occurrence index	masking
black spruce	Nenana coal basin
boreal forests	persistent anomaly detection
coal fire hazard	radiant temperatures
digital elevation model	remote sensing
forest fires	solar elevation angles
geographic information system	south facing slopes
high-latitude regions	spontaneous combustion
histogram	thermal anomalies
land cover	thermal anomaly detection
Landsat	thermal infrared (TIR)
land surface temperature (LST)	wildfires

References

- ASGDC (2014). *Alaska State Geo-Spatial Data Clearinghouse*. URL: <http://www.asgdc.state.ak.us/> (visited on 01/10/2014).
- Chander, G., B. L. Markham, and D. L. Helder (2009). Summary of current radiometric calibration coefficients for Landsat MSS, TM, ETM+, and EO-1 ALI sensors. *Remote Sensing of Environment*, vol. 113, no. 5, pp. 893–903. DOI: 10.1016/j.rse.2009.01.007.
- Chapin, F. S., M. W. Oswood, K. Van Cleve, L. A. Viereck, and D. L. Verbyla, eds. (2006). *Alaska's changing boreal forest*. Long-Term Ecological Research Network series. Oxford: Oxford University Press,
- Dissing, D. and D. L. Verbyla (2003). Spatial patterns of lightning strikes in interior Alaska and their relations to elevation and vegetation. *Canadian Journal of Forest Research*, vol. 33, no. 5, pp. 770–782. DOI: 10.1139/x02-214.
- Engle, M. A., L. F. Radke, E. L. Heffern, J. M. K. O'Keefe, C. D. Smeltzer, J. C. Hower, J. M. Hower, A. Prakash, A. Kolker, R. J. Eatwell, A. ter Schure, G. Queen, K. L. Aggen, G. B. Stracher, K. R. Henke, R. A. Olea, and Y. Román-Colón (2011). Quantifying greenhouse gas emissions from coal fires using airborne and ground-based methods. *International Journal of Coal Geology*, vol. 88, no. 2, pp. 147–151. DOI: 10.1016/j.coal.2011.09.003.
- Fauria, M. M. and E. A. Johnson (2008). Climate and wildfires in the North American boreal forest. *Philosophical Transactions of the Royal Society B: Biological Sciences*, vol. 363, no. 1501, pp. 2315–2327. DOI: 10.1098/rstb.2007.2202.
- Flores, R. M., G. D. Stricker, and S. A. Kinney (2004). *Alaska Coal Geology, Resources, and Coalbed Methane Potential*. Tech. rep. DDS-77. United States Geological Survey.
- GDAL Development Team (2011). *GDAL - Geospatial Data Abstraction Library, Version 1.8.1*. Open Source Geospatial Foundation. URL: <http://www.gdal.org> (visited on 12/05/2013).
- GINA (2014). *Geographic Information Network of Alaska*. University of Alaska Fairbanks. URL: <http://gina.alaska.edu>.
- Global Administrative Areas (2014). *Database of Global Administrative Areas, Version 2.0*. URL: <http://www.gadm.org> (visited on 07/10/2013).

GNIS (2013). *US Board on Geographic Names - USGS Geographic Names Information*. URL: <https://geonames.usgs.gov/> (visited on 07/10/2013).

Gupta, R. P. and A. Prakash (1998). Cover: Reflectance aureoles associated with thermal anomalies due to subsurface mine fires in the Jharia coalfield, India. *International Journal of Remote Sensing*, vol. 19, no. 14, pp. 2619–2622. DOI: 10.1080/014311698214415.

Hudspith, V., A. C. Scott, M. E. Collinson, N. Pronina, and T. Beeley (2012). Evaluating the extent to which wildfire history can be interpreted from inertinite distribution in coal pillars: An example from the Late Permian, Kuznetsk Basin, Russia. *International Journal of Coal Geology*. European Coal Conference 2010, vol. 89, no. Supplement C, pp. 13–25. DOI: 10.1016/j.coal.2011.07.009.

Kasischke, E. S., D. Williams, and D. Barry (2002). Analysis of the patterns of large fires in the boreal forest region of Alaska. *Int. J. Wildland Fire*, vol. 11, no. 2, pp. 131–144. DOI: 10.1071/WF02023.

Key, C. and N. Benson (2006). *Landscape Assessment: Ground measure of severity, the Composite Burn Index; and Remote sensing of severity, the Normalized Burn Ratio*. Other Government Series RMRS-GTR-164-CD: LA 1-51. Ogden, UT: USDA Forest Service, Rocky Mountain Research Station.

Kim, A. G. (2007). Greenhouse gases generated in underground coal-mine fires. In: *Geology of Coal Fires Case Studies from Around the World*. Ed. by G. B. Stracher. Geological Society of America.

Kuenzer, C., J. Zhang, J. Li, S. Voigt, H. Mehl, and W. Wagner (2007). Detecting unknown coal fires: synergy of automated coal fire risk area delineation and improved thermal anomaly extraction. *International Journal of Remote Sensing*, vol. 28, no. 20, pp. 4561–4585. DOI: 10.1080/01431160701250432.

Kuenzer, C., J. Zhang, Y. Sun, Y. Jia, and S. Dech (2012). Coal fires revisited: The Wuda coal field in the aftermath of extensive coal fire research and accelerating extinguishing activities. *International Journal of Coal Geology*, vol. 102, no. Supplement C, pp. 75–86. DOI: 10.1016/j.coal.2012.07.006.

Merritt, R. D. and C. C. Hawley (1986). *Map of Alaska's Coal Resources*.

Newberry, R. (2013). *What percent of Alaska is mapped and at what scale?* personal communication.

NPS (2012). *National Park Service Photo Gallery: Tatonduk River Windfall Mountain Fire*. URL: <http://www.nps.gov/media/photo/gallery.htm?id=33B24601-1DD8-B71C-07660A0CDCC89DDD> (visited on 12/10/2013).

Oliphant, T. E. (2007). Python for Scientific Computing. *Computing in Science Engineering*, vol. 9, no. 3, pp. 10–20. DOI: 10.1109/MCSE.2007.58.

Oreopoulos, L., M. J. Wilson, and T. Várnai (2011). Implementation on Landsat Data of a Simple Cloud-Mask Algorithm Developed for MODIS Land Bands. *IEEE Geoscience and Remote Sensing Letters*, vol. 8, no. 4, pp. 597–601. DOI: 10.1109/LGRS.2010.2095409.

Pedregosa, F., G. Varoquaux, A. Gramfort, V. Michel, B. Thirion, O. Grisel, M. Blondel, P. Prettenhofer, R. Weiss, V. Dubourg, J. Vanderplas, A. Passos, D. Cournapeau, M. Brucher, M. Perrot, and É. Duchesnay (2011). Scikit-learn: Machine Learning in Python. *Journal of Machine Learning Research*, vol. 12, 2825–2830.

Prakash, A., R. Gens, and Z. Vekerdy (1999). Monitoring coal fires using multi-temporal night-time thermal images in a coalfield in north-west China. *International Journal of Remote Sensing*, vol. 20, no. 14, pp. 2883–2888. DOI: 10.1080/014311699211868.

Prakash, A. and R. P. Gupta (1999). Surface fires in Jharia coalfield, India-their distribution and estimation of area and temperature from TM data. *International Journal of Remote Sensing*, vol. 20, no. 10, pp. 1935–1946. DOI: 10.1080/014311699212281.

Prakash, A., R. P. Gupta, and A. K. Saraf (1997). A Landsat TM based comparative study of surface and subsurface fires in the Jharia coalfield, India. *International Journal of Remote Sensing*, vol. 18, no. 11, pp. 2463–2469. DOI: 10.1080/014311697217738.

Prakash, A. (2014). *Coal fires - A Natural or Man Made Hazard*. URL: <http://www.gi.alaska.edu/~prakash/coalfires> (visited on 01/05/2014).

Prakash, A. and R. Gens (2011). Chapter 14 - Remote Sensing of Coal Fires. In: *Coal and Peat Fires: A Global Perspective*. Ed. by G. B. Stracher, A. Prakash, and E. V. Sokol. Vol. 1. Amsterdam: Elsevier, pp. 231–253.

Prakash, A., R. Gens, S. Prasad, A. Raju, and R. P. Gupta (2013). Chapter 10 - Coal Fires in the Jharia Coalfield, India. In: *Coal and Peat Fires: A Global Perspective*. Ed. by G. B. Stracher, A. Prakash, and E. V. Sokol. Vol. 2. Boston: Elsevier, pp. 153–177.

Prakash, A., K. Schaefer, W. K. Witte, K. Collins, R. Gens, and M. P. Goyette (2011). A Remote Sensing and GIS Based Investigation of a Boreal Forest Coal Fire. *International Journal of Coal Geology*, vol. 86, no. 1, pp. 79–86. DOI: 10.1016/j.coal.2010.12.001.

Prakash, A. and Z. Vekerdy (2004). Design and implementation of a dedicated prototype GIS for coal fire investigations in North China. *International Journal of Coal Geology*. Coal Fires Burning around the World: a Global Catastrophe, vol. 59, no. 1, pp. 107–119. DOI: 10.1016/j.coal.2003.12.009.

Raju, A., R. P. Gupta, and A. Prakash (2013). Delineation of coalfield surface fires by thresholding Landsat TM-7 day-time image data. *Geocarto International*, vol. 28, no. 4, pp. 343–363. DOI: 10.1080/10106049.2012.710651.

Stracher, G. B., R. B. Finkelman, J. C. Hower, D. N. Pone, A. Prakash, D. R. Blake, P. A. Schroeder, S. D. Emsbo-Mattingly, and J. M. K. O'Keefe (2009). Natural and anthropogenic coal fires. In: *Encyclopedia of Earth*. Ed. by A. U. Dogan and C. J. Cleveland. National Council for Science and the Environment.

Stracher, G. B., A. Prakash, and E. V. Sokol (2010). *Coal and Peat Fires: A Global Perspective: Volume 1: Coal - Geology and Combustion*. Vol. 1. Elsevier.

Stracher, G. B., A. Prakash, and E. V. Sokol (2012). *Coal and Peat Fires: A Global Perspective: Volume 2: Photographs and Multimedia Tours*. Vol. 2. Elsevier.

Stracher, G. B., E. V. Sokol, and A. Prakash (2015). *Coal and peat fires: A Global Perspective. Volume 3: Case Studies - Coal Fires*. Vol. 3. OCLC: 909314538. Amsterdam: Elsevier.

USGS (2012). *Landsat - a global land-imaging mission*. Fact sheet 2012-3072. US Geological Survey, p. 4.

Wendler, G., J. Conner, B. Moore, M. Shulski, and M. Stuefer (2010). Climatology of Alaskan wild-fires with special emphasis on the extreme year of 2004. *Theoretical and Applied Climatology*, vol. 104, no. 3, pp. 459–472. DOI: 10.1007/s00704-010-0357-9.

Whitehouse, A. E. and A. A. S. Mulyana (2004). Coal fires in Indonesia. *International Journal of Coal Geology*. Coal Fires Burning around the World: a Global Catastrophe, vol. 59, no. 1, pp. 91–97. DOI: 10.1016/j.coal.2003.08.010.

Zhang, J., W. Wagner, A. Prakash, H. Mehl, and S. Voigt (2004). Detecting coal fires using remote sensing techniques. *International Journal of Remote Sensing*, vol. 25, no. 16, pp. 3193–3220. DOI: 10.1080/01431160310001620812.

WWW Addresses: Additional

(1) Alaska Fire Science Consortium <http://www.frames.gov/partner-sites/afsc/home/> (accessed January 2014)

(2) Alaska Science Center: Post-Fire Succession Pattern <http://alaska.usgs.gov/science/geography/post-fire.html> (accessed January 2014)

(3) Usibelli Coal Mine, Inc. <http://www.usibelli.com> (accessed January 2014)

(4) Alaska Interagency Coordination Center <https://fire.ak.blm.gov/> (accessed January 2014)